Argonne
NATIONAL LABORATORY

ANL-GenIV-070

# Generation IV Nuclear Energy System Initiative Pin Core Subassembly Design for the Gas-Cooled Fast Reactor

Nuclear Engineering Division

**About Argonne National Laboratory**

Argonne is a U.S. Department of Energy laboratory managed by The University of Chicago under contract W-31-109-Eng-38. The Laboratory's main facility is outside Chicago, at 9700 South Cass Avenue, Argonne, Illinois 60439. For information about Argonne, see www.anl.gov.

**Availability of This Report**

This report is available, at no cost, at http://www.osti.gov/bridge. It is also available on paper to the U.S. Department of Energy and its contractors, for a processing fee, from:

U.S. Department of Energy
Office of Scientific and Technical Information
P.O. Box 62
Oak Ridge, TN 37831-0062
phone (865) 576-8401
fax (865) 576-5728
reports@adonis.osti.gov

ANL-GenIV-070

# Generation IV Nuclear Energy System Initiative

# Pin Core Subassembly Design for the Gas-Cooled Fast Reactor

---

by
M. T. Farmer
E. A. Hoffman
P. F. Pfeiffer
I. U. Therios
T. Y. C. Wei
Nuclear Engineering Division, Argonne National Laboratory

April 2006

## Table of Contents

## List of Figures

## List of Tables

# 1. Introduction and Conclusions

## 1.1 Background

The Gas-Cooled Fast Reactor (GFR) is one of six systems selected for viability assessment in the Generation IV program. It features a closed nuclear fuel cycle, consisting of a high-temperature helium-cooled fast spectrum reactor, coupled to a direct-cycle helium turbine for electricity production. The GFR combines the advantages of fast spectrum systems with those of high-temperature systems. It was clear from the very beginning that the GFR design should be driven by the objective to offer a complementary approach to liquid metal cooling. On this basis, CEA and the US DOE decided to collaborate on the pre-conceptual design of a GFR. This reactor design will provide a high level of safety and full recycling of the actinides, and will also be highly proliferation resistant and economically attractive.

The status of this collaborative project is that two unit sizes, 600 MWt and 2400 MWt were selected as the focus of the design and safety studies. Researchers studied fuel forms, fuel assembly/element designs, core configurations, primary and balance-of-plant layouts, and safety approaches for both of these unit sizes. Results regarding the feasibility of this GFR design are encouraging. For example, sustainability and non-proliferation goals can be met and the proposed concept has attractive safety features. These features take advantage of the helium in terms of its neutronic quasi-transparency as well as the enhanced Doppler effect in connection with candidate fuel and structural materials. The current design trend is to consider high unit power for the GFR (2400 MWt), an attractive level for the power density (100 $MW/m^3$), and the implementation of an innovative plate type fuel or pin type sub-assembly with carbide-based actinide compounds and SiC-based structural materials. Work is still needed to refine the safety approach, to select the main system options, and to more definitively establish economic parameters.

To summarize, the research team assembled point designs from different options and combinations, as described below [1]:

- Fuel choice: Dispersed fuel in plate sub-assemblies as the reference, SiC-cladded pellets in pin sub-assemblies as a back-up. The selected actinide compound was carbide in the design studies, but nitride remains a possible candidate.
- Unit size: 2400 MWt
- Power density: 100$MW/m^3$
- Decay heat removal: Natural convection passive approach, which should be combined with active means (low power circulators) in a well balanced mix to be refined. This does not exclude alternative options (search for conduction paths, heavy gas injection, etc.) on which some future effort should still be devoted.
- Balance-of-plant: Direct Brayton cycle balance-of-plant option remains the reference, but consideration of the indirect super-critical $CO_2$ cycle with an equivalent cycle efficiency has also been included.

The development of fuels is the key challenge remaining for future research.

More effort has therefore been concentrated on details of the core design tying together core neutronics, assembly thermal-hydraulics and fuel element structural design, and fuel performance. In agreement with CEA, CEA will perform the design work on the reference plate fuel core design while the US side is to perform the design work on the back-up pin core design. This report documents the current status of the US effort on pin element, bundle and core design for the back-up option.

## 1.2 Pin Fuel Design Issues

Fast reactor cores composed of fuel pins in subassembly bundles have been designed over a considerable period of time. And in the case of sodium coolant, there has been significant operational experiences in the performance of these designs and important feedback for the key design issues. In the case of gas coolant, in particular helium, while there has been no operational experience, major expertise has been brought to bear in the past on the design of pins, bundles, and cores for various versions of the gas cooled fast reactor by design teams. These different perspectives can be regarded to have been incorporated into the pin core design of the General Atomics (GA) 300 MWe demonstration GCFR plant of thirty years ago [2]. This pin core design served as the starting point for the GENIV GFR 2400 MWt design documented in this report.

The GA GCFR demonstration plant utilized the fuel pin technology of the LMFBR/LMFR. This LMFBR fuel pin design encapsulated MOX fuel pellets in 316 SS tube cladding. The GA approach was that no new fuel pin technology development was required for the GCFR since it could utilize the LMFR fuel pin technology. However there were differences in that part of the GCFR fuel pin was roughened to enhance the heat transfer characteristics of helium gas coolant, and the fuel pin was vented to account for the higher background primary helium coolant pressure. Experiments were specifically performed to address these two different design features. While these modifications were significant, the much larger design feature modifications of the GENIV GFR is in the choice of cladding material. Due to the much higher coolant outlet temperature (850°C) of the direct cycle GENIV GFR compared to the coolant outlet temperature (~510°C) of the GA GCFR, the GCFR metallic cladding (316 SS) will have to be replaced by a high temperature, high fast neutron flux tolerant ceramic (SiC). Refractory metals for this particular application have been assessed and discarded. The choice of a ceramic material for cladding brings with it a number of issues chief of which are fabrication questions and resultant implications for the design of the pin, the subassembly bundle and the core. In addition, ceramics will have to be selected not only for the pin but for the upper part of the bundle, in this upflow design, where load bearing structures have to be located in the high temperature (850°C) gas flow.

For the ceramic pin cladding the main fabrication questions are:

1. The maximum length of the claddings tubes – implications are multiple segment pin designs and
2. The minimum thickness of the tubes – implications are thick cladding and reduced heat transfer

3. The maximum strength of the tubes – implications are that fission gas venting may be needed

Translated into design issues, the following key parameters/phenomena need to be addressed.

A. Pin Design

(i) Thermal Bowing

Cold to hot operations leading to differential axial expansion and non-uniform radial distributions of temperature caused by power and flow distributions will lead to bowing of the fuel pin. This thermal induced bowing of the pin is a well known phenomena in reactor subassembly bundle mechanical design and is accommodated by the use of strategically located pin bundle spacers. The implications of the selection of a ceramic cladding replacing metal cladding for the thermal bowing needs to be examined. Significant bowing could not only lead to local flow blockages and uncoolable geometry but also tensile stresses, cycling and ultimately pin failure.

(ii) Flow-Induced Vibration

Flow induced vibration has both a parallel flow and a cross flow component to it since the flow in ducted the bundle is three dimensional even though the predominant direction is upward in the axial direction. This is true under even natural convection condition though the speed of the flow is substantially reduced in this mode. In the normal operation mode, it is well known that very high gas flow velocities (10s of m/s) occur in the bundles and conceptually could subject individual pins in local regions to high momentum fluxes. The resultant vibration, while potentially detrimental in terms of wear, fatigue, and cycling, is design dependent. The location of spacers can change both the frequency and amplify the vibrations. Extensive work in this area has been performed for LMFR pin bundles and the implications of the phenomena for a "brittle" ceramic clad GFR pin needs to be evaluated for the possibilities of early pin failure.

(iii) Fission-gas Pressure

In contrast to the dispersed fuel plate reference option where containment of the fission gas generated is carried out the at the local level, similar to the HTR coated particle fuel, confinement of the fission gases is carried out at a global level in a common fission gas plenum. This fission gas volume is provided at either the top or bottom of the fuel pin but the resultant gas pressure produces principally a hoop stress in the pin cladding. The mechanical strength of the clad material has to be high enough to accommodate this stress over the cycle life under high temperature and high fast fluence irradiation conditions. Thermal cycling also needs to be factored in. Possible failure of pin integrity with relatively weak ceramic clad under this fission gas pressure might require the use of fuel pin venting to balance the primary coolant pressure across the cladding thickness.

B. Subassembly Bundle Design

(i) Selection of Materials

As in the case of the individual pins, materials will have to be selected for the bundle structure which locates the pins, the plates which support the weight of the fuel and the

lower end piece and nozzle which transmit that weight to the core grid plate. In addition there are spacers for the bowing and vibration mitigation, tie rods, upper end piece for fuel handling and the subassembly wrapper for the ducted flow. Axial shielding material also has to be provided to protect the upper internals and the grid plate from the fast fluence during the cycle lifetime. Aside from the fast fluence environment, the major environmental factor is the high temperature. This is very much of a materials R&D challenge for future materials development. A combination of metals at the low temperature inlet end and ceramics at the high temperature outlet-end may be possible but the differences in thermal expansion coefficients would lead to difficulties with thermal stress. In addition there would be fabrication issues.

(ii) Selection of Spacers

Spacers, classically, are required in pin bundle designs to mitigate bowing and vibration phenomena. However, these serve as a source of pressure losses in the gas flow field. This is detrimental not only under the normal forced flow operating condition but especially so under low-pressure low-flow natural convection conditions. At low Reynolds numbers the Reynold's number dependence of the form loss component of the spacer induced pressure losses could be dominant. The safety approach selected of the GFR depressurized decay heat removal events is natural circulation heat removal of the core at ~7-8 bar. A significant number of spacers would be very detrimental to the natural circulation mass flow rate and this safety approach.

C. Core Design

(i) Thick Clad

The need for substantial thickness of the cladding due to the fabrication process for ceramic tubing would be disadvantageous to fuel loading. Significant structural volume requirements in the core would lead to less fuel reactivity potential and possibly softer spectrums. In addition, thick clad would reduce the area available for gas flow. This would be a disadvantage for natural convection potential.

(ii) Power Peaking Factors

Natural convection flow stability at low pressure conditions for gases is an issue which needs to be addressed. Non-uniform temperature peaking across the core coupled with the temperature dependence of the viscosity behavior of gases are conducive to the onset of flow and temperature instability. Orificing of the subassembly flow is not a particularly attractive design option for more uniform gas flow temperature distributions as an increase in total core pressure drop would also result. This is not desirable for natural convection flow and orifices would also have the form loss Reynolds number dependence similar to spacers. Fission power, and therefore decay power, flattening would be the design solution of choice. This should be a design target incorporated into the process.

## 1.3 Fuel Pin Concepts

These fuel pin design issues have been iterated on through a number of fuel pin design concepts as the GENIV project has proceeded, in particular through the I-NERI collaboration on GFR development with CEA. Table 1.1 shows the concepts in

chronological order from (1) to (4). Design concept (1) started from the GA GCFR pin design for the 300 MWe demonstration plant [2].

**Table 1.1. GFR Fuel Pin Concepts**

| | |
|---|---|
| (1) | Tall Vertical Single-Segment Pin |
| (2) | Vertical Split-Segment Pin |
| (3) | Short Horizontal Single-Segment Pin |
| (4) | Tall vertical Single-Segment Vented Pin |

A summary is given here in chronological order of each design concept, the issues it addressed and the issues which lead to modification. The current reference design is concept (4) and the most recent work and future work is focused on this vertical single-segment vented pin concept. Chapters 2-4 provide details on some of the current issues and design solutions. Reference [1] provide details of the previous work and rationale. The fuel actinide compound for all these concepts, in agreement with CEA, is UC prepared in the form of solid solution pellets.

### 1.3.1 Tall-Vertical Single Segment Pin

This pin design concept is patterned after the GA GCFR design of 30 years ago for the GA 300 MWe GCFR demonstration plant. A major difference is that given the design criteria of the GENIV program non-proliferation goals, the axial blanket pellets utilized in the pin design of 30 years ago have been removed. In addition, to minimize the fabrication demands on the SiC tubing length, the in-pin axial shielding pellets have been removed. The axial shielding will now be entirely external to the pin [3] similar to what was done for the EBR II Mark V subassembly design. Other differences are that;

(i) This is not a vented fuel pin design. A fission gas plenum patterned after the LMFR fission gas plenum is provided. The engineering judgment was made that where possible a vented fission gas system was to be avoided because of its complexity and potential safety implications.

(ii) Since the core power density has been derated to 100 w/cm$^3$ from the 250 w/cm$^3$ of the GCFR, clad roughening was found not to be required and is therefore not utilized to enhance the gas coolant heat transfer. This is a significant design modification since artificial roughening of the surface of the ceramic clad may not only be difficult but detrimental to its integrity. The selection of the derating of the power density is further discussed in [4] which provides the details on the safety approach for depressurized decay heat removal. Natural convection has been selected for this function.

Figure 1.1 shows the geometry of this concept. Notable features are an upper axial plenum length of 1.0 m; an upper axial reflector length of 0.5 m; an active core length of 1.34 m; a lower axial reflector axial length of 0.5 m; .0845 cm fuel pin outside diameter and 0.04cm SiC clad thickness. Additional design parameters are given in Table 1.2. A tall cladding tube (3.34 m) with "thin" walls (same as metal clad) is required. Clad thermal margins are acceptable [5] Figure 1.2 [5] shows the cladding hoop stress as fission gas is generated with burnup over the lifetime. With the primary helium coolant operating pressure of 70 MPa, the cladding is continually under compression. For monolithic SiC, the strength may be at the limit at BOL but the margins improve toward

EOL. However, when the reactor is depressurized to refueling conditions (1 bar), the spike in clad hoop stress (Figure 1.2), indicates that the pin may rupture in tension. It should be noted that Figure 1.3 does not include the hot-to-cold shutdown which could reduce the fission gas pressure as the fission gas plenum is cooled down to ~150°C before refueling begins. Still, the results are clearly indicative of the need to consider refueling and pressure variations during depressurization accidents in the pin design. The core average fuel thermal margins have been shown to be not adequate for this concept [6]. This is due to the use of a solid fuel pellet with a large clad-to-pellet gap. It was thought necessary to prevent pellet-clad-interaction induced by gap-closure with fuel swelling, by the use of a large gap. However this led to unacceptable pin temperature drops. The GA GCFR pin utilized annular pellets in a metallic clad. The judgment was made to allow for extra margin to PCI since the GFR clad is ceramic which is known to be brittle.

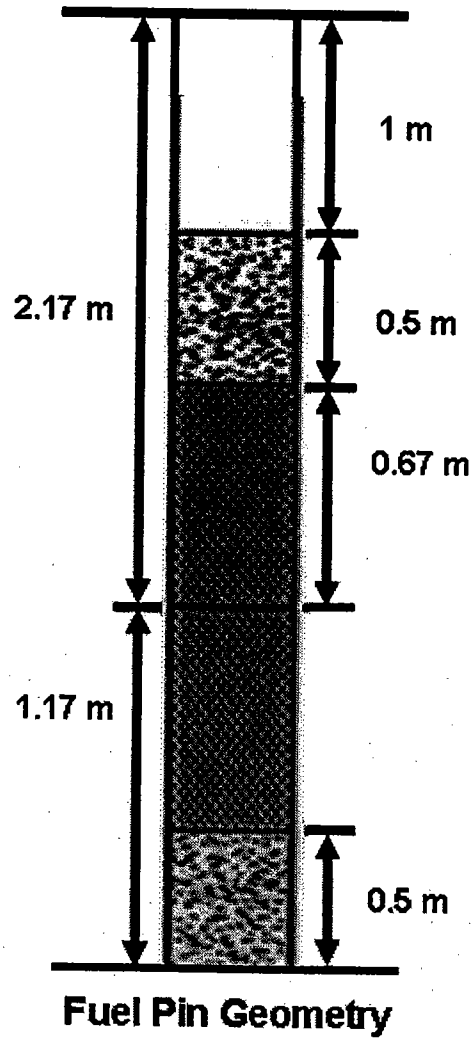


**Figure 1.1. Tall Vertical Single-Segment Pin**

**Table 1.2. Tall Vertical Single Segment Pin Design Parameters**

| Parameter | Value |
|---|---|
| Fuel | (U-15Pu)C |
| Cladding OD | 8.45 mm |
| Cladding wall thickness[1] | 0.4 mm |
| Pellet diameter | 6.73 mm |
| Pellet density | 97% |
| Active core height | 1.34 m |
| Plenum height | 1.0 m |
| Core inlet/outlet temperature | 480/850°C |
| Plenum temperature used for calculation | 665°C |
| Average burnup | 10 at.% |
| Pin fill gas pressure | 5 atm |
| Core pressure | 7 MPa |
| Fuel centerline temperature | 1275°C |
| Fractional fission gas release at EOL | 37% |

Notes:

- A more realistic value for SiC/SiCf would be 1-1.2 mm, due to manufacturing constraints.
- Pellet density of 97% may not be realistic due to manufacturing and fuel performance issues.
- Hypothesized primary system depressurization happens at EOL

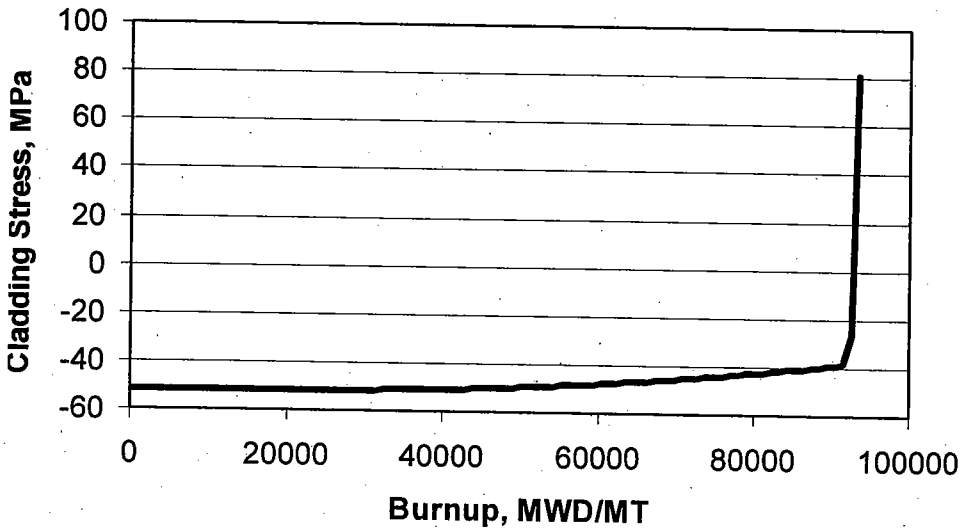


**Figure 1.2. Fuel Pin Clad Hoop Stress with Burnup (includes primary system depressurization at 90,000 MWD/MT)**

### 1.3.2 Vertical Split-Segment Pin

After the thermal margins assessment for the concept of an average core pin was completed, it was learned that the latest SiC composite tubing fabrication experiments in Japan at Kyoto University [7] were showing trends for thicker tubing and shorter fabrication lengths. Difficulties had been encountered in trying to fabricate long thin tubing with the SiC composites produced by the NITE process. The judgment to date has been that monolithic SiC tubes ($\alpha$ or $\beta$ phase) would not have the required strength both for fission gas retention or fuel handling needs. The conclusion being that higher strength SiC/SiC composites should be the pathway forward. Factoring in these results from Kyoto University it was decided to increase the pin design cladding thickness by a factor of 2 and to decrease the tubing length by a 1/2. This lead to pin concept (2) shown in Figure 1.3. This is a split segment pin (two segments) with thick clad. As with pin concept (1), concept (2) has a 0.5 m upper axial reflector length but the fission gas plenum has been split in two. There is a top 0.5 m upper axial plenum length, and a bottom 0.5 m lower axial plenum length. The 1.34 m active core length remains the same but is symmetrically split between the two segments. The 0.5 m lower axial reflector length in the bottom segment is a duplicate of the top segment geometry. An increase to 0.1 cm fuel clad thickness leads to a 0.957 cm fuel pin outside diameter. The pellet design is now an annular one and the clad-pellet gap has been significantly decreased. Details are available in Table 1.3. As with pin concept (1), the cladding is SiC, there are no external blankets and there is above and below core shielding. In addition to thermal margin design calculations, evaluations were also made of thermal bowing and axial flow-induced vibration. Even with ceramic cladding, due to the large temperature differences and levels, thermal bowing is still an issue. The solution requires the use of a number of spacers to reduce the bowing amplitude. However the use of spacers increases the bundle pressure drop and reduces the natural convection core cooling flow particularly during depressurization events. The design solution would not be consistent with the current safety approach to decay heat removal. Design solutions have been proposed in [8] to allow axial free expansion of the pin at the lower fuel support plate as well as simultaneously providing lateral restraint against vibration. Figure 1.4 shows a proposed solution. The evaluation also shows the axial-flow induced vibration is minor. Cross flow induced vibration is discussed in Section 4.3. Three "spacer" plates are therefore proposed. The lower and upper fuel support plates and a core midplane plate shown in Figure 1.5 attach the two segments together.

In summary the split pin status started with the single pin design increased clad thickness to 1 mm, and went to a two segment design. The fuel pin design conclusions are:

- Need to accommodate the axial clad expansion.
  a. Likely to fail in a tensile mode of failure with unconstrained thermal bowing
  b. Thermal bowing would require a large number of spacers
- A two pin design with an end support guide and a bonded head connector is proposed.
- Axial flow induced vibration should not be an issue.

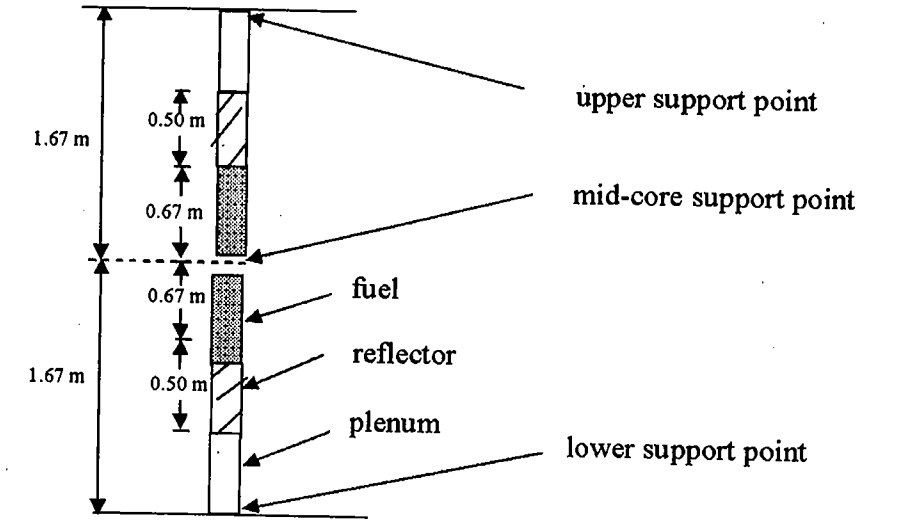


**Figure 1.3. Vertical Split Segment Pin (2) Geometry**

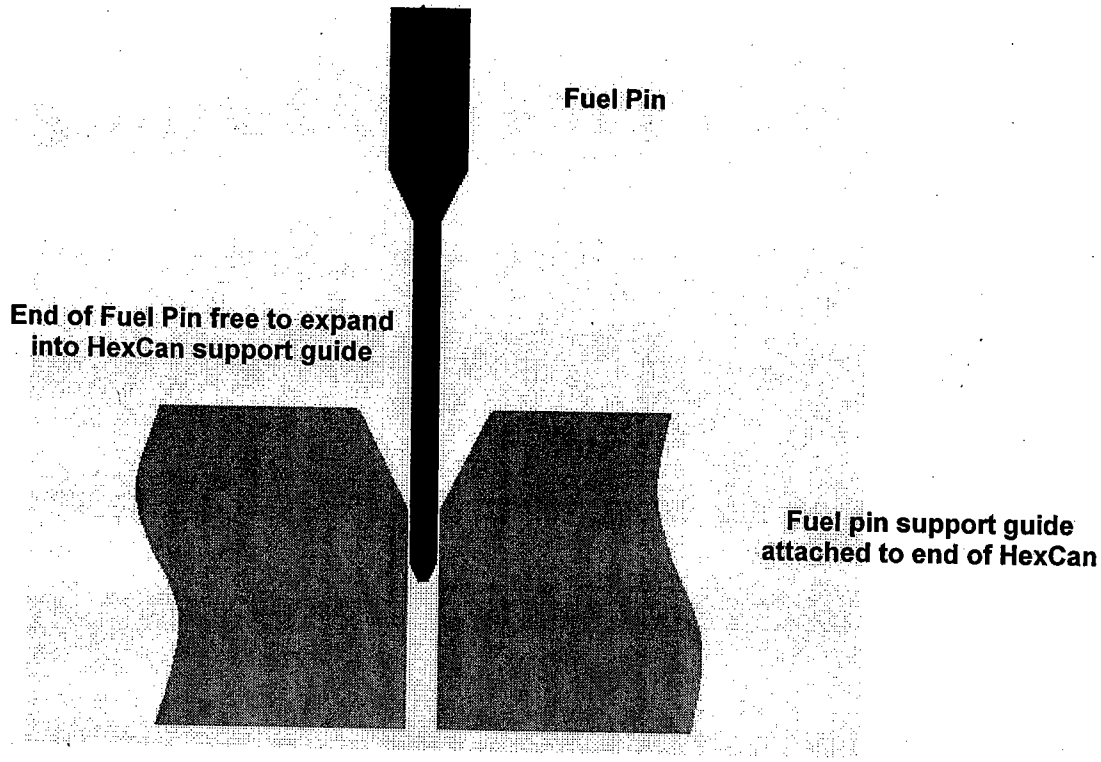


**Figure 1.4. Conceptual Design for Fuel Pin End Support**

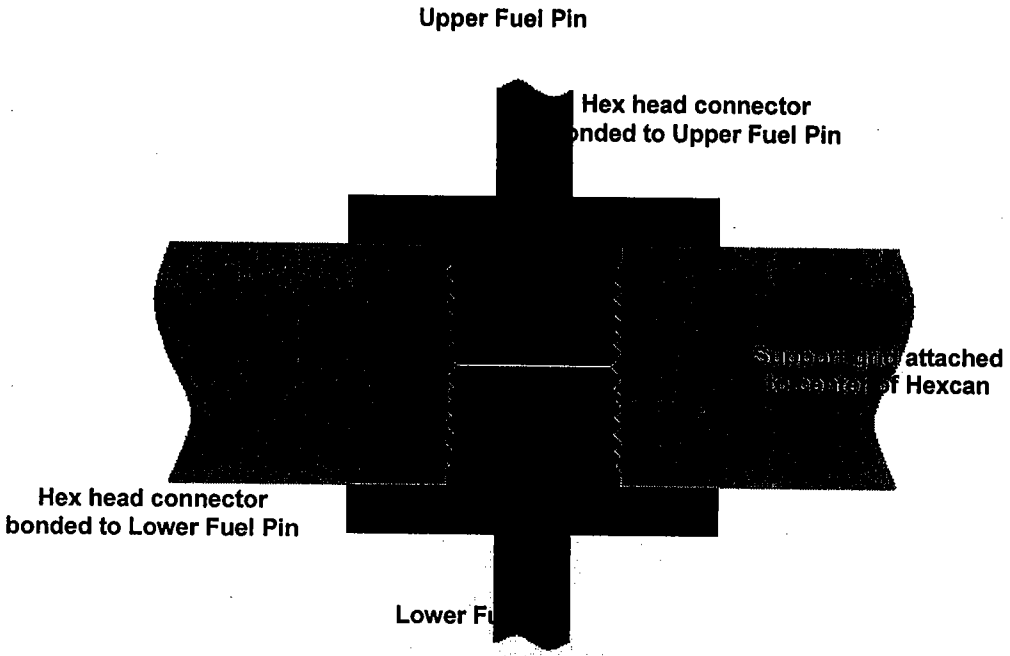


**Figure 1.5. Conceptual Design for Fuel Pin Attachment to Center Support Grid**

This pin concept satisfies the average thermal margins and the bowing constraints. It holds promise also for adequate vibration performance. However refueling still needs to be considered as well as other depressurization events.

### 1.3.3 Short Horizontal Single Segment Pin

After pin concept (2) was designed, further updates on the SiC/SiC components fabrication experiments were received [9]. The data trend pointed in the direction of even shorter pins ~0.25m. The minimum tube thickness selection showed promise but "long" tubes for "long" pins may be difficult to fabricate. Short pins of 0.25m length could not be possibly utilized in a vertical pin bundle without a significant number of segments. As Figure 1.6 shows then this would require multiple fission gas plena in a single pin. This would lead to considerable neutron streaming with this fast reactor spectrum. Staggering of pellets in neighboring pins might be considered but this would lead to administrative/QA problems for a core with upward of $10^5$ pins. To avoid a multi-segmented pin with multiple fission gas plena, a horizontal pin configuration in the bundle should be considered. This is shown in Figure 1.7. Unlike the CANDU design, the horizontal pins are still stacked in a vertical bundle. The bundle/subassembly is still inserted into and removed from the core in the vertical direction but the pins are stacked horizontally with vertical upflow which flows cross-wise across the pin. Even in this configuration, the issue of enhanced neutron streaming leakage pathways can be foreseen, as illustrated in Figure 1.8. In addition the length of the horizontal fission gas plena when accumulated across the many rows of subassemblies results in an increased vessel diameter. This violates the GT-MHR criteria set for the vessel diameter design

goal. The proposed design solution is an external plena attached to the subassembly walls shown in Figure 1.9. This however is inconsistent with the original premise that it is difficult to fabricate long lengths of strong SiC/SiC composite tubing. Figure 1.10 shows long length of "tubing" required for the external plena. Long lengths of monolithic SiC tubing [10] have been manufactured for industrial purposes over several decades. This can be utilized for the external plena but this would require lower fission gas plena pressure due to the relatively low strength of the monolithic SiC. In effect, a vented pin solution is call for. If this is the case then this approach opens up the possibility of a vertical vented pin design. The only reason at this stage to retain the short horizontal pin design is if there are larger thermal fluid margins with this option. Chapter 4 presents results from an extensive set of parametrics on the horizontal pin bundle configuration. These show that in spite of the improved Nusselt number and enhanced heat transfer in the cross flow configuration, the increased friction factor of the cross flow configuration over the parallel flow configuration cannot be compensated for by increases in pin diameter. The results show that for the target power density and vessel size, the bundle pressure drops are too high. This short horizontal single segment pin concept is dropped from further consideration. The project focus should be on a tall vertical pin/bundle design.

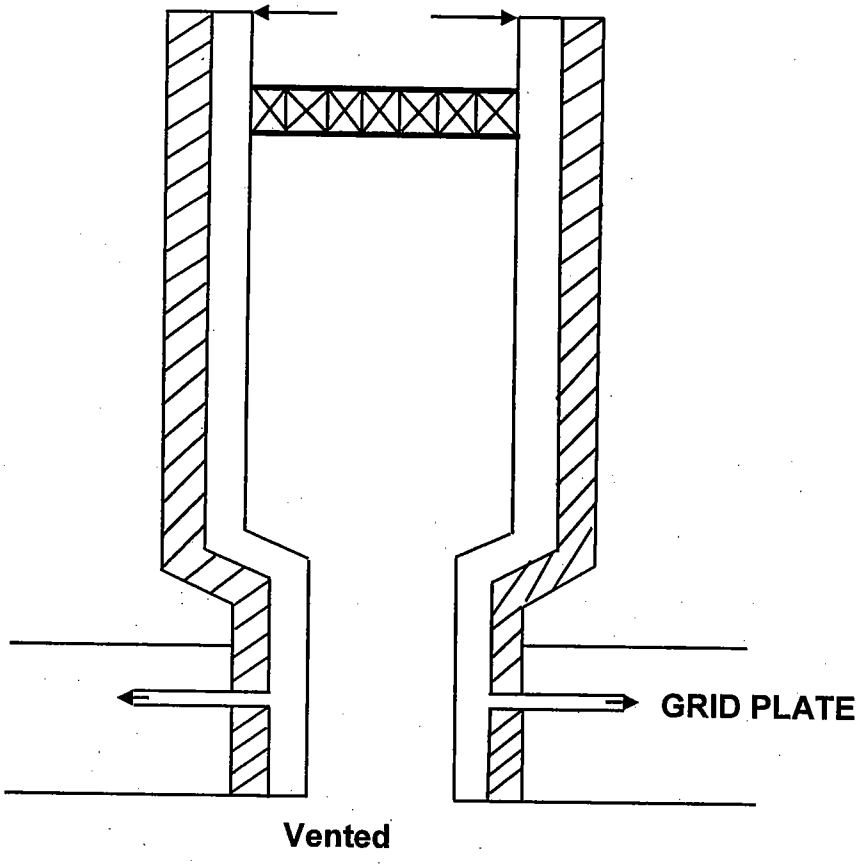


**Figure 1.6. Short Horizontal Single Segment Pin**

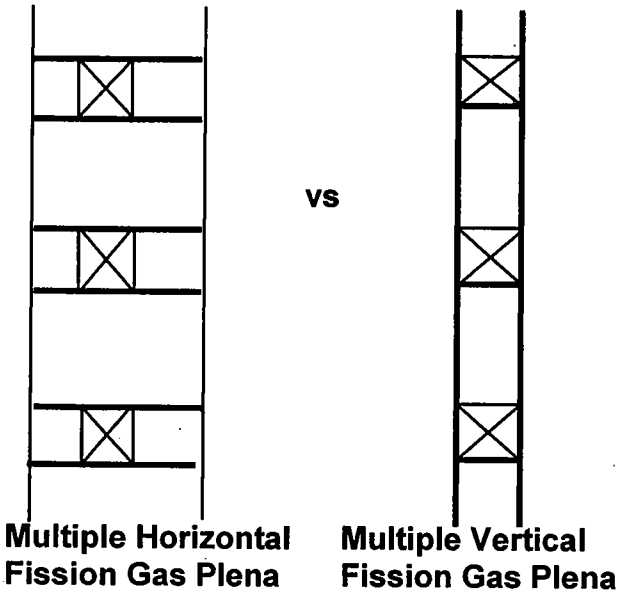


**Figure 1.7. Horizontal and Vertical Bundle Configuration with Short Pins**

### 1.3.4 Tall Vertical Single Segment Vented Pin

Unless longer length SiC/SiC composite tubing can be fabricated, the 2400 MWt pin core options will have to consider monolithic SiC cladding in conjunction with a vented pin. A vented pin would be dictated by the common assessment that the strength of monolithic SiC tubing is relatively low compared to the metal cladding used in fast reactor applications in the past. Venting is therefore the design solution for the design issues regarding refueling and depressurization events. The issues were discussed earlier. While a vented pin concept with its accompanying need for a venting system, charcoal traps, fission product holdup and pressure bleed points in the primary system, is indeed complicated, the GA GCFR 300 MWe demonstration plant had selected a vented pin design for its reference fuel 30 years ago. GA had assembled a venting system design and was having experiments performed to confirm the performance of the fuel pin with its fission product charcoal traps and filters. Moreover, GA had developed operating experience with a vented fuel element design from its Peach Bottom 1 plant design [11] which was operated for a number of years without significant difficulties. Even though Peach Bottom 1 was a thermal reactor and not a fast reactor, this operational expertise provides a starting basis. One of the major differences between the GFR design and the GCFR and Peach Bottom 1 will be the higher primary system temperatures (510 to 725°C vs 850°C on the outlet; 315°C vs 480°C on the inlet). This will have to be evaluated in the future work. The other major difference is the selection of the SiC ceramic cladding in place of the metallic cladding. U.S. Carborundum, a subsidiary of St. Gobain, has been fabricating monolothic SiC tubing for several decades. There is therefore a large database of industrial application experience with their SiC product, Hexoloy®. Figure 1.8 [10] shows a chemical process heat exchanger application which indicates that in an inert helium environment there should be no obstacles. The FUTURIX-MI irradiation test in Phoenix scheduled for early CY07 has included

Hexoloy® samples in the test train. This will provide valuable confirmation if the PIE results are positive. While the FUTURIX-MI specimens are small in dimensions, discussions with U.S. Carborundum [12] have indicated that lengths, diameters and thickness for the Hexoloy® tubing appropriate for GFR cladding can be obtained as essentially off-the-shelf items. Figure 1.9 shows samples of such tubes obtained from U.S. Carborundum. Design concept (4) utilizing such tubes for pin cladding is presented in Figure 1.10.

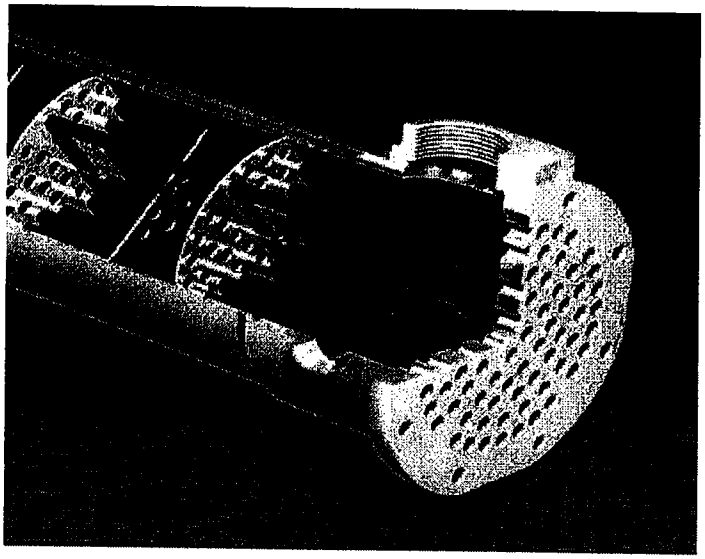

**Figure 1.8. Carborundum Hexoloy® Silicon Carbide Chemical Process Heat Exchanger Tubing**

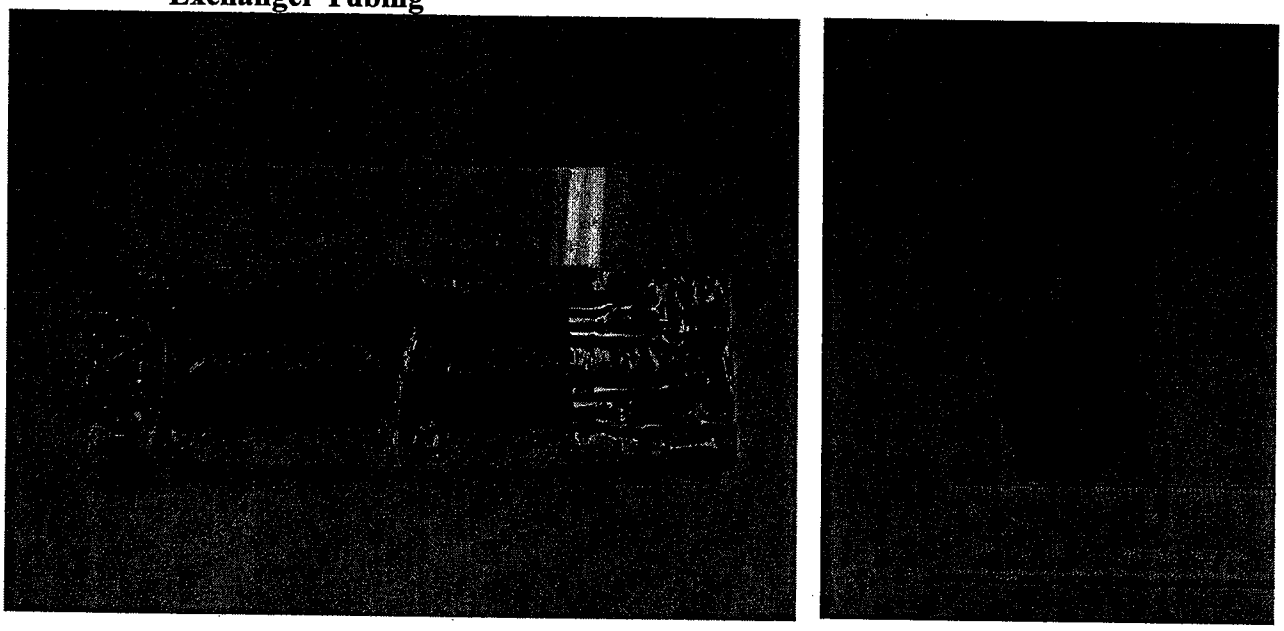

**Figure 1.9. US Carbonundum (St. Gobain) Hexoloy® (SiC) Tubing Clad**

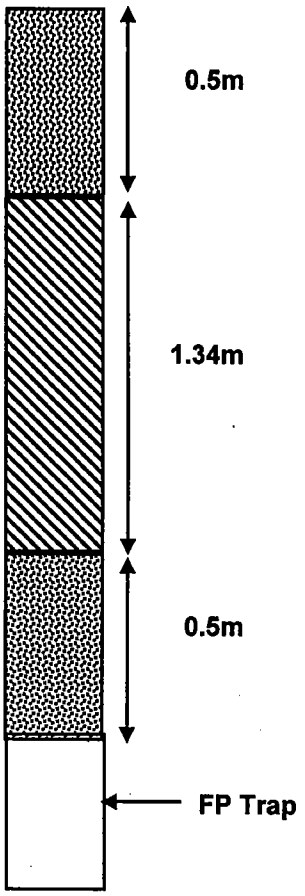


**Figure 1.10. Tall Vented Vertical Single Segment Pin**

In summary, starting from the vented GA GCFR pin design of 30 years ago with no fission gas plena and using external axial shielding, we have upper and lower reflectors of 0.5m length. There are no axial blankets. There is a 1.34m active core length. Hexalloy (SiC) tubing clad will be used. U.S. Carborundum (St. Gobain) believes [12] that

- 7mm ID/0.9mm thick/3m tubing can be supplied with high confidence
- 7mm ID/0.7mm thick/1.5m tubing can be supplied with high confidence
- 7mm ID/0.5mm thick tubing requires R&D
- 9.5mm OD/1.5mm thick, and 14mm OD/1.5mm thick tubing are standard tubing sizes available off-the-shelf.

## 1.4 Core Design Summary

Design Concept (4) is the reference pin design for the 2400 MWt backup pin core option. Future work will focus on the GA GCFR 300 MWe Demonstration plant venting system and evaluate the complications of utilizing the vertical vented fuel pin design with the Hexoloy® clad.

The 2400 MWt core layout which will utilize this pin concept is presented in Figure 1.11 [8]. This is the back-up pin core option to the 2400 MWt CEA plate core design. Details

regarding this core layout are available in [8] where the core design work was performed and documented. Chapter 2 of this report presents work on refinements to that design. Results are presented for the use of pin concept (4) with Hexoloy® clad and pin venting. Control rod worth distribution calculations were also performed and the results included here. The core fuel zone loading map is presented in Figure 1.12. It is taken from [8] since, as Chapter 2 will show, the use of Hexoloy® clad has only a minor effect on major fuel cycle parameters.

As with the last design iteration, this is a 2400 MWt core with equilibrium TRU recycle and a conversion ratio of ~1.0. It has a 3 cycle residence time and 10% average discharge burnup with 786 EFPD cycle length. There are no external blankets. The H/D ratio is .28 and the active core diameter (equivalent) is 4.77 m. This translates to a hex-to-hex active core diameter of 5.1m. Table 1.3 shows some key design dimensions. Figure 1.13 shows the fuel subassembly layout for both the fuel (only) subassembly and the fuel with control rod subassembly. Chapter 3 describes the mechanical details of the fuel bundle in the subassembly. Chapter 4 presents the results for the thermal margin and vibration analysis for the tall vertical pin concept (4). In addition thermal-fluid analyses are detailed for the short horizontal pin concept (3) and provide the justification for deleting this concept from future consideration.

**Table 1.3. Reference Design Description**

| **2400 MWt PIN CORE** | |
|---|---|
| **Fuel Assembly Geometry** | |
| Flat-to-flat of hexagonal duct (outside), mm | 215 |
| Duct wall thickness, mm | 3.7 |
| Interassembly gap, mm | 7 |
| Number of pins per core subassembly | 271 |
| Number of rings (excluding center one) | 9 |
| Number of spacers | 3 |
| Hydraulic diameter, mm | 12.2 |
| Pin pitch (average), mm | 12.6 |
| **Fuel Pin Geometry** | |
| Total pin length, m | 3.34 |
| Fuel pellet diameter, ID/ODmm (annular) | 3.02/7.37 |
| Fuel clad thickness, mm | 1.0 |
| Fuel pin diameter, mm | 9.57 |

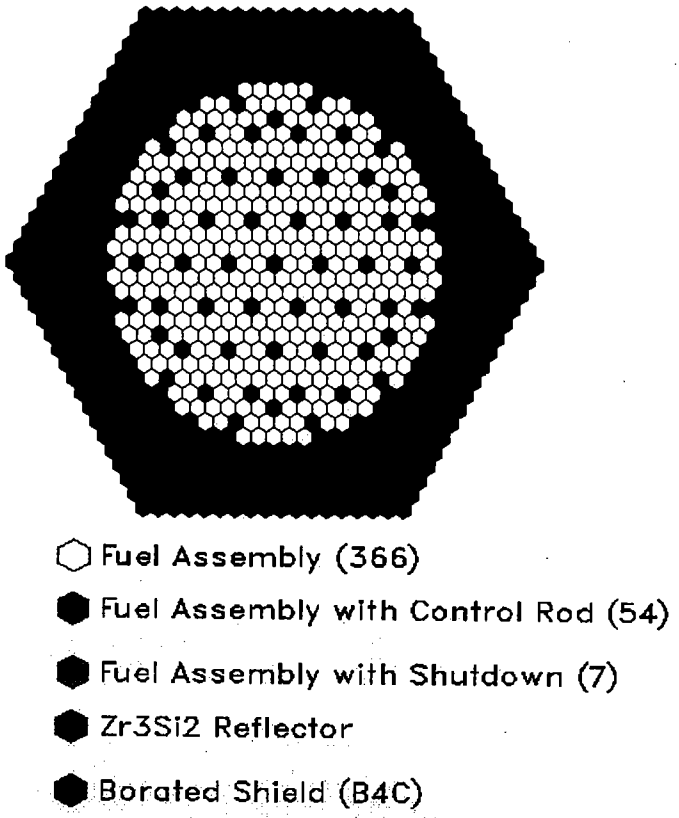


**Figure 1.11. 2400 MWt Backup Pin Core Reference Layout**

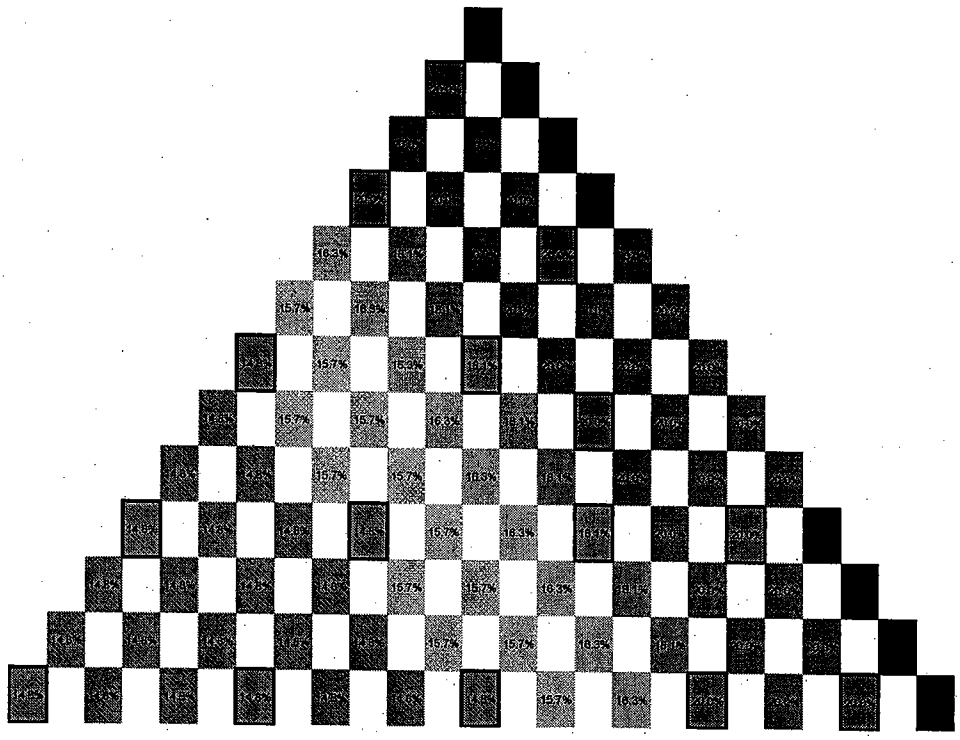

**Figure 1.12. Non-uniform Enrichment (20% TRU/HM Limit) Enrichment Zones**

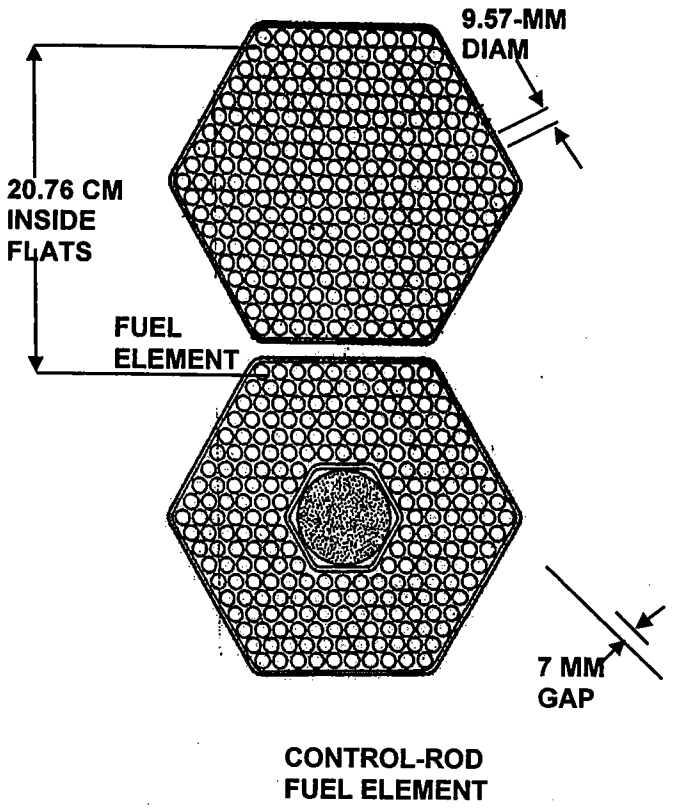


**Figure 1.13. Subassembly Design**

## 1.3 References


1. J. Rouault and T. Y. C. Wei, "Design Evaluation for GENIV Goals", GFR024, I-NERI #2001-002-F Report, March 2005.
2. A. R. Veca, H. J. Synder, P. Rau and M. Peehs, "Fuel Element Design for the 300 MWe Gas-Cooled Fast Breeder Reactor", Nuclear Engineering and Design 40 (1977) 81-99.
3. Project Staff, "EBR-II System Design Descriptions: Volume II Primary System, Chapter 2, Reactor, "Argonne National Laboratory report, 15 June 1971.
4. J. Rouault and T. Y. C. Wei, "Selection of the Concept for Point Design", GFR 021, I-NERI #2001-002-F Report, May 2004.
5. Project Staff "System Design Report" GFR023 I-NERI #2001-002-F Report, February 2005.
6. E. E. Feldman (ANL), Personal Communication, May 2004.
7. T. Mizuno (JAEA), Personal Communication, October 2003.
8. E. E. Feldman, G. A. Hoffman, R. F. Kulak, I. U. Therios and T. Y. C. Wei, "Large GFR Core Subassembly Design", ANL-GENIV-50, GENIV Gas Cooled Faster Reactor Report, Aug 2005.
9. T. Mizuno (JAEA), Personal Communication, September 2005.
10. Saint-Gobain Ceramics (www.carbo.com).

11. G. Melese and R. Katz, "Thermal and Flow Design of Helium Cooled Reactors", p. 40, ANS Publication, LaGrange Park, IL, USA, 1984.
12. J. Bevilacqua, (Saint-Golain Ceramics), Personal Communication, December 2005.

# 2. Core Neutronics Design

## 2.1 Fuel Cycle and Neutronics Modeling Approach

Full-core, equilibrium-cycle calculations were performed using the REBUS-3 fuel cycle analysis code [1]. An enrichment search was performed to determine the TRU enrichment required to achieve an end of equilibrium cycle (EOEC) unpoisoned $k_{eff}$=1.0. An external cycle time of three years and 0.1% losses of the actinides were assumed.

Region-dependent 33-group cross sections were generated with the $MC^2$-2 code [2] based on ENDF/B-V nuclear data. Beginning of cycle material compositions and temperatures from the reference design were used to generate the cross section library. The flux distributions were obtained using the nodal diffusion theory option of the DIF3D code [3].

A number of reactivity parameters were calculated by using the beginning of equilibrium cycle (BOEC) and EOEC number densities from the REBUS-3 calculations, generating individual finite-difference DIF3D cases, and new cross section sets using $MC^2$-2 for the reference conditions and the perturbed conditions. The values were calculated by eigenvalue difference. This was done with the exception of the axial and radial expansion calculations, where the unperturbed BOEC or EOEC cross section library was used. The delayed neutron fraction and prompt neutron lifetime were calculated at the BOEC and EOEC with VARI3D [4] using the real and adjoint fluxes calculated with DIF3D for the unperturbed conditions.

The reactivity effect of a depressurization accident was evaluated. The coolant pressure was assumed to fall instantaneously to atmospheric pressure throughout the system. New coolant number density was calculated at one atmosphere using the ideal gas law. The reactivity effect of instantaneous depressurization was evaluated at BOEC and EOEC.

For the expansion cases, the core volume is increased 5% by either radial or axial expansion. The number densities, except for the coolant, were reduced to conserve mass. The coolant number densities remained constant.

## 2.2 Vented Pin Configuration

The reference design is a 2400 MWt pancake (H/D ~ 0.28) core. The conversion ratio was approximately 1.0 for the three-batch scatter loading with an average 10% discharge burnup. The equilibrium-recycle fuel cycle was analyzed. Since the conversion ratio was maintained at unity, all the TRU is supplied from recycled fuel. The makeup uranium was depleted uranium. The core consists of 366 fuel (271 fuel pins) assemblies, 54 fuel assemblies (234 fuel pins) with a central control rod, and 7 fuel assemblies (234 fuel pins) with a central shutdown rod. Figure 2.1 shows the reactor layout for the reference design.

The assembly design included both fuel and control assemblies as indicated above. The fuel pins in all assemblies are the same design. The control assemblies have a centrally

located control tube which replaces 37 of the fuel pins. The details of the reference assembly design are provided in Table 2.1. The reference fuel cycle is a scatter-load 3-batch core with recycle.

A core design was developed that produced the desired performance and an acceptable power distribution [5] for a non-vented tall vertical pin. Since the previous evaluation, a number of design changes have occurred that may have effects on the neutronic design. These design changes include the use of vented fuel pins. This eliminates the need for a fission gas plenum. The upper fission gas plenum was eliminated, while the lower plenum was retained in the model to allow for a charcoal trap. Actual commercially available SiC materials are being evaluated. These materials have a significant level of boron impurities because of the manufacturing techniques. The other minor modification of significance was the gap in the fuel pins did not include helium in the original calculations. The gap was assumed to contain helium at system pressure.

Figure 2.2 shows the axial design of the fuel and control/shutdown assemblies. In the neutronics model, the end of life rod locations were modeled which places the control rods just outside the core. The control/shutdown assemblies have a central guide tube that runs the entire length of the fuel assemblies, but only the lower regions below the active core would actually contain the control element at the end of core life. This design leads to six axial regions in each fuel assembly as modeled. Starting from the top, there is a shield region containing neutron absorbing material and was modeled as an extension of the fuel assembly with the same volume fractions where the fuel is replaced by $B_4C$. In fact, this is likely to be a fixed shield that is not part of the removable assemblies. Below the upper shield is the neutron reflector region that would likely be part of the assembly and was modeled as reflector pellets ($Zr_3Si_2$) stacked on top of the fuel region. The next region is the active core or fuel region. Below the active core region is the lower reflector region. Below the reflector region is the lower plenum. Originally, there were upper and lower fission gas plenums that would be integrated into the fuel pin. Transition to vented pins eliminates the need for a fission gas plenum. However, the lower fission gas plenum was retained for use as a region that would include a fission product trap such as a charcoal filter. The some volume fractions as the reflector region are used except helium replaces the reflector pellets. The bottom region is the lower shield.

For the fuel assemblies without control rods, the upper and lower regions have the same compositions. Therefore, there are only four distinct regions, which are the fuel, reflector, shield, and plenum. For the fuel assemblies with control rods, the upper and lower regions are the same design, but the control rod will be inserted in the lower region. The control guide tube extends the entire length of the reactor and displaces fuel pins which lead to significantly different volume fractions from the fuel assembly. As a result, each axial region in the control/shutdown assembly has a different composition. This is modeled as six distinct regions, which are the three regions without control rods present (top shield, top reflector, and fuel) and the three regions with control rods present (bottom reflector, bottom plenum, and bottom shield). Table 2.2 includes the composition of the various regions in the reactor.

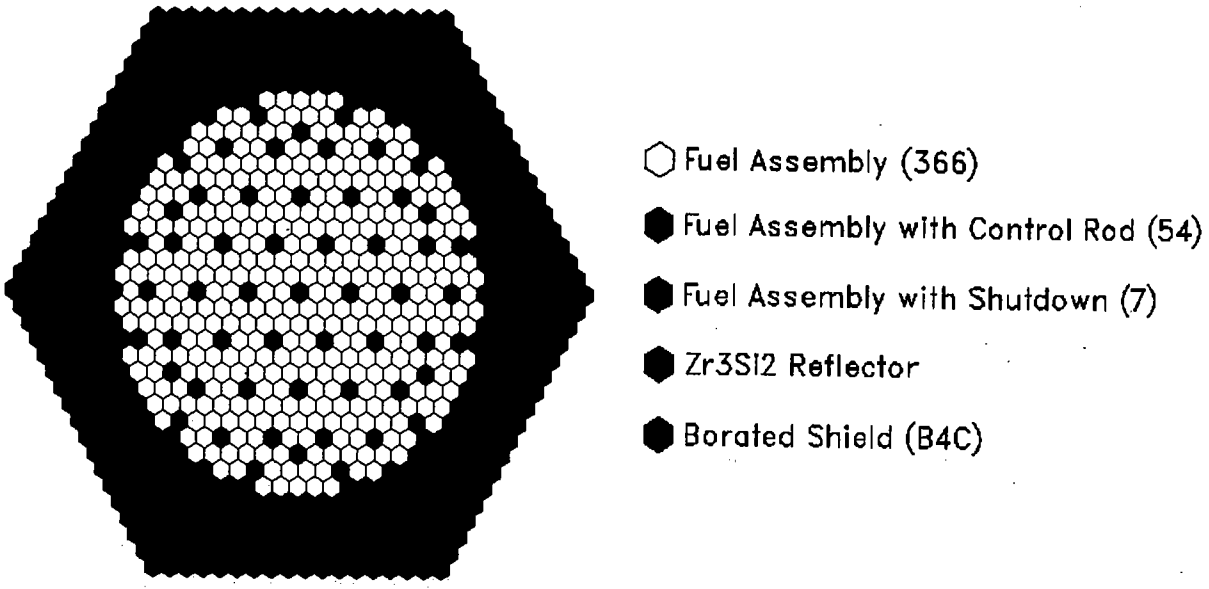


**Figure 2.1. Reference Reactor Layout.**

**Table 2.1. Equilibrium TRU Breakeven Gas-Cooled Fast Reactor Designs.**

| Assembly Type | Fuel | Control | Reflector | Shield |
|---|---|---|---|---|
| Assembly Pitch (mm) | 222 | 222 | 222 | 222 |
| Assembly Flat-to-Flat (mm) | 215 | 215 | 215 | 215 |
| Duct Thickness (mm) | 3.7 | 3.7 | 3.7 | 3.7 |
| Duct Material | SiC | SiC | $Zr_3Si_2$ | W |
| Pins | 271 | 234 | 19 | 19 |
| Pin Diameter (mm) | 9.57 | 9.57 | 40.1 | 40.1 |
| Clad Thickness (mm) | 1.00 | 1.00 | N/A | 0.019 |
| Clad Material | SiC | SiC | N/A | W |
| Pellet Outer Diameter (mm) | 7.37 | 7.37 | N/A | 38.9 |
| Pellet Inner Diameter (mm) | 3.02 | 3.02 | N/A | N/A |
| Pellet Material | (U,TRU)C | (U,TRU)C | $Zr_3Si_2$ | $B_4C$ |
| Control Rod Outer Diameter (mm) | N/A | 80.5 | N/A | N/A |
| Control Rod Cladding Thickness (mm) | N/A | 1 | N/A | N/A |
| $B_4C$ Diameter (mm) | N/A | 78.5 | N/A | N/A |

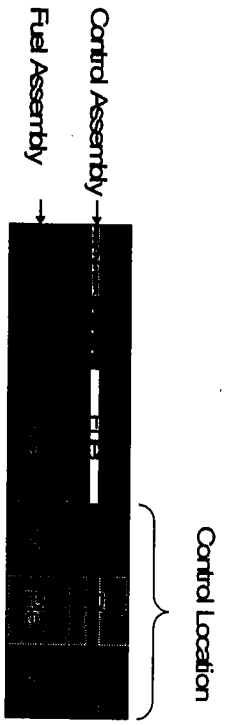


**Figure 2.2. Axial Fuel and Control Assembly Design.**

**Table 2.2. Gas-Cooled Fast Reactor Design Volume Fractions.**

| | Material | (U,TRU)C | SiC – Tube | SiC – Duct | He | $Zr_3Si_2$ | $B_4C$ | W |
|---|---|---|---|---|---|---|---|---|
| | Density (g/cc) | 13.62 | 3.20 | 3.20 | 0.00359 | 5.88 | 2.51 | 19.25 |
| Assembly | Region | Volume Fraction | | | | | | |
| Regular Fuel Assembly | Fuel | 19.2% | 17.1% | 6.3% | 54.0% | | | |
| | Reflector | | 17.1% | 6.3% | 54.0% | 22.6% | | |
| | Plenum | | 17.1% | 6.3% | 76.6% | | | |
| | Shield | | 17.1% | 6.3% | 54.0% | | 22.6% | |
| Control or Shutdown Assembly | Fuel | 16.6% | 14.8% | 6.3% | 59.4% | | | |
| | Top Reflector | | 14.8% | 6.3% | 59.4% | 19.5% | | |
| | Top Plenum | | 14.8% | 6.3% | 78.9% | | | |
| | Top Shield | | 14.8% | 6.3% | 59.4% | | 19.5% | |
| | Bottom Reflector | | 14.8% | 6.3% | 47.5% | 19.5% | 11.9% | |
| | Bottom Plenum | | 14.8% | 6.3% | 67.0% | | 11.9% | |
| | Bottom Shield | | 14.8% | 6.3% | 47.5% | | 31.4% | |
| Reflector | | | | | 30.7% | 69.3% | | |
| Shield | | | | | 34.3% | | 58.6% | 7.1% |

## 2.3 Cladding [Hexoloy ®] Boron Impurity

The use of commercially produced silicon carbide (SiC) would ideally be the approach used for production of the SiC cladding (tubes) and ducts in the vented pin design. The commercially available SiC that is being evaluated contains very significant quantities of boron impurity. The datasheets of one currently available source of SiC [5] list boron impurity level at 6900 ppm. Personnal communications with Saint-Gobain Ceramics (U.S. Carborundum Corporation) [7] confirmed the high concentrations of boron because the use of boron was integral to the manufacturing process. Since boron is not an important impurity, it is not controlled as tightly as possible. It was suggest that it was likely that boron could be more tightly controlled, but not eliminated, and the values could possibly be reduced to 3000-4000 ppm.

This high concentration of boron would have a significant reactivity effect. Using the published value of 6900 ppm B in the SiC would have a reactivity effect of approximately 1%Δk. The actual level of boron and measures to reduce it needs to be evaluated. If high levels must be tolerated, it will have significant consequences on the fuel loading required to maintain a TRU breakeven GFR design.

## 2.4 Vented Pin Core Design

A revised design for the 2400 MWt GFR [5] was completed. The GFR design was modified to utilize vented fuel pins. This eliminates the need for a fission gas plenum. Additionally, Hexoloy SiC tubes are being evaluated for use as the cladding. These pins have slightly lower density (3.1 g/cc) than was used in the previous study (3.2 g/cc) and will have boron impurity as a result of the manufacturing technique. A value of 3000 ppm of natural boron, which is on the low end of what seems practical, was assumed in the cladding. The duct walls were assumed to have the same density, but were assumed to have negligible boron impurity. Otherwise all other design parameters and constraints were retained. The split-batch design used to flatten the power profile was retained in this design. The enrichment in the inner rings was increased slightly to achieve the target cycle length. The overall performance is very similar to the previous design. Table 2.2 provides a comparison of the general design parameters. Table 2.3 provides a comparison of the safety parameters.

In general, the impact on the GFR design was negligible. The TRU loading remained nearly unchanged and the fuel volume fraction did not need to be modified. The most significant impact was the presence of the boron impurity, which significantly reduced the flux at lower energies. Figure 2.3 shows the relative change in flux for the new design relative to the old design. The absorption of neutrons by B-10 as they are slowing down greatly reduced the prompt neutron lifetime, which decreased from 2.7 μsec to 0.8 μsec at BOC.

The depressurization reactivity increased slightly and all other parameters showed relatively small differences. There were slight differences in how the depressurization reactivity was calculated. For the original designs, the entire inventory of helium was reduced to 1 atm. However, the helium inventory in the fuel pin was neglected and modeled as a void. Calculations were performed where the pins were pressurized with

helium to nominal operating conditions and then retained during the depressurization. This gave essentially the same results. This was the methodology used to calculate the depressurization of the Hexoloy design. However, the vented pin option is being evaluated to reduce the stress on the SiC cladding and therefore during depressurization the internal pressure in the pins must be reduced. This would slightly increase the depressurization reactivity because additional helium will be removed from the system during a depressurization accident.

**Table 2.2. Design Summary.**

| | Uniform | Split-Batch | Hexoloy |
|---|---|---|---|
| Power (MWt) | 2,400 | 2,400 | 2,400 |
| Height / Diameter Ratio | 0.282 | 0.282 | 0.282 |
| Cycle Length (EFPD) | 786 | 786 | 786 |
| Cycles in Core | 3 | 3 | 3 |
| Charge Enrichment (TRU/HM) | 16.5% | 15-20% | 15-20% |
| Enrichment Zones | 1 | 5 | 5 |
| BOEC Heavy Metal Loading (MT) | 56.4 | 56.6 | 56.6 |
| EOEC Heavy Metal Loading (MT) | 54.5 | 54.6 | 54.6 |
| BOEC TRU Loading (MT) | 9.6 | 10.3 | 10.5 |
| EOEC TRU Loading (MT) | 9.6 | 10.4 | 10.5 |
| Average Discharge Burnup | 10.0% | 9.9% | 9.9% |

**Table 2.3. Safety Parameters.**

| | Uniform | | Split-Batch | | Hexoloy | |
|---|---|---|---|---|---|---|
| | BOEC | EOEC | BOEC | EOEC | BOEC | EOEC |
| Delayed Neutron Fraction $x10^3$ | 3.45 | 3.39 | 3.46 | 3.40 | 3.44 | 3.39 |
| Prompt Neutron Lifetime (μsec) | 2.54 | 2.03 | 2.67 | 2.15 | 0.76 | 0.72 |
| Doppler Temperature Coefficient (¢/K) | -0.19 | -0.17 | -0.30 | -0.28 | -0.27 | -0.24 |
| Radial Expansion Coefficient ($/cm) | -0.52 | -0.53 | -0.42 | -0.41 | Not Calculated | |
| Axial Expansion Coefficient ($/cm) | -0.08 | -0.08 | -0.15 | -0.13 | Not Calculated | |
| Depressurization Reactivity ($) | 1.33 | 1.39 | 1.09 | 1.15 | 1.26 | 1.33 |

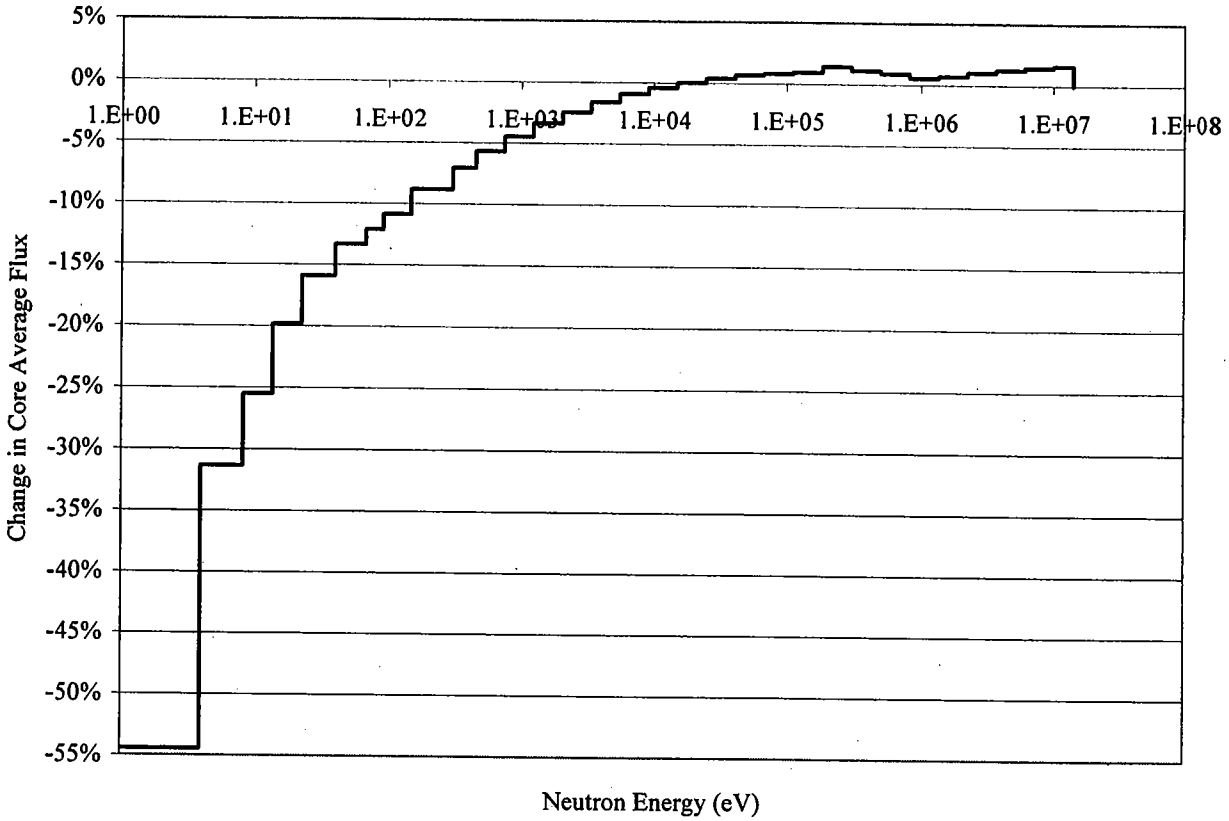


**Figure 2.3. Relative Change in Core Average Flux**

## 2.5 Control Rod Worth

Studies were performed on the 2400 MWt GFR with the non-vented vertical tall pins [5]. The results should also hold for the vented pin design. The initial designs assumed $B_4C$ control rods with natural boron, which was shown to provide sufficient reactivity for control and shutdown of the GFR. This configuration had individual rods with worths of nearly one dollar. Studies were conducted to assess the viability of using enriched and depleted boron to more uniformly distribute the reactivity amongst the available control rod locations.

The current configuration has 48 control rod locations distributed symmetrically in each sixth of the core. The average rod reactivity required for safe shutdown and burnup reactivity control is approximately \$0.18. The B-10 enrichment in the control rods required to produce a uniform reactivity worth was estimated from the reaction rates in the various control rods. The reaction rates showed that an exceedingly high B-10 enrichment would be required in the outer most control rods to produce the same reactivity as the inner most control rods because of the lower flux levels. The B-10 enrichment in the sixth inner most control rod was reduced to 8%, which reduced the reactivity of the most reactive rod from just less than \$1 to slightly more the 50¢. The second inner most set of twelve control rods were reduced in enrichment to 15% B-10, which gives each rod a reactivity of approximately 40¢. The next twelve control rods

used natural boron. The remaining control rods need to have a significant increase in B-10 enrichment in order to compensate for the loss of rod worth in the inner control rods. Enrichment of 50% for the six lowest worth control rods and 40% for the other 12 control rods provide nearly the same total rod worth as all control rods using natural boron.

The total burnup reactivity swing of the core is less than \$1. With 48 control rod locations, this equates to approximately \$0.02 per control rod. Thus, the reactivity accidents related to accidental control rod withdrawal at power will be driven by very small reactivity insertions and therefore are unlikely to be problematic. Therefore, if a high B-10 enrichment is not practical, it is quite likely that very substantial increases in individual rod worths can be safely tolerated in order to provide the necessary shutdown and safety margins.

## 2.6 Conclusions

Design changes and refinements have occurred on the 2400 MWt, low-pressure drop (H/D=0.282) design. The impact of these design changes were evaluated. The most significant refinement was the inclusion of a significant level of boron impurity in the SiC cladding. The presence of B-10 at the levels anticipated in the commercially available SiC tubing would significantly shorten the prompt neutron lifetime. The other effects would be slight increases in TRU loading and higher depressurization reactivity.

The low burnup reactivity swing and large number of control rods will result in very small reactivity insertion during operation. However, the total control rod worth of individual rods located near the center of the core was identified as a potential safety concern. The B-10 enrichment required to limit the maximum rod worth to 50¢ and spread the control rod worths more uniformly was evaluated. This required the innermost control rods to have boron enrichment reduced to approximately 8%. The control rods nearest the periphery of the core would require exceedingly high boron enrichments in order to produce a uniform rod worth. If the inner rods are limited to 50¢, the B-10 enrichment in the lowest worth rods would need to be 50% in order to give nearly the same total rod worth as the original design which was near the minimum required.

## 2.7 References


1. Toppel B. J., "A User's Guide to the REBUS-3 Fuel Cycle Analysis Capability," ANL-83-2, Argonne National Laboratory (1983).
2. Henryson II H., Toppel B. J., and Stenberg C. G., "MC2-2: A Code to Calculate Fast Neutron Spectra and Multigroup Cross Sections," ANL-8144, Argonne National Laboratory (1976).
3. Derstine K. L., "DIF3D: A Code to Solve One-, Two-, and Three-Dimensional Finite-Difference Diffusion Theory Problems," ANL-82-64, Argonne National Laboratory (1984).
4. Adams C. H., "Specifications for VARI3D – A Multidimensional Reactor Design Sensitivity Code," FRA-TM-74, Argonne National Laboratory (1975).

5. Feldman, E.E., Hoffman, E.A, Kulak, R.F., Therios, I.U., and Wei, T.Y.C., Large GFR Core Subassembly Design, Argonne National Laboratory, ANL-GENIV-050, 2005.
6. Saint-GobainCeramics (www.carbo.com/datasheets/techdata/chemanalysis.pdf).
7. Bevilacqua, J. (Saint-Gobain Ceramics), Personal Communication, December 2005.

# 3. Core Bundle Mechanical Design

## 3.1 Introduction

A mechanical design of the core bundle was done for a GFR 2400MWt plant. The preliminary design was performed in order to acquire approximate sizes for the core support structure and the assembly layout. A mechanical-structural design was done for the grid plate, lower end nozzle piece, lower and upper fuel support plates inside the assembly section, bundle restraint plates at the lower and upper ends of the assembly section, tie rods and the hexcan wrapper. The design for each component is presented in sections 3.2 through 3.6. The design details for each of the components in sections 3.3 through 3.6 are given in Appendix A through D, respectively.

## 3.2 Split Pin Assembly Layout

A schematic of the current core bundle design is depicted in Figure 3.1. The grid plate is made of 316L stainless steel and is 47 cm (18.5 in.) thick. The grid plate has holes through the thickness to accommodate the cooling requirements of the core. The total number of holes is 919 based on 366 fuel assemblies, 54 fuel assemblies with control rods, 7 fuel assemblies with shutdown, 174 reflector assemblies and 318 shield assemblies.

The nozzle for the fuel assembly is made of 316L stainless steel with a total height of 59 cm (23.2 in.), a lower inlet outer diameter of 17.2 cm (6.77 in.) and an upper inlet outer diameter of 21.5 cm (8.47 in.). The nozzle is set in the grid plate with the upper diameter section sitting 12 cm (4.77 in.) above the grid plate. The nozzle walls, in both the lower and upper diameter section, are 1 cm (0.39 in.) thick.

Fuel support plates are provided to support the fuel rods inside the assembly. The lower fuel support plate is made of 316L stainless steel and the upper fuel support plate is made of silicon carbide (SiC). The upper and lower plates are 2.54 cm (1.0 in.) thick. Core bundle restraint plates are used in both the lower and upper section of the assembly in order to contain the boron carbide ($B_4C$) shielding. These additional bundle restraint plates were designed to be 2.54 cm (1.0 in.) thick and are made of HT9 steel.

The tie rods are made of HT9 steel material with 6 rods for each assembly. Each rod is attached near the exterior hexagonal corner point of the lower and upper bundle restraint plates. The rods use a solid geometry with a 5 mm (0.2 in.) diameter and a length of 4.84 m (190.6 in.). The rods are designed to pass through the $B_4C$ shielding and the lower and upper fuel support plates near the exterior hexagonal corner points of the plates.

Additionally, the hexcan wrapper will be made of SiC material with a 3.7 mm (0.15 in.) thickness. The hexcan length is 4.84 m (190.6 in.) to accommodate the fuel pins, fuel support plates (lower and upper), lower and upper shielding, and lower and upper bundle restraint plates. The bundle restraint plates are located at the hexcan ends, which provide

the connection points for the tie rods. Essentially the tie rods and bundle restraint plates provide a compression fit to contain the hexcan internals.

The fuel pin configurations are based on the previously split pin design. The fuel pins have an active length of 134 cm (52.8 in.), a bottom and top reflector with a length of 50 cm (19.7 in.) each and a bottom and top fission gas plenum with a length of 50 cm (19.7 in.) each.

The lower and upper shielding in the hexcan is located below and above the fuel pins. The shielding is made of $B_4C$ and was estimated to be 80 cm (31.5 in.) in length for the lower shielding and 70 cm (27.6 in.) in length for the upper shielding. The shielding design and calculations are provided in [3.5].

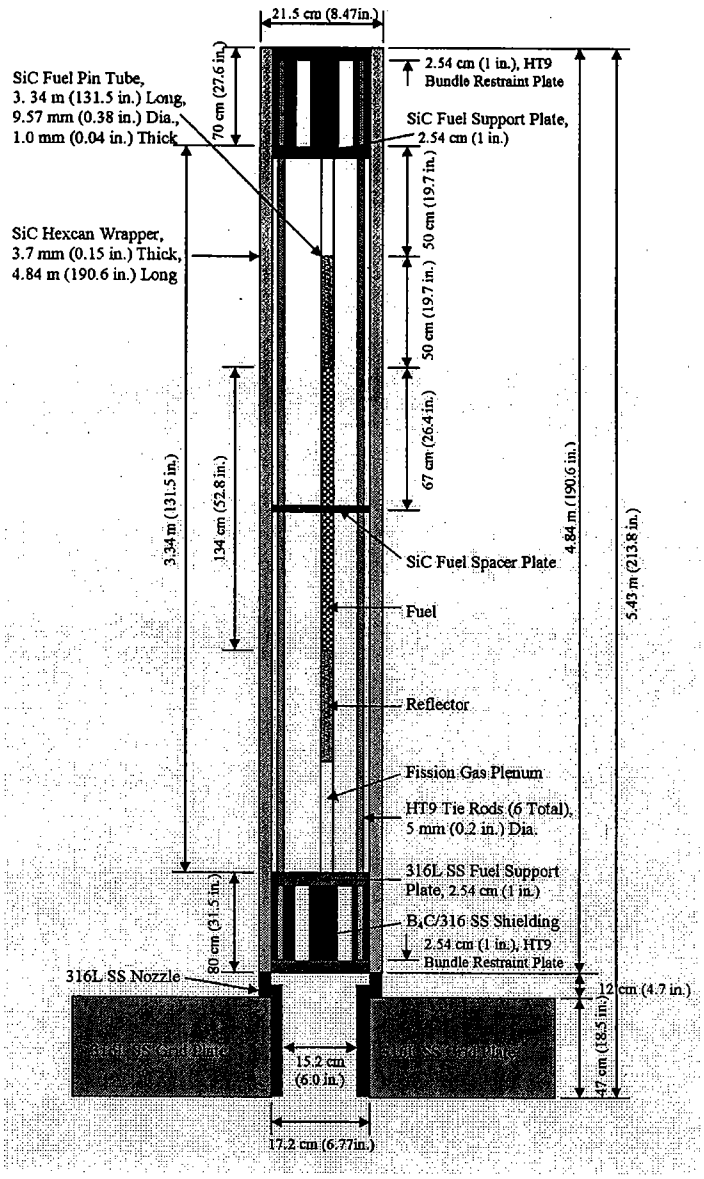


**Figure 3.1 Schematic of Core Bundle**

## 3.3 Grid Plate

The grid plate was designed with 316L stainless steel material based on the temperatures expected for the grid plate. The design temperature was 480°C (900°F) for the current design. The design of the plate was to determine the thickness necessary to support the weight of the current core design. The weight is based on the current core design which is given in Chapter 2 of this report. The computed core weights are given in Table 3.1 in terms of kilograms, metric tons (mT) and tons (2000 lbs.). The weight for each component is given and the total core weight is listed.

**Table 3.1 Core Component Weights and Total Core Weight**

| Core Assembly Weight | | | |
|---|---|---|---|
| Component | Weight (kg) | Weight (mT) | Weight (tons) |
| Fuel Assembly | 163484.8 | 163.5 | 180.2 |
| Control/Shutdown Assembly | 22558.1 | 22.6 | 24.9 |
| Reflector Assembly | 146648.8 | 146.6 | 161.7 |
| Shield Assembly | 186558.3 | 186.6 | 205.6 |
| Core Barrel | 41303.2 | 41.3 | 45.5 |
| Total | 560553.2 | 560.6 | 617.9 |

The average weight density for each component is given below. The weight calculation for each compontent is given in Appendix A. The calculations are based on using the average weight density multiplied by the corresponding volume for each component.

The materials and average weight density for the fuel assembly is given in Table 3.2. The weight density is for a regular assembly, with no control rod, which is composed of carbide fuel, cladding, hexcan duct (wrapper), axial reflectors, axial plenums and axial shields. There are 366 fuel assemblies in the core.

**Table 3.2 Weight Density for Regular Fuel Assemblies**

| Materials | Density (g/cc) | Regular Fuel Assembly (No Control Rod) | | | |
|---|---|---|---|---|---|
| | | Fuel Assembly | Axial Reflector | Axial Plenum | Axial Shield |
| Carbide Fuel | 13.62 | 19.2% | | | |
| SiC - Cladding | 3.20 | 17.1% | 17.1% | 17.1% | 17.1% |
| SiC - Duct | 3.20 | 6.3% | 6.3% | 6.3% | 6.3% |
| He | 0.003593 | 54.0% | 54.0% | 54.0% | 54.0% |
| $Zr_3Si_2$ - Reflector | 5.88 | | 22.6% | | 22.6% |
| $B_4C$ - Shield | 2.51 | | | | |
| W - Shield Structure | 19.25 | | | | |
| Average Density (g/cc) | | 3.37 | 2.08 | 0.75 | 2.08 |

The materials and average weight density for the control and shutdown fuel assembly are given in Table 3.3 and Table 3.4. The weight density in Table 3.3 is used when the control rod is present in the lower half of the fuel assembly. The weight density in Table 3.4 is used when no control rod is present in the upper half of the fuel assembly. The control and shutdown fuel assembly are made up of carbide fuel, cladding, hexcan duct (wrapper), axial reflectors, axial plenums and axial shields. There are 54 control rod fuel assemblies and 7 shutdown fuel assemblies in the core.

**Table 3.3 Weight Density for Control/Shutdown Assembly with a Control Rod**

| Materials | Density (g/cc) | Control or Shutdown Fuel Assembly | Control Rod Present | | |
|---|---|---|---|---|---|
| | | | Axial Reflector | Axial Plenum | Axial Shield |
| Carbide Fuel | 13.62 | 16.6% | | | |
| SiC - Cladding | 3.20 | 14.8% | 14.8% | 14.8% | 14.8% |
| SiC - Duct | 3.20 | 6.3% | 6.3% | 6.3% | 6.3% |
| He | 0.003593 | 59.4% | 47.5% | 47.5% | 47.5% |
| $Zr_3Si_2$ - Reflector | 5.88 | | 19.5% | | |
| $B_4C$ - Shield | 2.51 | | 11.9% | 11.9% | 31.4% |
| W - Shield Structure | 19.25 | | | | |
| Average Density (g/cc) | | 2.94 | 2.12 | 0.98 | 1.47 |

**Table 3.4 Weight Density for Control/Shutdown Assembly without a Control Rod**

| Materials | Density (g/cc) | Control or Shutdown Fuel Assembly | No Control Rod Present | | |
|---|---|---|---|---|---|
| | | | Axial Reflector | Axial Plenum | Axial Shield |
| Carbide Fuel | 13.62 | 16.6% | | | |
| SiC - Cladding | 3.20 | 14.8% | 14.8% | 14.8% | |
| SiC - Duct | 3.20 | 6.3% | 6.3% | 6.3% | 6.3% |
| He | 0.003593 | 59.4% | 59.4% | 59.4% | 59.4% |
| $Zr_3Si_2$ - Reflector | 5.88 | | 19.5% | | |
| $B_4C$ - Shield | 2.51 | | 0.0% | 0.0% | 34.3% |
| W - Shield Structure | 19.25 | | | | |
| Average Density (g/cc) | | 2.94 | 1.82 | 0.68 | 1.07 |

The materials and average weight density for the reflector assembly and shield assembly are given in Table 3.5. The reflector assembly is made of zirconium silicon reflector material and the shield assembly is made of boron carbide material and a tungsten outer structure. There are 174 reflector assemblies and 318 shield assemblies in the core.

**Table 3.5 Weight Density for Reflector and Shield Assemblies**

| Materials | Density (g/cc) | Reflector Assembly | Shield Assembly |
|---|---|---|---|
| Carbide Fuel | 13.62 | | |
| SiC – Cladding | 3.20 | | |
| SiC – Duct | 3.20 | | |
| He | 0.003593 | 30.7% | 30.7% |
| $Zr_3Si_2$ – Reflector | 5.88 | 69.3% | |
| $B_4C$ – Shield | 2.51 | | 58.6% |
| W - Shield Structure | 19.25 | | 7.1% |
| Average Density (g/cc) | | 4.08 | 2.84 |

The thickness of the grid plate was determined by using Roark's [3.1] with Table 24, case 10a "Solid Circular Plate Simply Supported; Uniformly Distributed Pressure". This is a closed formed solution based on small deflection theory. The pressure acts over the entire surface of the grid plate. The pressure is the total weight that is supported by the grid plate plus the weight of the grid plate itself. The assumption in the analysis is the total weight acts over the entire span of the grid plate. Based on a previous conceptual design of the GFR (GFR021 – May 2004) the grid plate will be designed as a simply supported structure with an outer diameter of 290 in. (7.366 m).

Using the ASME B&PV [3.2] with material properties for 316L and a total core weight of 560.6 metric Tons (617.9 Tons) the size of the grid plate can be calculated. The details of the calculations are given in Appendix A – Calculations for Grid Plate. The thickness was determined to be 47 cm (18.5 in.) thick. The thickness can accommodate both the static and other loads (service limits A, B and C from Ref. 3.2) from the core weight (including the fuel, reflectors, axial and radial shielding, nozzles, hexcan wrappers and other assembly internal structures which includes support plates, spacer plates, and tie rods). The grid plate thickness was designed to support its own weight which would be an additional 160.2 Metric Tons (176.6 Tons). This weight is a conservative value because the holes and attached nozzles are not included. The weight would be reduced by about 56.5 metric Tons (62.3 Tons) as shown in Appendix A.

## 3.4 Lower End Nozzle Piece

The nozzle is made of 316L stainless steel with a total height of 59 cm (23.2 in.) and a lower inlet outer diameter of 17.2 cm ( 6.77 in.) and an upper inlet outer diameter of 21.5 cm (8.47 in.). The nozzle is set in the grid plate with the upper diameter section sitting 12 cm (4.77 in.) above the grid plate. The nozzle walls, in both the lower and upper diameter section, are 1 cm (0.39 in.) thick. The nozzle mechanical design was to determine the required thickness to properly transfer the weight of a fuel assembly to the grid plate support.

The nozzle needs to accommodate the assembly hexcan duct. The flat-to-flat of the hexagonal duct is 215 mm for the outside dimension. The duct wall thickness is 3.7 mm. The interface between the duct and the nozzle was not designed, but there needs to be enough material to accommodate an effective interface. Thus, the thickness of the nozzle walls was chosen to be 1.0 cm thick. Additionally, a nozzle is needed for all of the assemblies of the core. So a single nozzle was designed to accommodate the fuel assembly, control / shutdown assembly, reflector assembly and the shield assembly. The details of the calculations to check the adequacy of the nozzle are given in Appendix B – Calculations for Lower End Nozzle Piece.

## 3.5 Fuel Support and Bundle Restraint (Lower / Upper Plates)

The lower fuel support plate is made of 316L stainless steel and the upper fuel support plate is made of silicon carbide (SiC). The upper and lower plates are 2.54 cm (1.0 in.) thick. In both the lower and upper section of the assembly two plates are needed in order to contain the boron carbide ($B_4C$) shielding, which are denoted as the bundle support plates. The bundle support plates were also designed to be 2.54 cm (1.0 in.) thick and made of HT9 steel material.

The design temperature was 480°C (900°F) for the current design of the lower plate. The thickness of the grid plate was determined by using Roark's [3.1] with Table 24, case 10a "Solid Circular Plate Simply Supported; Uniformly Distributed Pressure" from Reference [3.1]. The pressure acts over the entire surface of the grid plate. The pressure is the total weight that is supported by the fuel support plate plus the weight of the fuel support plate. Using the ASME B&PV [3.2] with material properties for 316L the size of the lower fuel support plate can be calculated. The details of the calculations are given in Appendix C – Calculations for Fuel Support Lower/Upper Plates. The thickness was determined to be 2.54 cm (1 in.) thick. A similar design was done for the upper plate which is subjected to a higher temperature of 850°C (1562°F). These plates support very little weight because of their location and the material used for the plates is assumed to be SiC. The thickness of the upper fuel plate was determined to be 2.54 cm (1 in.). This is the same thickness as the lower fuel plate.

## 3.6 Tie Rods / Wrapper

The tie rods were assumed to be made of HT9 steel material utilizing 6 rods at the exterior points of the lower and upper fuel support plates. HT9 was used based on the temperature range of 480°C (900°F) to 850°C (1562°F) and need to provide strength only during refueling operations. The temperature during refueling will be at 100°C (900°F). The judgment used here is based on the fact that the rods with HT9 material can handle the temperature range and have sufficient strength when needed during refueling operations. Refueling operations would require installation and removal of fuel assemblies from within the grid plate. The details of the calculations are given in Appendix D – Calculations for Tie Rods/Wrapper. The rods are designed to be solid 5 mm (0.2 in.) diameter geometry.

The hexcan wrapper was assumed to be made of SiC material because of the temperature range of 480°C (900°F) to 850°C (1562°F). A thickness of 3.7 mm (0.15 in.) was

assumed to be adequate for a postulated differential pressure of 0.5 bar which is 50,000 Pa (7.25 psi)

## 3.7 Summary and Conclusions

A scoping mechanical design has been performed for the GFR 2400MWt plant. The basic design of the core bundle has been determined. The details of the connection between the SiC hexcan wrapper and nozzle end piece would need to be investigated, as well as the internal structure connections of the fuel assemblies (i.e. fuel support connections to hexcan and connections with axial shielding). The additional margins on the service limits for both the grid plate and fuel support plates also needs to be assessed. This assessment would need to be done only after the plant design is mature enough to properly evaluate the required service limits of ASME NH in Ref. 3.2.

## 3.8 References


3.1 Roark and Young, "Formulas for Stress and Strain," 5th Edition, 1975

3.2 ASME Boiler and Pressure Vessel Code, Rules for Construction of Nuclear Facility Components, Section III, Division 1- Subsection NH, Class 1 Components in Elevated Temperature Service, 2004 Edition, July 1, 2004.

3.3 "Mark's Standard Handbook for Mechanical Engineers," 8th Edition, 1978

3.4 ASME Boiler and Pressure Vessel Code, Rules for Construction of Nuclear Facility Components, Section III, Division 1- Appendices, Appendix A-8000 Stresses in Perforated Flat Plates, 2004 Edition, July 1, 2004.

3.5 J. R. Perry, "GFR Subassembly Shielding Design Studies", Report INL/EXT-06-1152, (Jan. 2006).

# 4. Core Bundle Thermal-Hydraulic Design

The 2400 MWt helium-cooled Gas Fast Reactor (GFR) is being designed for an elevated core outlet temperature of nominally 1123 K (850°C) to achieve high electrical production efficiency using a direct-cycle system in which the turbine is included in the primary loop. In addition, this design is capable of providing process heat at temperatures that are compatible with various hydrogen production schemes. To achieve these high operating temperatures, one of the core design options that is being considered is a pin-type (U,Pu)C fuel featuring silicon carbide (SiC) cladding. SiC is an attractive alternative for the cladding in this particular application due to the fact that it has a very high melting point (~ 2700°C), and is chemically inert with both the fuel and coolant. However, the radiation performance of this material is yet to be proven. Furthermore, this refractory-type material has relatively weak mechanical properties compared to traditional iron-based alloys that have been used as cladding materials in other fast reactor applications (e.g., HT-9). On this basis, the traditional vertical core bundle design has been considered, as well as a modified horizontal cross-flow bundle design that features short pin segments. The latter design alternative is motivated by the fact that SiC cladding with improved mechanically strength properties can be fabricated, but only in very short segments (30-50 cm) based on current manufacturing technology.

For either core bundle design, analysis is required to verify suitable thermal hydraulic and mechanical performance under the normal operating conditions anticipated for GFR. The primary objective of this section is to provide these analyses in overall support of the GFR clad fuel pin design option. To this end, a general thermal hydraulic channel flow model is first developed and applied to the vertical bundle design to verify acceptable thermal hydraulic characteristics. With these results in hand, some minor modeling modifications are then made and the same analysis is carried out for the horizontal bundle design. The calculations for the horizontal design option will show that although acceptable fuel and cladding temperatures can be achieved under normal operating conditions, the overall core pressure drop exceeds that which will allow acceptable core cooling under natural convection flow conditions that would develop under postulated accident conditions. On this basis, the vertical core bundle is further analyzed to verify that the design is acceptable from the viewpoint of flow-induced vibration.

## 4.1 Vertical Pin Bundle Thermal Analysis

The objective of this section is to develop a simplified computational model that allows the fuel, cladding, and coolant gas temperatures, as well as coolant flow velocity and pressure drop, to be evaluated as a function of axial position within a vertical, parallel flow pin bundle. The basic model for calculating these variables is developed first, followed by the presentation of the ancillary correlations and property data that are utilized in the analysis. Finally, the model is applied to evaluate the thermal hydraulic characteristics for the current GFR vertical bundle design.

### 4.1.1 Model Development for Vertical Pin Bundle Case

The modeling is restricted to a single fuel pin channel of a potential GFR core design. The gas is envisioned to enter the core inlet plenum at a specified pressure ($P_o$) and

temperature ($T_o$). Furthermore, the channel mass flowrate ($\dot{m}$) is assumed to be specified. As the gas flows through the channel, it removes heat by forced convection from the adjacent clad fuel pin. Aside from entrance and exit losses at the core inlet and exit, flow friction acts to reduce the coolant pressure as the gas accelerates down the channel. In addition, grid spacers may also be present that will result in localized pressure drops at discrete locations along the channel.

Well known analytical solutions are available for the case of compressible, adiabatic flow of an ideal gas through a constant area duct including the effects of friction (i.e., the Fanno line solutions). However, these solutions are not applicable for this case since heat transfer from the fuel to the coolant occurs as the coolant flows through the core. Thus, the compressible gas flow equations that govern this case are developed in order to accurately capture the heat transfer effects.

A depiction of a control volume within the coolant channel is shown in Figure 4.1. Steady state flow conditions in a constant area (A) channel are assumed, so that variables are only a function of channel position (x). The coolant temperature (T), pressure (P), density ($\rho$), and velocity (U) are all functions of channel position. Since steady state flow is assumed, the mass flowrate in the channel is constant and conservation of mass at both edges of the control volume becomes:

$$\dot{m} = \rho UA = (\rho + d\rho)(U + dU)A = \text{constant}. \tag{4.1}$$

The analysis is further simplified by assuming ideal gas behavior. For this case, the equation of state relating local gas pressure to temperature is of the form:

$$P = \rho R_g T, \tag{4.2}$$

where $R_g$ is the ideal gas constant (2077.22 J/kg-K for helium).

The x-component of the momentum equation for the volume can be expressed in integral form as:

$$F_{S_x} + F_{b_x} = \frac{\partial}{\partial t}\int_{CV} U_x \rho dV + \int_{CS} U_x \rho \vec{U} \bullet d\vec{A}, \tag{4.3}$$

where the two terms on the left hand side of the equation denote surface and body forces, respectively. Neglecting body forces (e.g., gravity, which is an excellent assumption for gases under forced convection conditions), and also setting the differential surface force equal to that due to friction, $dF_f$, then Eq. 4.3 can be written as:

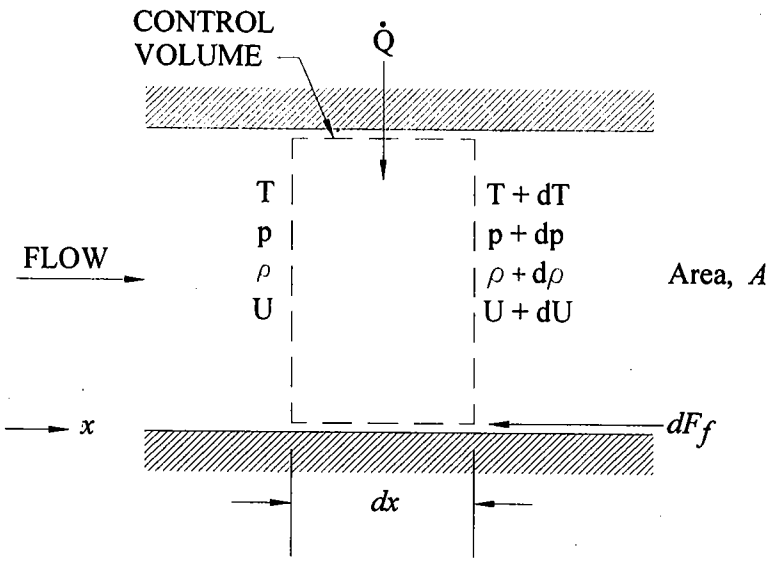


**Figure 4.1. Depiction of Channel Control Volume.**

$$-dF_f + PA - (P + dP)A = U\{-|\rho UA|\} + (U + dU)\{|(\rho + d\rho)(U + dU)A|\}. \tag{4.4}$$

With Eq. 4.1, the above expression reduces to:

$$-\frac{dF_f}{A} - dP = \rho U dU = \rho d\left(\frac{1}{2}U^2\right). \tag{4.5}$$

Pressure losses due to flow friction within the channel are modeled using the classic Darcy-Weisbach approximation; i.e.,

$$dF_f = \frac{fA}{D_h}\left(\frac{1}{2}\rho U^2\right)dx, \tag{4.6}$$

where f denotes the friction factor evaluated on the basis of the local channel flow conditions, and $D_h$ is the channel hydraulic diameter, which is defined as:

$$D_h = \frac{4A}{P_w} = \frac{4A}{2\pi R_c}, \tag{4.7}$$

where $R_c$ is the cladding outer radius. Expressions for the friction factor and other ancillary correlations and property functions required to carry out the analysis are provided later in this section.

Substitution of Eq. 4.6 into Eq. 4.5 and rearranging terms results in the following first order ordinary differential equation that relates the local channel pressure to the flow velocity:

$$\frac{dP}{dx} = -\frac{f}{D_h}\frac{\rho U^2}{2} - \rho\frac{d}{dx}\left(\frac{1}{2}U^2\right). \tag{4.8}$$

As noted at the beginning of this section, the core inlet plenum pressure, $P_o$, is taken as a specified constant. Assuming that the pressure loss from the inlet plenum into the core can be characterized by an entrance loss coefficient, $K_{entr}$, then the pressure at the channel inlet can be approximated as:

$$P(x = 0^+) = P_o' = P_o - \frac{K_{entr}}{2}\rho_o U_o^2, \tag{4.9}$$

where $\rho_o$ and $U_o$ are evaluated from Eqs. 4.1 and 4.2, along with the fact that the inlet plenum gas temperature, $T_o$, is also a specified constant. Note that Eq. 4.9 is the initial condition for the integration of the pressure loss equation, Eq. 4.8. Utilizing an identical approach, then the pressure in the core exit plenum can also be evaluated once the local flow conditions at the core exit have been calculated with an assumed exit loss coefficient, $K_{exit}$. Finally, pressure losses across grid spacers located at discrete locations along the channel can evaluated based on local flow conditions with the definition of a grid spacer loss coefficient, $K_{grid}$. Correlations for these various loss coefficients are provided in Section 4.1.2.

Now that an equation for the channel pressure loss has been developed, a second equation governing the coolant temperature evolution is required. Conservation of energy for the control volume shown in Figure 4.1 can be written in integral form as:

$$\dot{Q} = \frac{\partial}{\partial t}\int_{CV}\left(u + \frac{U^2}{2}\right)\rho dV + \int_{CS}\left(u + \frac{U^2}{2} + P\upsilon\right)\rho\vec{U}\bullet d\vec{A}, \tag{4.10}$$

where u is the gas internal energy, $\upsilon$ is specific volume, and $\dot{Q}$ is heat transfer rate into the control volume due to convection from the pin surface in contact with the volume. Expansion of Eq. 4.9 at the control volume boundaries under the assumed conditions yields:

$$\begin{aligned}\dot{Q} = {} & \left(u + \frac{U^2}{2} + P\upsilon\right)\{-|\rho UA|\} + \\ & \left[u + du + \frac{U^2}{2} + d\left(\frac{U^2}{2}\right) + P\upsilon + d(P\upsilon)\right]\{|(\rho + d\rho)(U + dU)A|\}\end{aligned} \tag{4.11}$$

The relationship between the gas specific enthalpy and internal energy is of the form:

$$h = u + P\upsilon. \tag{4.12}$$

With Eqs. 4.1 and 4.12, then Eq. 4.11 simplifies to:

$$\dot{Q} = \dot{m}\left[dh + d\left(\frac{U^2}{2}\right)\right]. \tag{4.13}$$

The heat transfer rate into the control volume can be expressed in differential form as:

$$\dot{Q} = 2\pi R_c h_{con}(T_s - T)dx, \tag{4.14}$$

where $h_{con}$ is the forced convection heat transfer coefficient, and $T_s$ is the local cladding surface temperature in contact with the control volume. With Eq. 4.14 and the definition of specific enthalpy, $h = c_p T$, then Eq. 4.13 can be written as:

$$\frac{dT}{dx} = \frac{2\pi R_c h_{con}(T_s - T)}{c_p \dot{m}} - \frac{1}{c_p}\frac{d}{dx}\left(\frac{U^2}{2}\right), \tag{4.15}$$

where $c_p$ is the gas specific heat at constant pressure. The above equation is subject to the initial condition:

$$T(x = 0) = T_o. \tag{4.16}$$

Equations 4.8 and 4.15, subject to the initial conditions defined in Eqs. 4.9 and 4.16, constitute the initial value problem governing the coolant temperature and pressure evolution along the length of the channel. To carry out the integration, it is convenient to eliminate the local gas density and flow velocity from these equations. Utilizing Eqs. 4.1-4.2 to accomplish this objective, the following two equations are obtained:

$$\frac{dP}{dx} = -\left(1 - \frac{\omega^2 T}{R_g P^2}\right)^{-1}\left\{\frac{\omega^2}{R_g P}\frac{dT}{dx} + \frac{f}{D_h}\frac{\omega^2}{2R_g}\frac{T}{P}\right\}, \tag{4.17}$$

$$\frac{dT}{dx} = \left(1 + \frac{\omega^2 T}{c_p P^2}\right)^{-1}\left\{\xi(T_s - T) + \frac{\omega^2 T^2}{c_p P^3}\frac{dP}{dx}\right\}, \tag{4.18}$$

where:

$$\omega = \frac{R_g \dot{m}}{A}; \quad \xi = \frac{2\pi R_c h_{con}}{c_p \dot{m}}. \tag{4.19}$$

Equations 4.17-4.18 constitute two equations in two unknowns for the coolant pressure and temperature. Using Eq. 4.17 to eliminate the pressure derivative yields the following explicit solution for the temperature derivative:

$$\frac{dT}{dx} = \left(1 + \frac{\omega^4 T^2}{R_g c_p P^4 \left(1 - \frac{\omega^2 T}{R_g P^2}\right)\left(1 + \frac{\omega^2 T}{c_p P^2}\right)}\right)^{-1} \left\{ \frac{\xi(T_s - T)}{\left(1 + \frac{\omega^2 T}{c_p P^2}\right)} - \frac{f\omega^4 T^3}{2D_h R_g c_p P^4 \left(1 - \frac{\omega^2 T}{R_g P^2}\right)\left(1 + \frac{\omega^2 T}{c_p P^2}\right)} \right\} \quad (4.20)$$

With this expression, the explicit equation for the pressure derivative is also known through Eq. 4.17.

The final parameter in Eqs. 4.17 and 4.20 that requires evaluation is the cladding outer surface temperature in contact with the coolant, $T_s$. An expression for this variable is developed by solving the local conduction heat transfer equations in the fuel and cladding regions assuming that axial conduction is much less than the radial component. With this assumption, then the equations governing the fuel and cladding temperature distributions are of the form:

$$\frac{1}{r}\frac{\partial}{\partial r}\left(k_f \frac{\partial T_f}{\partial r}\right) + \dot{Q}_f(x) = 0, \quad (4.21)$$

$$\frac{1}{r}\frac{\partial}{\partial r}\left(k_c^{eff} \frac{\partial T_c}{\partial r}\right) = 0, \quad (4.22)$$

where k is thermal conductivity, subscripts f and c denote fuel and cladding regions, respectively, and $\dot{Q}_f(x)$ is the fuel volumetric fission power density that is a function of axial position within the core. A simple model for the power distribution is provided in Section 4.1.2. In addition, $k_c^{eff}$ has been defined as the effective cladding thermal conductivity that includes the heat transfer resistance in the gap between the cladding and fuel; i.e.,

$$k_c^{eff} = \frac{k_c}{1 + \frac{k_c}{h_{gap}\delta_c}}, \quad (4.23)$$

The boundary condition on the temperature at the fuel inner radius $R_i$ is of the form:

$$\left.\frac{\partial T_f}{\partial r}\right|_{r=R_i} = 0. \quad (4.24)$$

Continuity between temperature and heat flux is also required at the fuel/gap interface; i.e.,

$$T_f\big|_{r=R_f} = T_c\big|_{r=R_f}; \quad k_f \left.\frac{\partial T_f}{\partial r}\right|_{r=R_f} = k_c^{eff} \left.\frac{\partial T_c}{\partial r}\right|_{r=R_f}, \quad (4.25)$$

where $R_f$ is the fuel pellet radius. Finally, the energy balance at the interface between the cladding and coolant is of the form:

$$-k_c^{eff}\left.\frac{\partial T_c}{\partial r}\right|_{r=R_c} = h_{con}(T_c|_{r=R_c} - T) = h_{con}(T_s - T). \tag{4.26}$$

With Eqs. 4-24-4.26, Eqs. 4.21-4.22 can be integrated in a straightforward manner. This effort yields the following solution for the cladding surface temperature in terms of the local fission power, cladding and fuel pellet dimensions, and the convective heat transfer coefficient:

$$T_s - T = \frac{\dot{Q}_f R_f^2}{2h_{con}R_c}\left(1 - \frac{R_i^2}{R_f^2}\right) \tag{4.27}$$

The above expression is sufficient to close the initial value problem given by Eqs. 4.9, 4.16-4.17, and 4.20. However, a few additional useful expressions can also be deduced from the fuel and cladding temperature profile solutions. This includes the following expressions for the peak fuel pellet centerline temperature and the pellet outer surface temperature:

$$T_f|_{r=R_i} = T + \frac{\dot{Q}_f R_f^2}{2k_c^{eff}}\left(1 - \frac{R_i^2}{R_f^2}\right)\left\{\ln\left(\frac{R_c}{R_f}\right) + \frac{k_c^{eff}}{2k_f} + \frac{k_c^{eff}}{h_{con}R_c}\right\}, \tag{4.28}$$

$$T_f|_{r=R_f} = T_s + \frac{\dot{Q}_f R_f^2}{2k_c^{eff}}\ln\left(\frac{R_c}{R_f}\right). \tag{4.29}$$

With the fuel surface temperature defined, then the following expression for the cladding inner surface temperature can be developed in a straightforward manner:

$$T_c|_{r=R_f} = \frac{h_{gap}T_f|_{r=R_f} + (k_c/\delta_c)T_s}{h_{gap} + k_c/\delta_c}. \tag{4.30}$$

The above expression corresponds to the local peak cladding temperature, which is an essential parameter that must be considered in any core design. Before the above equations can be numerically integrated, a few supporting correlations are required. These correlations are provided in the next section.

## 4.1.2 Ancillary Correlations for Vertical Pin Bundle Case

To carry out the integration, a correlation for evaluating the convective heat transfer coefficient as a function of the channel flow conditions is required. For the purposes of this work, this coefficient is evaluated using the classic Dittus-Boelter correlation; i.e.,

$$h_{con} = \begin{cases} \left(\frac{7.6k}{D_h}\right); & Re < 2300 \\ \\ 0.023 Re^{0.8} Pr^{0.4} \left(\frac{k}{D_h}\right); & Re \geq 2300 \end{cases}, \tag{4.31}$$

where the coolant Reynolds and Prandtl numbers are defined as:

$$Re = \frac{\rho U D_h}{\mu}; \qquad Pr = \frac{\mu c_p}{k}, \tag{4.32}$$

and $\mu$ is the gas viscosity. For the purposes of this analysis, the gas specific heat is assumed to be constant at 5220 J/kg-K. However, for helium the thermal conductivity and viscosity are sensitive to temperature. The following correlations [4.1] are used to evaluate the conductivity and viscosity based on the local gas temperature:

$$\begin{aligned} k &= 2.774 \bullet 10^{-3} T^{0.701} \ \text{W/m} - \text{K}, \\ \mu &= 3.953 \bullet 10^{-7} T^{0.687} \ \text{kg/m} - \text{sec}, \end{aligned} \tag{4.33}$$

where T is in degrees Kelvin.

Aside from the convective heat transfer coefficient, correlations for the local friction factor and form loss coefficients are required. For the purposes of this analysis, the coolant flow in the channel is assumed to be turbulent, for which the friction factor can be evaluated with the Blasius correlation; i.e.,

$$f = \frac{0.3164}{Re^{0.25}} \tag{4.34}$$

As discussed by Kejzlar [4.2], entrance form loss coefficients vary with Reynolds number in the laminar/turbulent transition region (i.e., Re < $10^4$-$10^5$). For typical entrance conditions, the correlation for the loss coefficient is given as [4.3]:

$$K_{entr} = \frac{30}{Re} + K_{turb} \tag{4.35}$$

where $K_{turb}$ is the loss coefficient for highly turbulent flow. For this work, it is assumed that $K_{turb} = 0.5$. Furthermore, the exit loss coefficient is assumed to be constant at $K_{exit} = 0.357$.

Form losses on grid spacers are also highly important for pin bundle designs since pressure losses across these elements can constitute a significant fraction of the total bundle pressure drop [4.2]. Rehme [4.4] made extensive measurements of pressure drops for various grid spacer designs and was able to correlate the data in the following manner:

$$K_{grid} = \varepsilon^2 C_D \tag{4.36}$$

where $\varepsilon$ is the ratio of the projected grid cross-sectional area to the open channel flow area (typically $\varepsilon = 0.35$) and $C_D$ is a modified drag coefficient that is correlated as [4.2]:

$$C_D = \begin{cases} 6.0 + \dfrac{3.2 \bullet 10^5}{Re^{1.3}}; & Re > 4000 \\ \\ 6.0 + \dfrac{2.9 \bullet 10^4}{Re}; & Re < 4000 \end{cases} \tag{4.37}$$

Finally, one of the modeling objectives of this work is to examine the effects of non-uniform axial fission power distribution on the thermal-hydraulic characteristics. In this case, if $x = 0$ corresponds to the core axial centerline, then the axial power distribution $\dot{Q}_f(x)$ can be approximated using a chopped cosine model; i.e.,

$$\dot{Q}_f(x) = \dot{Q}_f^{ave} P^* \cos\left(\frac{\pi x}{2a_{ex}}\right) \tag{4.38}$$

where $a_{ex}$ is the extrapolation distance outside the core at which the neutron flux tends to zero, $\dot{Q}_f^{ave}$ is the average fission power density, and $P^*$ is the peak-to-average axial power density ratio. The extrapolation distance is found by solution of the following transcendental equation:

$$P^* = \frac{\pi L_f}{4a_{ex} \cos\left(\dfrac{\pi L_f}{4a_{ex}}\right)} \tag{4.39}$$

where $L_f$ is the active fuel length of the core.

### 4.1.3 Results and Discussion

The previous sections have outlined the overall approach for evaluating the gas temperature and pressure, as well as fuel and cladding temperatures, as a function of axial position given the inlet plenum pressure and temperature, and the coolant channel mass flowrate. The purpose of this section is to apply the model to the current GFR vertical bundle design to verify acceptable thermal-hydraulic characteristics. But before this is

done, the model is benchmarked against results obtained previously by Feldman et al. [4.5] with a model that assumes a flat axial power profile in the core (i.e., $P^*=1$). The reference bundle design data are provided in Table 4.1, along with thermal-hydraulic information that was used for the benchmark. Key results obtained with the two models are shown in Table 4.2. The core bundle theoretical pumping power (i.e., total bundle volumetric flowrate times pressure drop) has also been calculated as part of the current analysis and is shown in Table 4.2 for the standard 271 pin hexagonal bundle design [4.5]. As is evident, the agreement between the two models is quite close. Slight differences are noted, which may be due to the fact that Feldman et al. [4.5] utilized a better heat transfer model across the helium-filled gap between the pellet and cladding that included both radiation and conduction heat transfer, whereas the current model only treats the conduction component. Nonetheless, the agreement is deemed to be reasonable (i.e., within 0.5 %).

**Table 4.1. Model Input Parameters.**

| Input Parameter | Value |
|---|---|
| Fuel thermal conductivity | 11.02 W/m-K |
| Fuel pellet ID | 3.00 mm |
| Fuel pellet OD | 7.37 mm |
| Average fuel power density | 451 $MW/m^3$ |
| Axial power peaking factor | 1.00 or 1.21 |
| Gap width | 0.10 mm |
| Fuel/clad gap conductance[a] | 4.4 $kW/m^2$-K |
| Clad thermal conductivity | 20.0 W/m-K |
| Clad thickness | 1.00 mm |
| Clad OD | 9.57 mm |
| Pin pitch | 12.56 mm |
| Channel hydraulic diameter | 8.60 mm |
| Channel flow area | 0.65 $cm^2$ |
| Active fuel length | 1.344 m |
| Lower reflector length | 1.0 m |
| Upper reflector length | 1.0 m |
| Total fuel pin length | 3.344 m |
| Inlet plenum pressure | 7.0 MPa |
| Inlet gas temperature | 753 K |
| Channel mass flowrate | $1.125 \bullet 10^{-2}$ kg/s |
| Entrance loss coefficient | 0.5 |
| Exit loss coefficient | 0.357 |
| Number of spacer grids | 3 |
| Grid spacer locations | 1.0 m, 1.67 m, 2.34 m |
| Grid spacer area reduction, $\varepsilon$ | 0.35, 0.35, 0.35 |

[a]Assumes conduction across a helium filled gap.

**Table 4.2. Model Benchmark Results for a Flat Axial Core Power Profile ($P^*=1$).**

| Calculated Quantity | Ref. [4.5] | Current Model |
|---|---|---|
| Channel exit velocity | 57.99 m/sec | 58.11 m/sec |
| Maximum fuel temperature | 1533 K | 1526 K |
| Maximum clad temperature | 1317 K | 1318 K |
| Core pressure drop | 54.83 kPa | 54.64 kPa |
| Assembly pumping power | - | 55.77 kW (0.95 %) |

Key results calculated with the model for the standard vertical bundle design [4.5] are shown in Table 4.3 for the case of a power peaking factor of 1.21. Also shown are the core hot channel results obtained assuming a hot channel power of 125 % of nominal (i.e., 564 $MW/m^3$ fuel power density). In addition, data plots showing the axial evolution of key parameters (i.e., flow velocity, temperatures, and pressure) are shown in Figure 4.2, while Figures 4.3 and 4.4

provide ancillary plots of fuel power density distributions and channel convective heat transfer coefficients. Note that this particular assembly design assumes that three grid spacers are used; the adequacy of this approach from the viewpoint of minimizing flow-induced vibration is addressed in Section 4.3.

As is evident by comparing Tables 4.2 and 4.3, the inclusion of a more realistic axial cosine power distribution reduces the predicted peak fuel and cladding temperatures by 63 and 59 K, respectively. The reason for this becomes evident upon examination of Figure 4.2(b). In particular, power peaking near the core center moves the peak fuel and cladding temperatures near this location. However, the coolant gas temperature at this location is still relatively cool compared to the core exit temperature. Since coolant temperature establishes the baseline for the fuel and cladding temperature increments (see Eqs. 4.27-4.28 and 4.30), this causes a reduction in the calculated peak temperatures relative to the flat power profile case. As is evident from Figure 4.2(b), peak fuel and cladding temperatures are located at the core exit for the flat profile case.

Aside from fuel and cladding temperature variations, the inclusion of a cosine power distribution is noted to have very little effect on other key channel thermalhydraulic characteristics. In particular, comparison of Tables

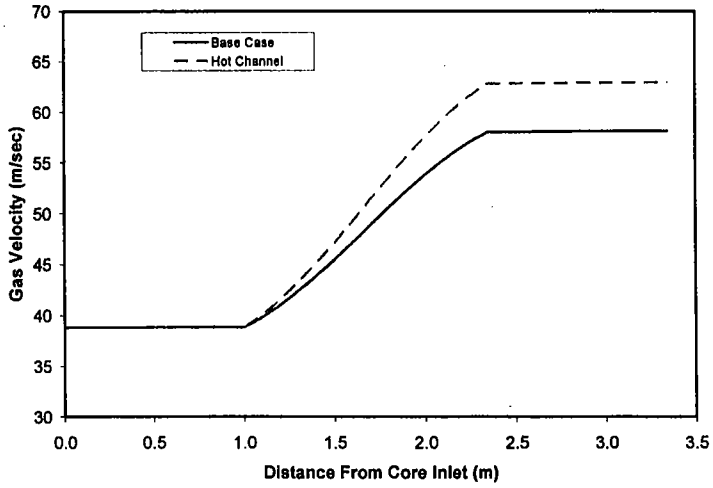


(a)

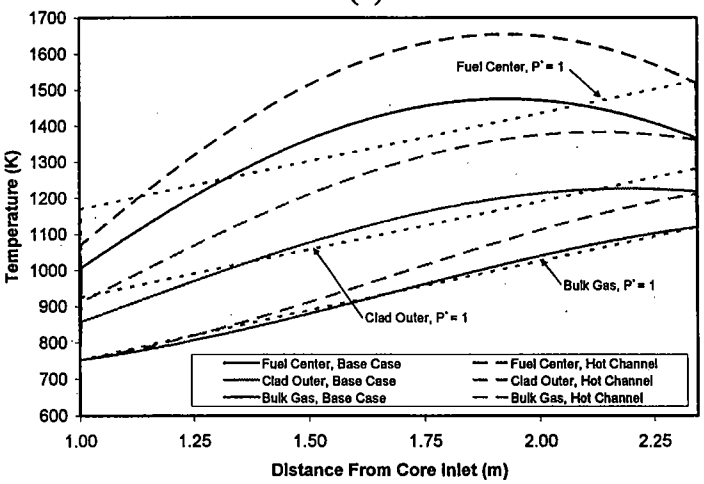


(b)

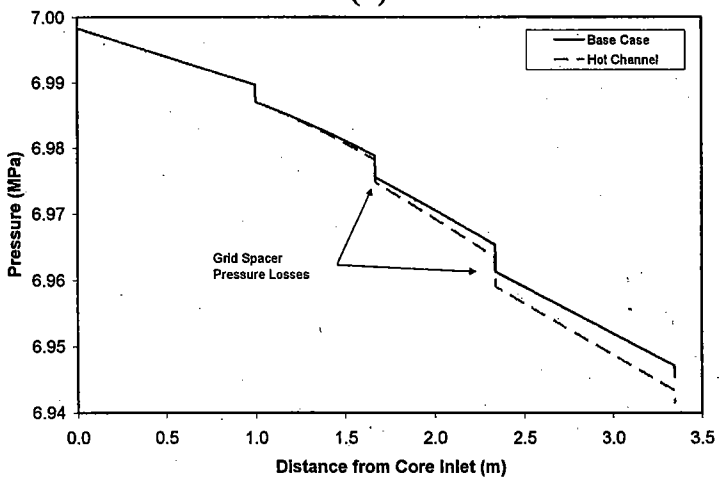


(c)

**Figure 4.2. Thermalhydraulic Results for Vertical Bundle Design: a) Channel Velocities, b) Temperatures, and c) Pressures.**

**Table 4.3. Key Thermalhydraulic Results for Standard Core Bundle Designs with Cosine Axial Power Distribution ($P^*$=1.21).**

| Calculated Quantity | Base Case | | Hot Channel (125 % Nominal Power) | |
|---|---|---|---|---|
| | Value | Distance from Core Inlet | Value | Distance from Core Inlet |
| Maximum gas velocity | 58.12 m/sec | 3.34 m | 62.93 m/sec | 3.34 m |
| Max. fuel temperature | 1475 K | 1.93 m | 1654 K | 1.93 m |
| Max. clad temperature | 1258 K | 2.13 m | 1383 K | 2.13 m |
| Bundle ΔP | 54.64 kPa | | 58.54 kPa | |
| Bundle mass flowrate (271 pin) | 3.048 kg/sec | | 3.048 kg/sec | |
| Core mass flowrate | 1249 kg/sec | | 1249 kg/sec | |
| Assembly pumping power | 55.78 kW (0.95 %) | | 64.69 kW (0.88 %) | |

4.2 and 4.3 indicates that bundle pressure drop, pumping power, and maximum gas velocity are virtually identical. This is the expected behavior since, based on conservation of energy, the coolant conditions at the core exit are the same for either case.

Further examination of Table 4.3 indicates that peak fuel and cladding temperatures for the hot channel are increased to 1654 K and 1383 K, respectively, relative to the nominal channel conditions (i.e., temperature increments are +179 K and +125 K for the fuel and cladding). In lieu of orificing at the bundle inlets, maximum flow velocity and channel pressure drop for the hot channel would be increased by ~ 10 % to ~ 64 m/sec and ~ 59 kPa, respectively, assuming the same mass flowrates for the two different cases.

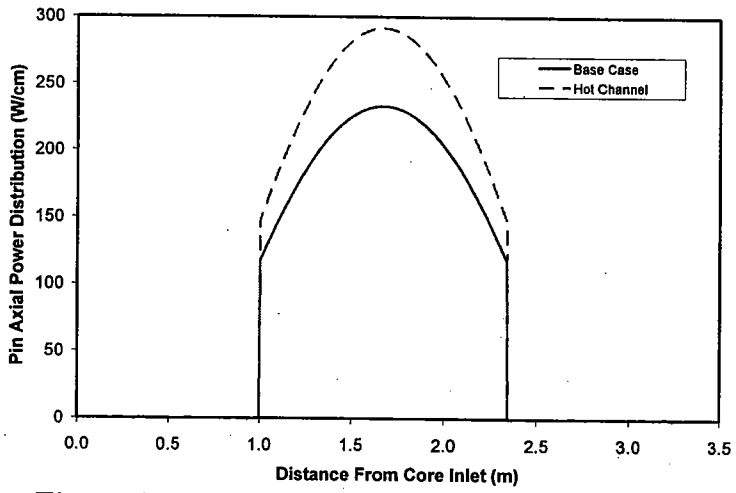


**Figure 4.3. Axial Fuel Fission Power Distributions.**

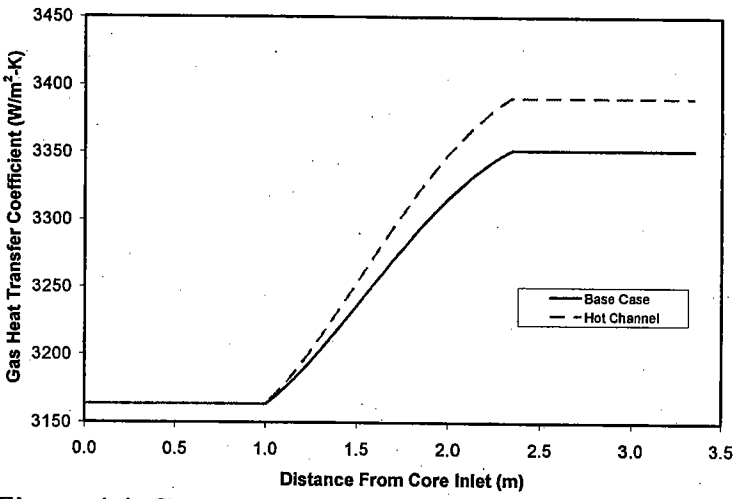


**Figure 4.4. Convective Heat Transfer Coefficients, $h_{con}$.**

## 4.2 Horizontal Pin Bundle Thermal Analysis

The previous section has outlined an approach for evaluating the thermal hydraulic performance of potential GFR core bundle designs for the case of vertical channel flow. Since the reference GFR core design features SiC cladding, it is also worthwhile to explore the possibility of a cross-flow core design since high strength SiC tubing can only be manufactured in short lengths (up to ~ 50 cm). The objective of this section is to provide the modeling basis for exploring this possibility. To that end, the required modeling modifications and ancillary correlations for examining a cross-flow core design are described first, followed by the presentation of a set of parametric calculations that illustrate the thermal hydraulic performance of this core type for the current GFR design conditions.

### 4.2.1 Modeling Modifications for Horizontal Pin Bundle Case

The purpose of this section is to define appropriate modifications to the vertical bundle flow model developed in the previous section so that the model can be applied to the case of a cross-flow core design. A conceptual drawing that illustrates key attributes of this type of bundle is provided in Figure 4.5. In plan view, the bundle would most likely be square to minimize complications in the fuel loading scheme. Although both inline or staggered pin layouts would be feasible, the inline layout is adopted for this work since it would most likely be the easiest for the incorporation of vertically inserted control "blades" into the bundle design (by removal of one or more vertical rows of pins).

As shown in Figure 4.5, the modeling considers a horizontal array of fuel pins with transverse (perpendicular to flow) and longitudinal (parallel to flow) pin pitches of $S_T$ and $S_L$, respectively. The pins are installed in a bundle shroud of width $B_W$ and breadth $B_L$. The vertical length of the active fuel region is defined as $L_f$. In the analysis that follows, it is convenient to define dimensionless pin transverse and longitudinal pitches as:

$$\hat{S}_T = \frac{S_T}{D_c}; \quad \hat{S}_L = \frac{S_L}{D_c} \tag{4.40}$$

where $D_c = 2R_c$ is the cladding outer diameter.

With the nomenclature defined, the first task is to modify the flow pressure drop equation, Eq. 4.8, for the case of cross flow. In general, the pressure drop across a tube bundle in cross-flow is correlated in terms of a hydraulic drag coefficient, or Euler number, $\zeta$, as:

$$\Delta P = \zeta \frac{\rho U^2}{2} n \tag{4.41}$$

where n is the number of tube rows in cross-flow (viz., $n = L_f / S_L$) and, in this application, U is the average gas velocity in the minimum free-flow area in the bundle. Correlations for $\zeta$ are provided in the next subsection. For the current case of an in-line bundle with perpendicular cross-flow (i.e., yaw angle of 90°), the velocity U is related to the free-stream velocity, $U_o$, in the open channel flow area, $B_W \cdot B_L$, as:

$$U = \frac{\hat{S}_T}{\hat{S}_T - 1} U_o \qquad (4.42)$$

With the overall bundle pressure drop defined in Eq. 4.41, then the differential pressure drop due to flow friction can be expressed as:

$$dF_f = \frac{A\zeta}{S_L}\left(\frac{1}{2}\rho U^2\right)dx \qquad (4.43)$$

Note that this expression is the analog of the Darcy-Weisbach approximation used to evaluate the flow friction pressure drop in Eq. 4.6. Substitution of this expression into the force balance given by Eq. 4.5 yields the following first order differential equation that approximately relates local channel pressure to flow velocity for the case of bundle cross-flow:

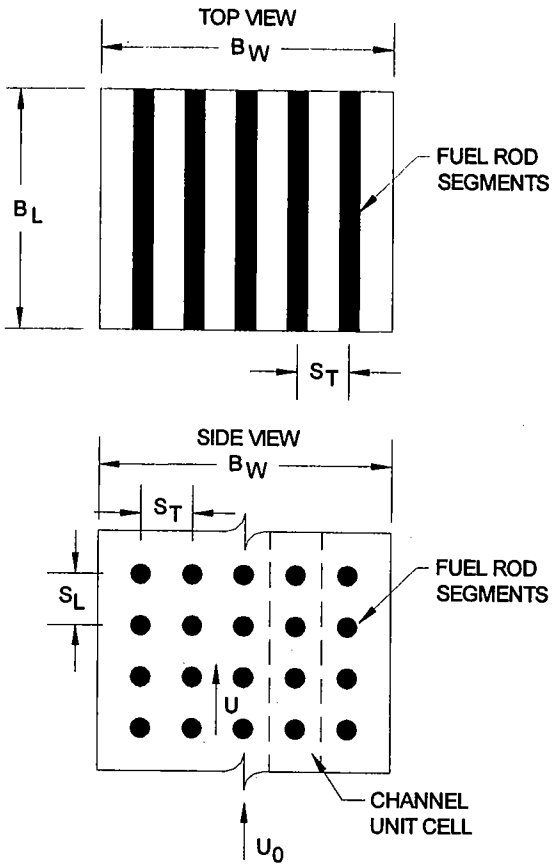


**Figure 4.5. Depiction of Cross-Flow Bundle Design.**

$$\frac{dP}{dx} = -\frac{\zeta}{S_L}\frac{\rho U^2}{2} - \rho\frac{d}{dx}\left(\frac{1}{2}U^2\right) \qquad (4.44)$$

Consistent with the parallel channel flow case, Eqs. 4.1-4.2 can be used to eliminate local gas density and flow velocity from this equation in terms of gas temperature. Carrying out these steps yields,

$$\frac{dP}{dx} = -\left(1 - \frac{\omega^2 T}{R_g P^2}\right)^{-1}\left\{\frac{\omega^2}{R_g P}\frac{dT}{dx} + \frac{\zeta}{S_L}\frac{\omega^2}{2R_g}\frac{T}{P}\right\}, \qquad (4.45)$$

This expression is noted to be identical to Eq. 4.17, with the exception that the term $f/D_h$ in that equation is replaced by $\zeta/S_L$ for the case of cross-flow.

With this result, effort is now directed towards modification of the gas conservation of energy equation (i.e., Eq. 4.15) for the case of cross-flow. Note that the total cladding heat transfer surface area in the vertical unit cell depicted in Figure 4.5 is given by:

$$A_T = 2\pi R_c B_L \frac{L_f}{S_L} \tag{4.46}$$

Thus, the axially smeared differential heat transfer surface area is found as:

$$dA = 2\pi R_c B_L \frac{B_L}{S_L} dx \tag{4.47}$$

Thus, the analog to Eq. 4.14 governing the heat transfer into the control volume for the case of cross-flow is of the form:

$$\dot{Q} = 2\pi R_c h_{con} \frac{B_L}{S_L} (T_s - T) dx, \tag{4.48}$$

Correlations for the convective heat transfer coefficient in cross-flow, $h_{con}$, are provided in the next subsection. Substitution of Eq. 4.48 into Eq. 4.13 and using Eqs. 4.1 and 4.2 to eliminate gas density and velocity in terms of temperature and pressure yields:

$$\frac{dT}{dx} = \left(1 + \frac{\omega^2 T}{c_p P^2}\right)^{-1} \left\{\xi(T_s - T) + \frac{\omega^2 T^2}{c_p P^3} \frac{dP}{dx}\right\}, \tag{4.49}$$

This expression is identical to Eq. 4.18 with the exception that the parameter $\xi$ is redefined as:

$$\xi = \frac{2\pi R_c h_{con}}{c_p \dot{m}} \left(\frac{B_L}{S_L}\right) \tag{4.50}$$

Equations 4.45 and 4.50 constitute the required modifications to the coolant conservation of momentum and energy equations for the case of bundle cross-flow. Pressure losses at the core inlet and exit are calculated using the same approach as for the parallel channel flow case (i.e., see Eq. 4.9 and the discussion thereafter). Grid spacers are not considered for the cross flow case due to the short length of the cladding segments in this design.

The solutions for the fuel and cladding temperatures that are calculated as part of the solution remain the same as for the parallel channel flow case (i.e., Eqs. 4.27 through 4.30), with the exception that the convective heat transfer coefficient is calculated using correlations that are applicable to the cross-flow case (see next section). The appropriate area mapping factors for the case of cross-flow are included in Eqs. 4.48 and 4.50 so that energy is conserved.

### 4.2.2 Ancillary Correlations for Horizontal Pin Bundle Case

In order to proceed with the analysis, correlations are required for the hydraulic drag coefficient, $\zeta$, and the convective heat transfer coefficient in cross-flow, $h_{con}$. Note that both of these variables can be functions of the number or pin rows for shallow tube banks (i.e., $n \leq 16$). However, for the cases considered herein, the number of pin rows exceeds this limit by a large margin, and therefore entrance effects are neglected.

For the case of in-line tube bundles, the hydraulic drag coefficient depends on the Reynolds number, Eq. 4.32, as well as the dimensionless tube transverse and longitudinal pitches, $\hat{S}_T$, and $\hat{S}_L$, respectively. The following correlation that is utilized in this study is given by Idelchik [4.6].

For the case $\hat{S}_T \leq \hat{S}_L$:

$$\zeta = 2.0\left(\hat{S}_T - 1\right)^{-0.5} \mathrm{Re}^{-0.2} \tag{4.51}$$

For the case $\hat{S}_T > \hat{S}_L$:

$$\zeta = \begin{cases} 0.38\left(\dfrac{\hat{S}_T - 1}{\hat{S}_L - 1} - 0.94\right)^{-0.59} \left(\hat{S}_T - 1\right)^{-0.5} \mathrm{Re}^{\overline{\left[\frac{\hat{S}_T - 1}{\hat{S}_L - 1}\right]^2}^{-0.2}}; & 1 \leq \dfrac{\hat{S}_T - 1}{\hat{S}_L - 1} \leq 8 \\ 0.118\left(\hat{S}_T - 1\right)^{-0.5}; & \dfrac{\hat{S}_T - 1}{\hat{S}_L - 1} \geq 8 \end{cases} \tag{4.52}$$

Note that Reynolds number in these correlations is based on the cladding outer diameter, $D_c$, and the flow velocity based on the minimum flow area in the tube bundle, U.

A plot of the Euler number as a function of transverse pitch ratio, $\hat{S}_T$, is provided in Figure 4.6 for several different Reynolds numbers that span the range of those calculated for GFR full power operating conditions. A similar plot in which the tube longitudinal pitch is treated as the independent variable is shown in provided in Figure 4.7. As is evident, the Euler number is a complicated function of pitch ratio, particularly in the region where $\hat{S}_T \sim \hat{S}_L$. In this region, vortex shedding and the resultant pin-to-pin flow field interactions cause the complicated non-linear dependences that are observed in Figures 4.6 and 4.7.

The Nusselt number correlation that is used to evaluate the convective heat transfer coefficient in cross-flow is due to Žukauskas [4.7]. The correlation is of the form:

$$Nu = \frac{h_{con} D_c}{k} = C_1 Re^{C_2} Pr^{C_3} \quad (4.53)$$

where the constants $C_1$, $C_2$, and $C_3$ are Reynolds number dependent. The values of these constants are provided in Table 4.4. The values of the dimensionless numbers in this correlation are also based on cladding diameter and maximum flow velocity in the bundle.

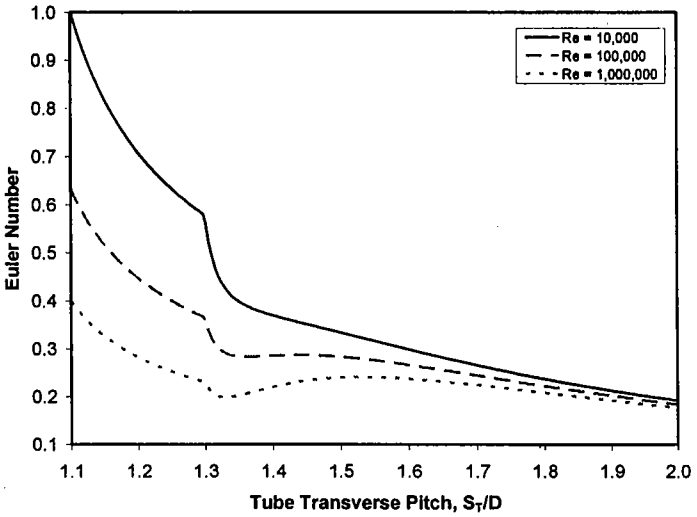


**Figure 4.6. Euler No. vs. Transverse Pitch for $S_L/D_c = 1.3$.**

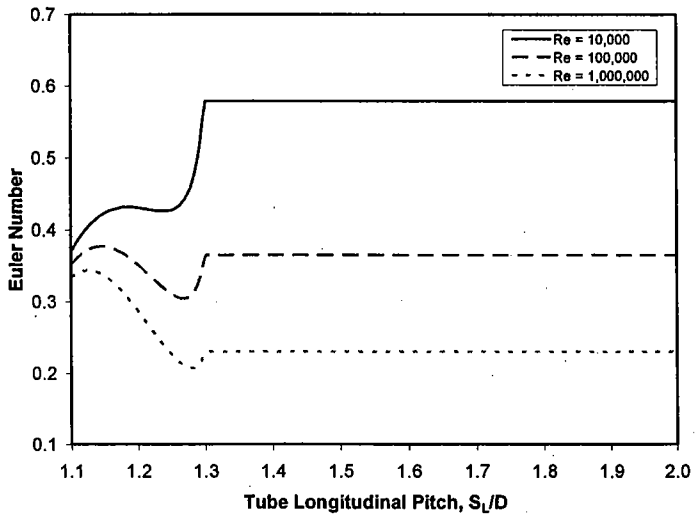


**Figure 4.7. Euler No. vs. Longitudinal Pitch for $S_T/D_c = 1.3$.**

**Table 4.4. Žukauskas [4.7] Correlation Constants.**

| Reynolds No. Range | $C_1$ | $C_2$ | $C_3$ |
|---|---|---|---|
| 1-100 | 0.9 | 0.4 | 0.36 |
| 100-1000 | 0.52 | 0.5 | 0.36 |
| $1000\text{-}2\cdot10^5$ | 0.27 | 0.63 | 0.36 |
| $2\cdot10^5\text{-}2\cdot10^6$ | 0.033 | 0.8 | 0.4 |

### 4.2.3 Bundle Design

Before proceeding with the analysis, a physical layout for the cross-flow bundle needs to be defined. Since the neutronics behavior is closely linked to the core smeared fuel density, the first criterion for the base case bundle design is that the smeared fuel density shall be the same as for the vertical core case. Second, the same fuel and cladding radial dimensions will be utilized (see Table 4.1). Third, the transverse tube pitch will be taken equal to the pin pitch in the vertical core design, which is 12.6 mm. As noted earlier, an inline pin layout is adopted for this study since this design would probably be the easiest for the incorporation of vertically inserted reactivity control blades. With these specifications, the last remaining variable for the cross-flow pin bundle layout is the longitudinal tube pitch. With the above criteria, a straightforward calculation indicates that the longitudinal pitch must be equal to 10.88 mm to conserve the smeared fuel density. With the same fuel density, the overall core active fuel length

must be maintained at 1.344 m to preserve the core outlet temperature, and therefore the 2400 MWt overall core power rating for the current GFR design (see Table 4.1). Given the longitudinal pitch, the number of vertical rows of fuel pins is thus evaluated as 123.56, which is rounded down to 123. Finally, the core bundle is assumed to be square, and the internal bundle dimension is set at $B_W = B_L = 188.45$ mm to conserve the bundle cross-sectional areas between the vertical [4.5] and cross-flow bundle designs. This pin length is well within the range where high-strength SiC tubing segments can be manufactured. With this dimension, each cross-flow bundle would have 15 transverse rows of fuel pins.

Finally, the vertical bundle design featured core reflectors and fission gas plena that were integral components of the overall pin design. For the cross-flow case it is clear that a vented pin design would need to be developed. However, the presence of the plena is neglected in this analysis, and the fuel is assumed to completely occupy the pin length inside the bundle shroud. In terms of axial reflectors, one approach would be to simply include reflector rods in an identical cross-flow configuration above and below the active fuel length. However, this approach is avoided since this type of geometry has an inherently high pressure drop relative to a parallel flow, open channel design. Thus, in the analysis that follows, any pressure drops across the upper and lower core reflectors are neglected on the basis that these losses would be small compared to that across the bundle itself.

The overall cross-flow bundle baseline design data are summarized in Table 4.5. The balance of the information required to carry out the analysis (i.e., thermophysical property data and core inlet plenum operating conditions) are the same as that shown in Table 4.1.

**Table 4.5. Baseline Horizontal Bundle Design Data.**

| Parameter | Value |
|---|---|
| Fuel pellet ID | 3.00 mm |
| Fuel pellet OD | 7.37 mm |
| Average fuel power density | 451 MW/m$^3$ |
| Axial power peaking factor | 1.21 |
| Gap width | 0.10 mm |
| Clad thickness | 1.00 mm |
| Clad OD | 9.57 mm |
| Pin transverse pitch | 12.56 mm |
| Pin longitudinal pitch | 10.88 mm |
| Pin length | 188.45 mm |
| Active fuel bundle length | 1.344 m |
| Fuel can Shape | Square |
| Fuel can internal dimensions | 188.45 x 188.45 mm |
| Number of Horizontal pin rows | 15 |
| Number of vertical pin rows | 123 |

### 4.2.4 Results and Discussion

Key results (i.e., flow velocity, temperatures, and pressure) for the baseline cross-flow bundle design are compared with the vertical bundle results in Figure 4.8 for the case of an axial power peaking factor of 1.21. In addition, an ancillary plot of the flow channel convective heat transfer coefficients for the two cases is provided in Figure 4.9.

As is evident from Figure 4.8(b), the calculated peak fuel and cladding temperatures for the cross-flow design are 1358 and 1175 K, respectively. These temperatures are on average ~ 100 K less than the peak fuel and cladding temperatures calculated for the vertical flow case (see Table 4.3). Examination of Figure 4.9 indicates that this temperature reduction is due to the much (i.e., ~ 200 %) higher convective heat transfer coefficient that is calculated for the cross-flow case. However, examination of Figure 4.8(c) indicates that the temperature reduction comes at a very high cost in terms of core pressure drop. In particular, the pressure drop over the 1.34 m long fuel length is calculated to be 730 kPa at full power conditions, which is over an order of magnitude higher than the ~ 55 kPa pressure drop that is calculated for the vertical fuel bundle design (see Table 4.3).

In summary, these calculations show that although acceptable fuel and cladding temperatures

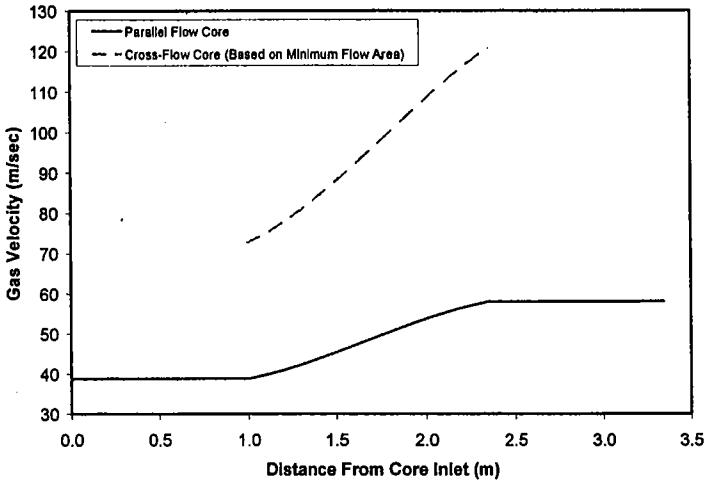


(a)

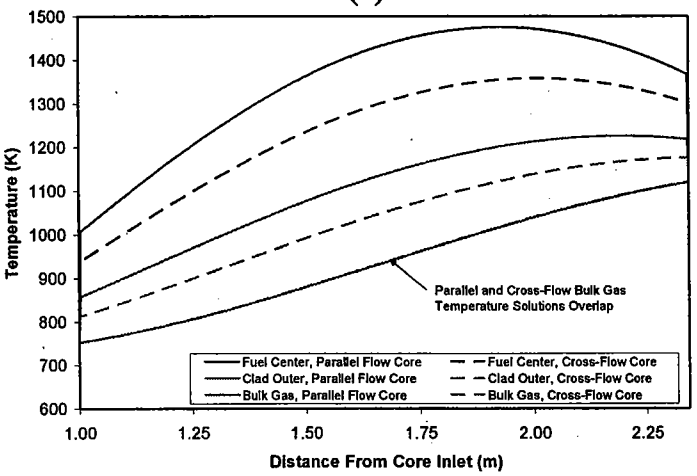


(b)

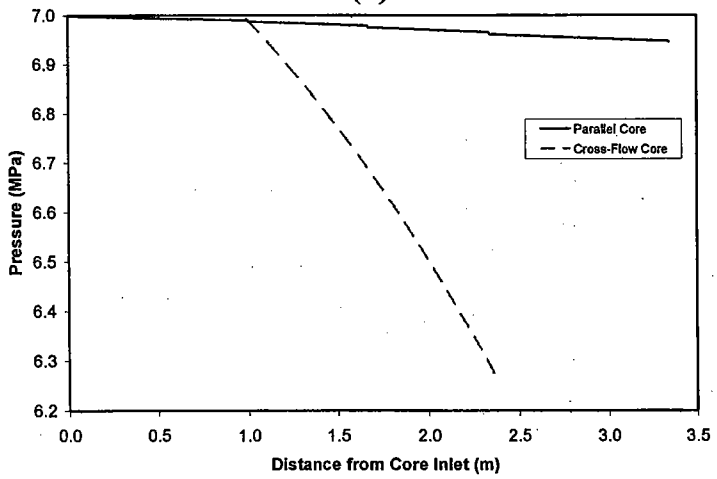


(c)

**Figure 4.8. Base Case Cross-Flow Bundle Results Compared to Vertical Design: a) Velocities, b) Temperatures, and c) Pressures.**

can be achieved under normal operating conditions for the baseline cross-flow bundle design, the overall core pressure drop exceeds that which will allow acceptable core cooling under natural convection flow conditions to develop under postulated accident conditions. On this basis, a set of parametric calculations are performed below to determine if a suitable pin layout can be identified that would reduce the pressure drop to an acceptable level (viz., ~ 50 kPa).

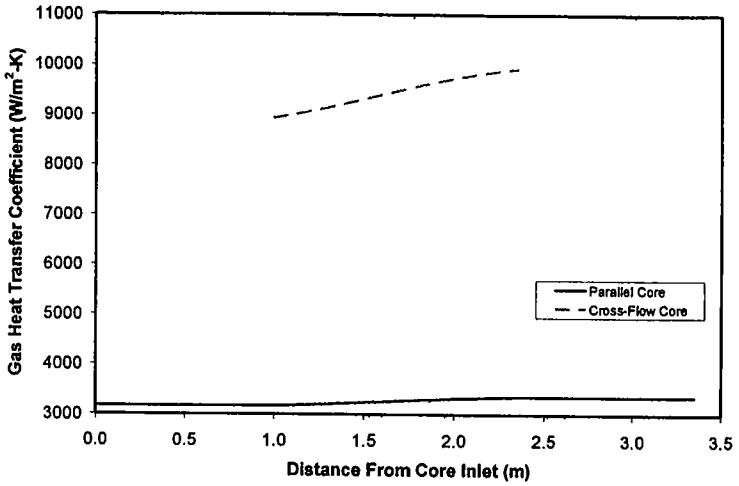


**Figure 4.9. Convective Heat Transfer in Cross-Flow Compared to Parallel Flow Case.**

In the first case, dimensionless tube longitudinal pitch, $\hat{S}_L$, is varied to investigate the effect of this parameter on core pressure drop. In these calculations, the number of vertical pin rows is held constant, and therefore the overall core height increases in direct proportion to the longitudinal pitch. However, the core diameter would remain the same using this approach. The fuel fission power density is also kept constant at the value for the baseline case (see Table 4.1). As a result, the core exit temperature is fixed at the GFR design specification of 1123 K (850 °C) as the pitch is varied. All other parameters (i.e., pin diameter and transverse pitch) are held constant at the baseline values.

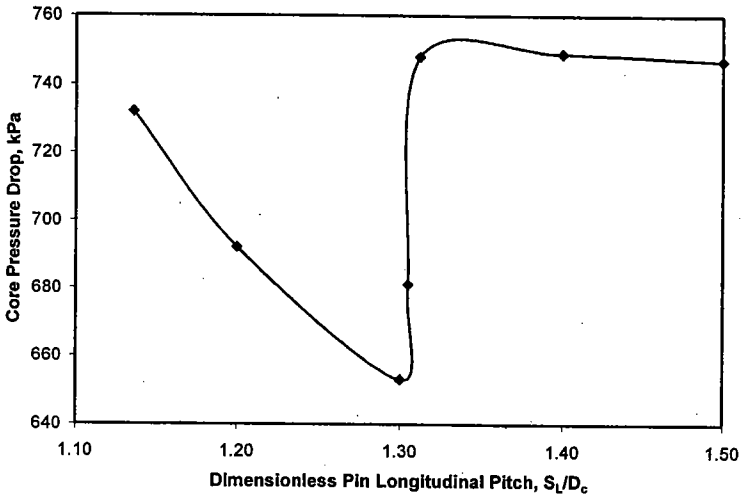


**Figure 4.10. Cross-Flow Core ΔP vs. Pin Longitudinal Pitch.**

The results for this case are shown in Figure 4.10. As is evident, the core pressure drop systematically decreases as the pitch is increased from the baseline of $\hat{S}_L = 1.136$ until the longitudinal pitch matches the transverse pitch baseline of $\hat{S}_T = 1.312$. After this point, the pressure drop increases rapidly to ~ 750 kPa, which exceeds the pressure drop for the baseline bundle design. The explanation for this rather odd pressure dependence becomes evident upon examination of Figure 4.7. In particular, the calculated pressure drop is simply following the trend predicted by the hydraulic drag coefficient correlation

(Idelchik [4.6]). As noted earlier, when $\hat{S}_T \sim \hat{S}_L$, there are pin-to-pin flow-field interactions that cause the complicated non-linear dependences that are observed in Figures 4.6 and 4.7. In any event, this analysis indicates that the maximum reduction in core $\Delta P$ occurs when the longitudinal pitch is increased to $\hat{S}_L \sim 1.3$ when $\hat{S}_T = 1.312$. Under these conditions, core $\Delta P$ is reduced from 730 to 650 kPa, which is far less than the required reduction to achieve the target pressure drop of 50 kPa.

Note that the peak fuel and cladding temperatures calculated over the range of conditions for this case are the same as the baseline results. This is due to the fact that the Reynolds number is principally determined by the pin transverse pitch and diameter, both of which were held constant for this case. The convective heat transfer coefficient, evaluated through Eq. 4.53, is only a function of these two variables for a given set of coolant properties.

In the second case, the dimensionless transverse tube pitch, $\hat{S}_T$, is varied to investigate the effect of this parameter on core pressure drop. For these calculations, the pin lattice is expanded horizontally in direct proportion to the transverse pitch while the longitudinal pitch and number of fuel pin rows is held constant. Therefore, the core diameter increases in direct proportion to transverse pitch, while the core height remains fixed. The bundle shroud dimensions, $B_W$ and $B_L$, are also increased linearly with pitch. Thus, coolant mass flowrate through the bundle is also increased in direct proportion to the transverse pitch. Finally, the fuel fission power density is held constant at the value for the baseline case. Using this approach, the core exit temperature is maintained at the 1123 K target as the pitch is varied.

The results for this second case are shown in Figure 4.11. As is evident, core $\Delta P$ systematically decreases as the transverse pitch increases. However, even when the pitch has been increase to the point where $\hat{S}_T = 1.50$, the core $\Delta P$ is still 210 kPa, which is four times the target limit. However, this pressure drop reduction comes with a high price: the core cross sectional area would be increased by 125% using this type of approach.

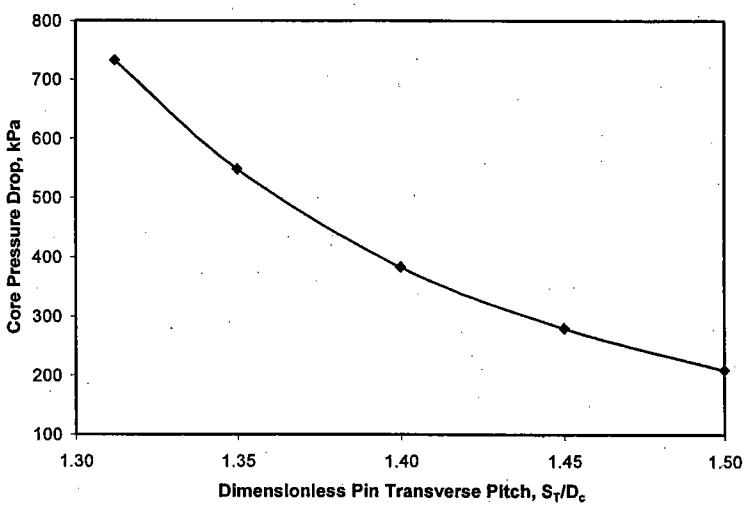

**Figure 4.11. Cross-Flow Core $\Delta P$ vs. Pin Transverse Pitch.**

Peak fuel and cladding temperatures were calculated to increase by 11 and 19 K, respectively, relative to the baseline case over the range of conditions shown in

Figure 4.11. This trend is due to the fact that the coolant flow velocity and therefore Reynolds number are inversely proportional to transverse pitch for this case. Thus, the convective heat transfer coefficient evaluated through Eq. 4.53 is reduced as pitch increases, which causes the modest increase in the peak fuel and cladding temperatures.

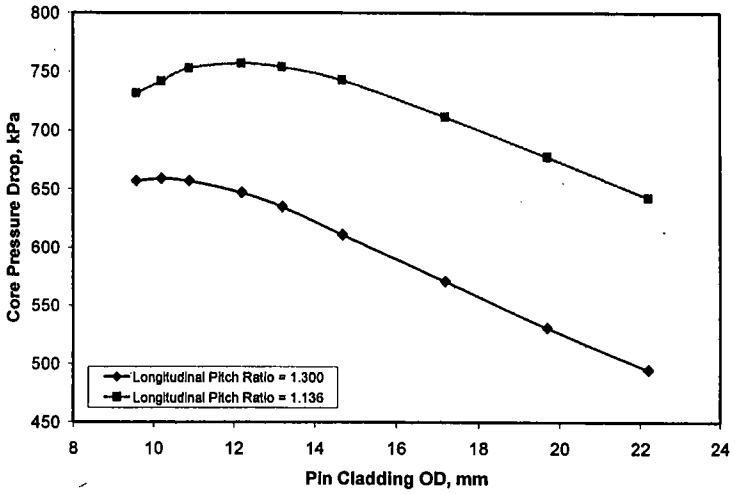


**Figure 4.12. Core ΔP vs. $D_c$ for the Case $\hat{S}_T = 1.312$.**

In the third and final case, both the *dimensionless* transverse and longitudinal pin pitches are held constant, and the pin diameter is varied to investigate the effect of this parameter on core pressure drop. On this basis, both horizontal and vertical pin pitches are increased in direct proportion to the cladding diameter, while the overall core volume is held constant. Thus, the number of both horizontal and vertical pin rows in the core layout is reduced as the pin diameter increases. The smeared fuel density is fixed by virtue of the fact that the lattice P/D ratios are fixed. Overall coolant mass flowrate is held constant, and since the power density is the same, the core exit temperature is maintained at 1123 K as the diameter is varied.

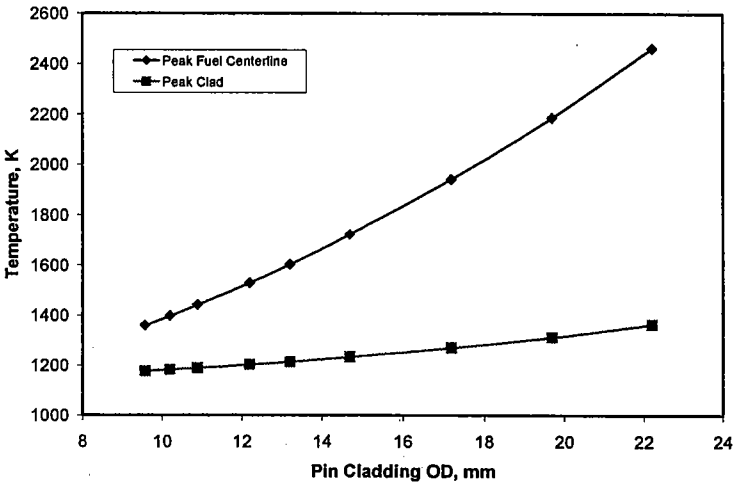


**Figure 4.13. Peak Fuel and Cladding Temperatures vs. $D_c$ for the Case $\hat{S}_T = 1.312$ and $\hat{S}_L = 1.136$.**

The core pressure drop results are shown in Figure 4.12 for the case in which $\hat{S}_T$ and $\hat{S}_L$ are fixed at the baseline values, and also for the case in which $\hat{S}_L$ is increased to 1.30. Recall that this latter case was found to minimize core ΔP when $\hat{S}_T$ is set at the baseline value of 1.312. Overall, core ΔP decreases as the $D_c$ increases. This is due in part to the fact that the Reynolds number increases with increasing $D_c$, which causes the Euler number to decrease (see Figures 4.6 and 4.7). This trend is also due to the fact that the number of pin rows in cross-flow decreases as $D_c$ increases, which causes a corresponding reduction in pressure drop (see Eq. 4.41). As is evident from Figure 4.12,

core ΔP may be reduced to as low as 450 kPa if the pin diameter is increased to 22 mm. This pressure drop is again noted to be significantly above the target of 50 kPa. However, this pressure drop reduction also comes with a price. As shown in Figure 4.13, fuel centerline temperatures would exceed 2400 K if the pin diameter was increased to this level. This increase is simply due to the conduction limitation that controls the fuel temperature response; see Eqs. 4.27-4.29 (i.e., temperature increase at the fuel center scales with the pellet radius squared).

In summary, this analysis has shown that overall core pressure drops for the case of horizontal core bundle design exceed that which will allow acceptable core cooling under natural convection flow conditions under postulated accident conditions. On this basis, the vertical pin bundle is further analyzed to verify that the design is acceptable from the viewpoint of flow-induced vibration. This analysis is provided in the next section.

## 4.3 Vertical Pin Bundle Vibration Analysis

The previous sections have investigated the thermalhydraulic performance of both vertical and horizontal pin bundle designs. The results indicate that a vertical bundle design must be adopted in order to maintain the core pressure drop in the range that will allow adequate cooling under natural convection flow conditions for postulated accident sequences. On this basis, the objective of this section is to further examine the vertical bundle design to verify acceptable performance from the viewpoint of flow-induced vibration.

There are two primary concerns from the viewpoint of vibration analysis: i) the magnitude of turbulence-induced pin displacements; i.e., preclude pin-to-pin contacts which could result in damage accumulation over the course of plant operations, and ii) excitation mechanisms, wherein the frequency of flow field oscillations may match the natural vibration frequency of the pins, resulting in energy extraction from the flow field that can lead to pin damage. These two concerns are addressed in sequence below for the current GFR vertical pin bundle design.

Turbulence-induced vibration displacement for the case of parallel flow has been studied by a variety of investigators. Paidoussis [4.8] experimentally measured vibration amplitude for end-supported cylinders over a range of flowrates. He found that the displacement data could be correlated as:

$$\frac{\Delta}{D_c} = 5.0 \cdot 10^{-4} \frac{K_p}{\alpha_L^4} \left( \frac{\hat{U}^{1.6} \varepsilon^{1.8} Re^{0.25}}{1+\hat{U}^2} \right) \left( \frac{D_h}{D_c} \right)^{0.4} \frac{\beta^{2/3}}{1+4\beta} \tag{4.54}$$

where:

| | | |
|---|---|---|
| $\Delta$ | = | tube displacement, |
| $K_p$ | = | flow constant (1 for quiet flow, or 5 for realistic disturbances), |
| $\alpha_L$ | = | first mode beam eigenvalue (3.412 for simply supported, or 4.73 for fixed ends), |

$\hat{U}$ = dimensionless velocity = $UL\sqrt{\frac{m_v}{EI}}$

E = cladding modulus of elasticity,

L = pin length (between supports),

I = cladding area moment of inertia = $\frac{\pi}{64}\left(D_c^4 - D_f^4\right)$

$m_v$ = fluid added mass external to cladding = $C_M \rho\left(\frac{\pi}{4}D_c^2\right)$,

$C_M$ = added mass coefficient [1] = $e^{\left(1.434-5.654x+8.625x^2-4.583x^3\right)}$,

x = $\frac{P_p - D_c}{D_c}$,

$P_p$ = pin pitch,

ε = $\frac{L}{D_c}$,

β = $\frac{m_v}{m_p + m_v}$,

$m_p$ = pin mass per unit length = $\frac{\pi}{4}\left[\rho_i D_f^2 + \rho_c\left(D_c^4 - D_f^4\right)\right]$,

$\rho_c$ = cladding density,

and $\rho_i$ is the density of the medium on the interior of the cladding depending upon axial position (i.e., fuel, reflector, or helium density if in the active core, reflector, or fission gas plenum regions, respectively).

Aside from the work of Paidoussis, Blevins [4.10] modified the theoretical model of Chen and Wambsganss to arrive at the following correlation for the root-mean-square displacement of a cylinder subject to a turbulent flow field:

$$\frac{\Delta}{D_c} = 0.036 K_B \sqrt{U D_c^2}\left(\frac{\rho D_c^2}{m_p + m_v}\right)\left(\frac{U}{f_n D_c}\right)^{1.5}\left(\frac{D_h}{D_c}\right)^{1.5}\left(\frac{D_c}{L}\right)^{0.5}\left(\frac{1}{\varsigma}\right)^{0.5} \tag{4.55}$$

where $K_B$ is a dimensional constant ($5.8 \cdot 10^{-3}$ $sec^{1/2}/m^{3/2}$), ς is a viscous damping factor, and $f_n$ is the pin natural vibration frequency which is defined as:

$$f_n = \frac{\alpha_L^2}{2\pi L^2}\sqrt{\frac{EI}{m_p + m_v}} \tag{4.56}$$

As discussed by Shin and Wambsganss [4.9], the damping factor ς is a function of the mean coolant velocity. These data may be correlated as:

[1] Based on a curve fit to the data provided in the review paper by Shin and Wambsganss [4.9].

$$\varsigma = \begin{cases} 0.027 + 1.73 \cdot 10^{-3}(U - 16.7); & U > 16.7 \text{ m/sec} \\ 0.003 + 8.01 \cdot 10^{-4} U + 3.70 \cdot 10^{-5} U^2; & U \le 16.7 \text{ m/sec} \end{cases} \quad (4.57)$$

The fuel pin displacements calculated on the basis of Eqs. 4.54 and 4.55 are plotted in Figure 4.14 as a function of the number of (equally spaced) grid spacers positioned along the length of the bundle. For these calculations, the pins are assumed to be simply supported at the core inlet and exits, and also at the grid spacer locations. The SiC cladding elastic modulus, E, was set at 430 GPa. The displacement calculations are based on the mean coolant velocity and gas density which are calculated over each pin segment. The pin mass per unit length, $m_p$, is also calculated for each rod segment along the channel. For the case of two or more grid spacers, the maximum displacements are thus calculated at the core exit between the last grid spacer and pin support plate since flow velocity is highest, and $m_p$ the lowest (due to pin fission gas plenum), at this location. Maximum displacement decreases rapidly with the number of grid spacers since the length between supports, L, decreases as the number of grid spacers increases. The information in Figure 4.14 indicates that the vertical bundle design is acceptable in terms of preventing pin-to-pin contact from turbulence-induced vibration regardless of the number of grid spacers included in the bundle design.

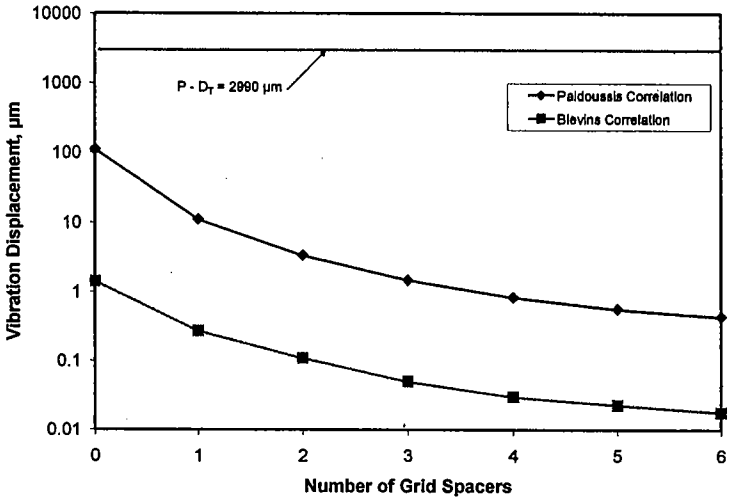


**Figure 4.14. Turbulence-Induced Pin Displacements vs. Number of Grid Spacers for Parallel Flow.**

With the magnitude of turbulence-induced pin displacements assessed, effort is now directed towards evaluating the potential for pin vibrational coupling with the surrounding flowfield. As discussed by Melese and Katz [4.10], these types of instabilities are principally observed in situations involving cross-flow across tube banks. Although the bundle under consideration is designed for parallel channel flow, cross-flow velocity components may also develop, particularly near the bundle inlet and exits, as well as near the grid spacers. Estimation of the magnitude of the cross-flow velocities in this situation is not straightforward. Tinker [4.11] has suggested that average cross-flow velocity on the shell-side of heat exchangers can be computed as the bundle volumetric flowrate divided by the average cross-flow area, so that:

$$U_c = \frac{\dot{m}_b}{\rho A_c} \quad (4.58)$$

where $\dot{m}_b$ is the total bundle mass flowrate and $A_c$ is the average crossflow area. The average cross-flow area at the centerline of a cylindrical bundle with pins on a triangular pitch is given as [4.11]:

$$A_c = 0.98\left(\frac{P_p - D_c}{D_c}\right)D_B L \tag{4.59}$$

where $D_B$ is the outer diameter of the bundle (assumed to equal the hexcan internal flat-to-flat dimension of ~ 20 cm), and (in heat exchanger applications) L is tube span between support plates. In this application, L is set equal to the pin span between grid spacers. In heat exchanger applications, the tube support plates are used to induce cross-flow within the bundle (thereby increasing the convective heat transfer), and therefore this is a logical length scale upon which to base the cross-flow velocity. However, in this application, the flow will not be completely redirected into a cross-flow pattern at the grid spacer locations, but rather, local turbulence will be generated with a cross-flow component. Thus, it is highly conservative to use Eqs. 4.58 and 4.59 to estimate cross-flow velocities in the GFR vertical bundle design, and the actual velocities are expected to be much less than that predicted using this approach.

In terms of cross-flow instabilities, when a tube bank is subject to a high velocity cross-flow, then the fluid is accelerated into the gaps between tubes, which cause local pressure forces to develop on the tube surfaces. If the tubes flex, then this will change the local flow velocity and hence the pressure force applied to the tubes. If the tubes move in tandem, then there is the potential to extract energy from the flow, and if this energy is greater than the damping energy as the tubes move, then instability can develop. The minimum flow velocity for the onset of this whirling instability is given through the expression [4.12]:

$$\frac{U_w}{f_n D_c} = K_w\sqrt{2\pi\varsigma\left(\frac{m_T}{\rho D_c^2}\right)} \tag{4.60}$$

Where $U_w$ is the minimum coolant flow velocity for onset of this whirling instability, and $K_w$ is a dimensionless instability constant (~ 3). In this case, the viscous damping constant $\varsigma$ is evaluated through Eq. 4.57, but the velocity is evaluated with $U_c$ as opposed to the vertical channel flow velocity, U.

The minimum velocity for onset of swirling instability, evaluated from Eq. 4.60, is plotted in Figure 4.15 as a function of the number of grid spacers. Also shown in this graph is the bundle cross-flow velocity estimated through Eqs. 4.58 and 4.59. Both $U_w$ and $U_c$ are noted to increase with the number of grid spacers. The rise in $U_w$ is driven by the fact that the pin fundamental frequency increases rapidly with decreasing distance between spacers; see Eq. 4.56. The increase in cross-flow velocity is due to the fact that the (assumed) bundle cross-flow area is directly proportional to the distance between spacers; see Eq 4.59. In any case, the cross flow velocity effectively meets $U_w$ for the case of three spacers, and falls well below $U_w$ for four or more spacers. Hence, this analysis indicates that the use of three grid spacers will more than likely preclude

swirling instabilities in the bundle, given the large conservatism in the estimation of the bundle cross-flow velocity. However, if the decision is made to deploy four spacers to ensure that the cross-flow velocity is well below the instability threshold, then the pressure drop across the bundle would increase slightly from 54.6 kPa (see Table 4.3) to 58.0 kPa; see Figure 4.16.

Aside from whirling instability, a second potentially damaging excitation mechanism can occur when the pin natural vibration frequency approaches the vortex shedding frequency for situations involving high Reynolds number cross-flows. In general, the vortex shedding frequency, $f_v$, is characterized in terms of the dimensionless Strouhal number that is defined as [4.9]:

$$St = \frac{f_v D_c}{U_c} \qquad (4.61)$$

For flows across tube banks, the Strouhal number has been found [4.9] to be a function of the type of tube bank (i.e., in-line vs. staggered), and also the transverse and longitudinal tube-spacing ratios, defined in Eq. 4.40. For this particular application, the tube bank is staggered (i.e. triangular), and the transverse and longitudinal pitches are identical. In order to evaluate the Strouhal number as a general function of pitch-to-diameter ratio, data were extracted from Figure 18

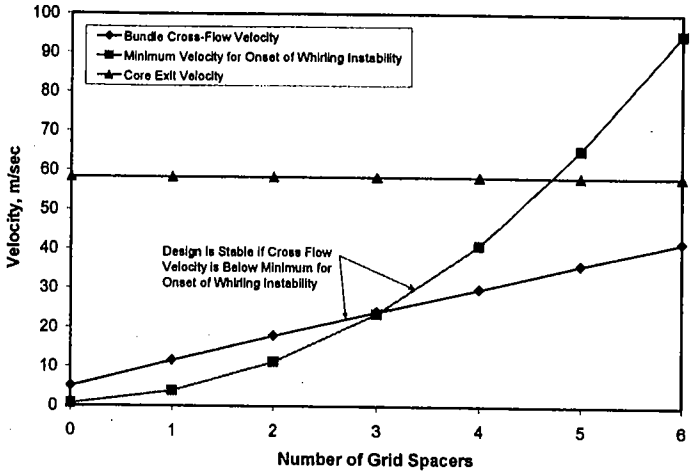


**Figure 4.15. Comparison of Bundle Cross-Flow and Swirling Instability Threshold Velocities.**

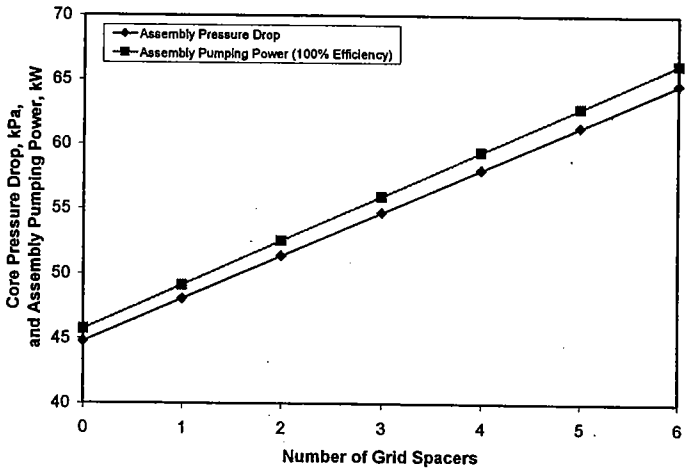


**Figure 4.16. Bundle ΔP and Pumping Power for Reference 271 Vertical Pin Bundle Design.**

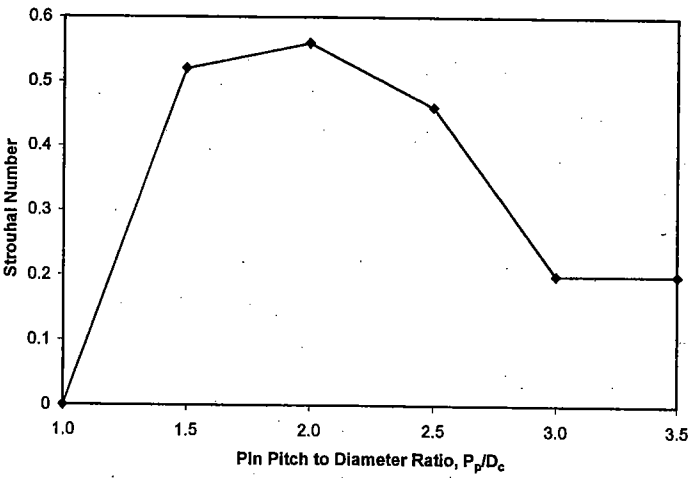


**Figure 4.17. Strouhal Number vs. Pitch-to-Diameter Ratio for a Triangular Pitch Array.**

of Reference [4.9], and this information was used to linearly interpolate in order to estimate St as a function of $P_p/D_c$. This function is shown in Figure 4.17. For the current GFR bundle design, $P_p/D_c \sim 1.3$ (see Table 4.1). Thus, the Strouhal number for the bundle is estimated to be ~ 0.32 based on data provided in Figure 4.17.

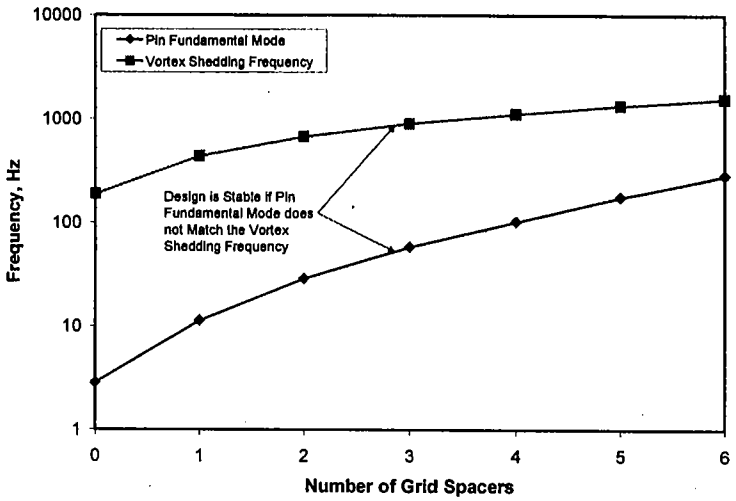


**Figure 4.18. Pin Natural Vibration and Vortex Shedding Frequencies for GFR Vertical Bundle Design.**

The frequency of vortex shedding evaluated from Eq. 4.61 is compared with the pin natural vibration frequency, Eq. 4.56, in Figure 4.18. As is evident, the pin fundamental frequency is at least an order of magnitude below the vortex shedding frequency for any plausible number of grid spacers. Thus, the reference GFR bundle design should not be susceptible to instabilities associated with vortex shedding.

## 4.4 Summary and Conclusions

A general thermal hydraulic channel flow model was developed and applied to the reference GFR vertical bundle design to verify acceptable thermal hydraulic characteristics under full power operating conditions. With these results, modeling modifications were then made to evaluate horizontal bundle design options. The calculations for the horizontal case indicated that although acceptable fuel and cladding temperatures can be achieved under normal operating conditions, the overall core pressure drop exceeds that which would allow acceptable core cooling under natural convection flow conditions to develop under postulated accident conditions.

On this basis, the vertical core bundle was further analyzed to verify acceptable performance from the viewpoint of flow-induced vibration. The results of these analyses indicate that the current 271 pin bundle design with three uniformly spaced grid spacers is acceptable from the viewpoint of turbulence-induced pin displacements. In addition, the design was found to be robust insofar as preventing vibration instabilities that could lead to fretting and wear during normal plant operations.

## 4.5 References


4.1 J. Goodman et al., "The Thermodynamic and Transport Properties of Helium," GA-A13400, October, 1975.

4.2 Appendix A in "Development of Gen IV Advanced Gas-Cooled Reactors with Hardened/Fast Neutron Spectrum," Third Annual Technical Progress Report, I-NERI Project # 2001-002-F, September 2004.

4.3 I. E. Idelchik, Handbook of Hydraulic Resistance, 3rd Ed., CRC Press, 1993.

4.4 K. Rehme, "Pressure Drop Correlations for Fuel Element Spacers," Nuclear Tech., Vol. 139, pp. 72-79, 1973.

4.5 E. Feldman et al., "Generation IV Nuclear Energy Initiative Large GFR Core Subassembly Design," ANL-GENIV-050, August 2005.

4.6 I. E. Idelchik, Handbook of Hydraulic Resistance, 2nd Ed., Hemisphere Publishing, 1986.

4.7 A. A. Žukauskas, "Konvektivnyi Perenos v Teploobmennikakh (Convective Heat Transfer in Heat Exchangers), Nauka, Moscow, p. 472, 1982.

4.8 M. P. Paidoussis, "An Experimental Study of Vibration of Flexible Cylinders Induced by Nominally Axial Flow," Nucl. Sci. Eng., Vol. 35, pp. 127-138, 1969.

4.9 Y. S. Shin and M. W. Wambsganss, "Flow-Induced Vibration in LMFBR Steam Generators: A State-of-the-Art Review," Nucl. Eng. Des., Vol. 40, pp. 235-284, 1977.

4.10 G. Melese and R. Katz, Thermal and Flow Design of Helium-Cooled Reactors, American Nuclear Society, La Grange Park, IL (1984).

4.11 T. Tinker, "Shell-Side Characteristics of Shell-and-Tube Heat Exchangers," Trans. ASME, Vol. 80, pp. 36-52, 1958.

4.12 R. D. Blevins, Flow-Induced Vibration, Van Nostrand Reinhold Co., New York, NY (1977).

# Appendix A – Calculations for Grid Plate

The core weight calculations were based on using the average weight density, per component material multiplied by the corresponding volume for each component. This allows for an effective means to determine the static weight which needs to be supported by the grid plate.

The component weights and average weight densities are summarized in Section 3.3 of the report.

The volumes for the assemblies are calculated from the cross-sectional area times the height of the assembly. The lattice (assembly) pitch distance is used to calculate the cross-sectional area of the hexagonal geometry. The pitch distance is 215 mm (flat-to-flat of the outside duct) plus the inter-assembly gap of 7 mm. The total flat-to-flat distance for the inter-assembly including the gap is 222 mm. The cross-sectional area for a hexagonal area is found in Ref. 3.3 (pg. 1-8) for a six sided polygon:

Area = $3.464 \times r^2$ , where $r$ = radius of inscribed circle

The values of $r$ = 111 mm, which is the assembly pitch of 222 mm / 2 for the current core geometry.

The output from an EXCEL spreadsheet which calculates the weight for each component is given below.

Fuel Assembly

| Fuel Assembly | Radius = 111 (mm)<br>Area = 42679.9 (mm^2) | | | 0.04268 (m^2) | |
|---|---|---|---|---|---|
| Component | Length (m) | Volume (m^3) | Wt. Density (kg/m^3) | Weight (kg) | |
| Fuel | 1.34 | 0.05719 | 3370 | 192.7 | |
| Reflector (lower and upper) | 1 | 0.04268 | 2080 | 88.8 | |
| Plenum (lower and upper) | 1 | 0.04268 | 750 | 32.0 | |
| Shield (lower) | 0.8 | 0.03414 | 2080 | 71.0 | |
| Shield (upper) | 0.7 | 0.02988 | 2080 | 62.1 | |
| Total Weight per Assembly | | | | 446.7 | |
| Total Length per Assembly | 4.84 | | | | |
| Total No. of Assemblies = | 366 | | Total Wt. = | 163484.8 | (kg) |
| | | | Total Wt. = | 163.5 | (mT) |
| | | | Total Wt. = | 180.2 | (tons) |

## Control/Shutdown Assembly

| Control/Shutdown Assembly | Radius = | 111 | (mm) | | |
|---|---|---|---|---|---|
| | Area = | 42679.9 | (mm^2) | 0.04268 | (m^2) |

| Component | Length (m) | Volume (m^3) | Wt. Density (kg/m^3) | Weight (kg) | |
|---|---|---|---|---|---|
| Fuel | 1.34 | 0.05719 | 2940 | 168.1 | |
| Reflector (lower) | 0.5 | 0.02134 | 2120 | 45.2 | |
| Reflector (upper) | 0.5 | 0.02134 | 1820 | 38.8 | |
| Plenum (lower) | 0.5 | 0.02134 | 980 | 20.9 | |
| Plenum (upper) | 0.5 | 0.02134 | 680 | 14.5 | |
| Shield (lower) | 0.8 | 0.03414 | 1470 | 50.2 | |
| Shield (upper) | 0.7 | 0.02988 | 1070 | 32.0 | |
| Total Weight per Assembly | | | | 369.8 | |
| Total Length perf Assembly | 4.84 | | | | |

| Total No. of Assemblies = | 61 | Total Wt. = | 22558.1 | (kg) |
|---|---|---|---|---|
| | | Total Wt. = | 22.6 | (mT) |
| | | Total Wt. = | 24.9 | (tons) |

## Reflector Assembly

| Reflector Assembly | Radius = | 111 | (mm) | | |
|---|---|---|---|---|---|
| | Area = | 42679.9 | (mm^2) | 0.04268 | (m^2) |

| Component | Length (m) | Volume (m^3) | Wt. Density (kg/m^3) | Weight (kg) | |
|---|---|---|---|---|---|
| Reflector | 4.84 | 0.20657 | 4080 | 842.8 | |

| Total No. of Assemblies = | 174 | Total Wt. = | 146648.8 | (kg) |
|---|---|---|---|---|
| | | Total Wt. = | 146.6 | (mT) |
| | | Total Wt. = | 161.7 | (tons) |

Shield Assembly

| Shield Assembly | Radius = | 111 | (mm) | | |
|---|---|---|---|---|---|
| | Area = | 42679.9 | (mm^2) | 0.04268 | (m^2) |

| Component | Length (m) | Volume (m^3) | Wt. Density (kg/m^3) | Weight (kg) | |
|---|---|---|---|---|---|
| Shield and Shield Structure | 4.84 | 0.20657 | 2840 | 586.7 | |
| Total No. of Assemblies = | 318 | | Total Wt. = | 186558.3 | (kg) |
| | | | Total Wt. = | 186.6 | (mT) |
| | | | Total Wt. = | 205.6 | (tons) |

Core Barrel

The core barrel weight was estimated from a preliminary design sketch and was assumed to be 2.54 cm (1.0 in.) thick. This information is from a previous conceptual design of GFR, GFR021 – May, 2004. The height was taken to the length of the fuel assemblies of 4.84 m plus some additional height above the assemblies.

| Core Barrel Weight | | | | | |
|---|---|---|---|---|---|
| | Volume = 2 π R t Ht | | | | |
| | Average Radius R = | 3.3804 | (m) | | |
| | Thickness t = | 0.0254 | (m) | 1 | (in.) |
| Total core barrel height (4.84+1.75+2.988) | Height Ht = | 9.57 | (m) | | |
| | Volume = | 5.16290 | (m^3) | | |
| | Density = | 8000 | (kg/m^3) | | |
| | Total Weight = | 41303.2 | (kg) | | |
| | Total Weight = | 41.3 | (mT) | | |
| | Total Weight = | 45.5 | (tons) | | |

The total weight of all the components is given in Table 3.1 which is 560.6 mT (617.9 tons).

## Case 10a Solid Circular Plate Simply Supported; Uniformly Distributed Pressure from $r_o$ to a

**Solid circular plate**

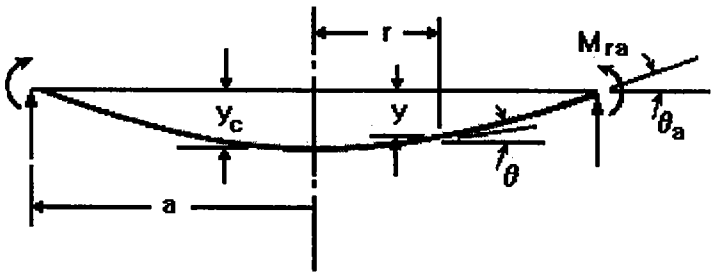


**Uniformly distributed pressure from $r_o$ to a**

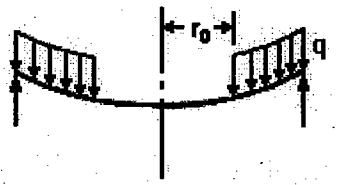

**Enter dimensions, properties and loading**

Plate dimensions:

thickness: $t \equiv 47 \cdot cm$ $t = 18.504 \cdot in$

radius: $a \equiv 145 \cdot in$ $a = 3.683 \cdot m$

Total weight supported by plate (see Table 3.1) $W_{total} := 560.6 \cdot kg \cdot 1000$ $W_{total} = 5.606 \cdot 10^5 \cdot kg$

Compute uniform pressure due to support weight

$$q_{support} := \frac{W_{total} \cdot g}{\pi \cdot a^2} \qquad q_{support} = 18.711 \cdot psi \qquad q_{support} = 1.29 \cdot 10^5 \cdot Pa$$

$g = 9.807 \cdot m \cdot s^{-2}$ acceleration of gravity

Modulus of elasticity: $E \equiv 23 \cdot 10^6 \cdot \frac{lbf}{in^2}$ $E = 1.586 \cdot 10^{11} \cdot Pa$

Poisson's ratio: $\nu \equiv 0.3$

Radial location of applied load: $r_o \equiv 0 \cdot in$

Total Weight on Grid Plate:
(Add weight of plate based on thickness for unit wt. of steel = 8000 kg/m$^3$)

$$W_{plate} := t \cdot 8000 \cdot \frac{kg}{m^3} \cdot \pi \cdot a^2 \qquad W_{plate} = 1.602 \cdot 10^5 \cdot kg \qquad W_{plate} = 176.622 \cdot ton$$

Subtract out holes for assemblies plus add weight of nozzles (see Appendix B for nozzle design)

$$V_{plate} := t \cdot \left(\pi \cdot a^2\right) \qquad V_{plate} = 20.029 \cdot m^3$$

$r_{hole} := 8.6 \cdot cm$ $V_{holes} := t \cdot 919 \cdot \pi \cdot r_{hole}^2$ $V_{holes} = 10.036 \cdot m^3$

$V_{nozzel} := 2.97 \cdot m^3$

$W_{plate1} := 8000 \frac{kg}{m^3} (20.029 - 10.036 + 2.97)\, m^3$ $W_{plate1} = 1.037 \cdot 10^5 \cdot kg$ $W_{plate1} = 114.314 \cdot ton$

Conservatively assume solid plate

$$q_{plate} := \frac{W_{plate} \cdot g}{\pi \cdot a^2} \qquad q_{plate} = 5.348 \cdot psi \qquad q_{plate} = 3.687 \cdot 10^4 \cdot Pa$$

Applied uniform pressure:
(Support weight plus grid plate weight)

$$q \equiv 18.711 \cdot psi + 5.348 \cdot psi \qquad q = 24.059 \cdot psi \qquad q = 1.659 \cdot 10^5 \cdot Pa$$

**Constants**

Shear modulus: $G \equiv \frac{E}{2 \cdot (1 + \nu)}$

D is a plate constant used in determining boundary values; it is also used in the general equations for deflection, slope, moment and shear. $K_{sro}$ is the tangential shear constant used in determining the deflection due to shear.

$$D \equiv \frac{E \cdot t^3}{12 \cdot \left(1 - \nu^2\right)} \qquad D = 1.334 \cdot 10^{10} \cdot lbf \cdot in$$

$$K_{sro} \equiv -0.30 \cdot \left[1 - \left(\frac{r_o}{a}\right)^2 \cdot \left(1 + 2 \cdot \ln\left(\frac{a}{r_o}\right)\right)\right] \qquad K_{sro} = -0.3$$

**Boundary values**

**The $G_n$ and $L_n$ functions used in the equations below are defined at the end of this document.**

$M_r$ is radial moment, Q is shear, y is deflection and $\theta$ is slope.

Due to bending:

At the edge of the plate (a):

$$M_{ra} := 0 \frac{lbf \cdot in}{in} \qquad M_{ra} = 0 \cdot \frac{lbf \cdot in}{in}$$

$$Q_a := \frac{-q}{2 \cdot a} \cdot \left(a^2 - r_o^2\right) \qquad Q_a = -1.744 \cdot 10^3 \cdot \frac{lbf}{in}$$

$$y_a := 0 \cdot in \qquad y_a = 0 \cdot in$$

$$\theta_a := \frac{q}{8 \cdot D \cdot a \cdot (1 + \nu)} \cdot \left(a^2 - r_o^2\right)^2 \qquad \theta_a = 0.03 \cdot deg$$

At the center of the plate (c):

$M_c := q \cdot a^2 \cdot L_{17}$ $\quad M_c = 1.043 \cdot 10^5 \cdot \frac{lbf \cdot in}{in}$

$y_c := \frac{-q \cdot a^4}{2 \cdot D} \cdot \left( \frac{L_{17}}{1+\nu} - 2 \cdot L_{11} \right)$ $\quad y_c = -0.051 \cdot in$

Due to tangential shear stresses:

$y_{sro} := \frac{K_{sro} \cdot q \cdot a^2}{t \cdot G}$ $\quad y_{sro} = -9.2708 \cdot 10^{-4} \cdot in$

**General formulas and graphs for deflection, slope, moment, shear and stress as a function of r**

Define r, the range of the radius:

$r \equiv \frac{a}{100}, \frac{a}{50} .. a$

**Deflection**

$y(r) := y_c + \frac{M_c \cdot r^2}{2 \cdot D \cdot (1+\nu)} + LT_y(r)$

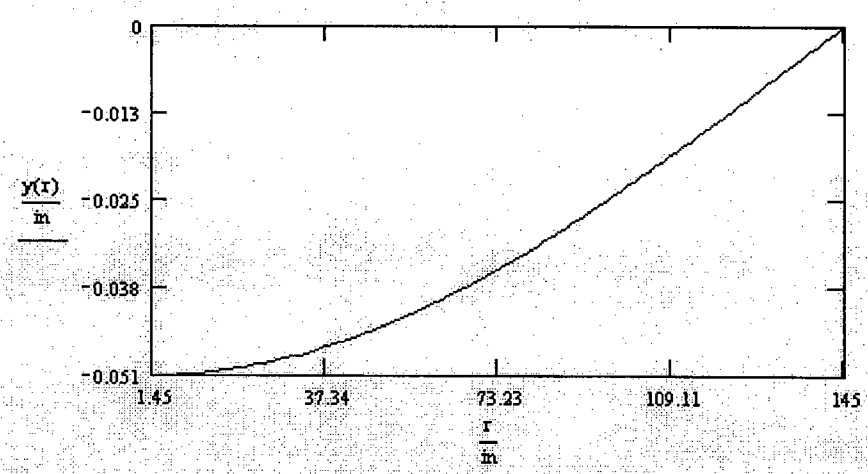


Deflections at the center and outer radius:

$y(0 \cdot in) = -0.051 \cdot in$ $\quad y(a) = 0 \cdot in$

Maximum deflection (magnitude):

$Y_{(r) \cdot \frac{100}{in}} := y(r)$ $\quad A := \max(Y)$ $\quad B := \min(Y)$

$y_{max} := (A > -B) \cdot A + (A \le -B) \cdot B$ $\quad y_{max} = -0.051 \cdot in$

**Large deflection condition check**

Check to verify that the absolute value of the maximum deflection is less than one-half the plate thickness (an assumption stated in the Notation file which must hold true). If $|y_{max}|$ is greater than t/2 (large deflection), the equations in this table used for plates with small deflections are subject to large errors.

$$check := if\left(\left| y_{max} \right| > \frac{t}{2}, 0, 1\right) \qquad check = 1$$

If $|y_{max}|$ is greater than t/2 (i.e., check = 0), only max y and $\sigma$ can be found.

If $|y_{max}|$ is not greater than t/2 (i.e., check = 1), solution okay.

**Slope**

$$\theta(r) := \frac{M_c \cdot r}{D \cdot (1 + \nu)} + LT_\theta(r)$$

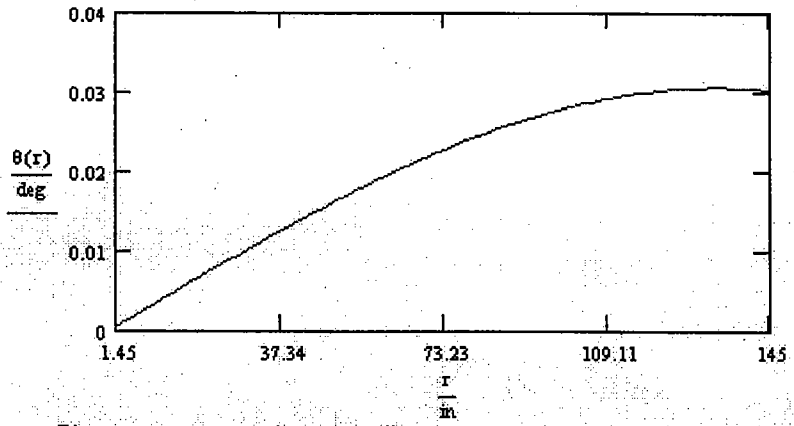


Slope at center and outer radius:

$\theta(0\,in) = 0 \cdot deg$ $\qquad$ $\theta(a) = 0.03 \cdot deg$

Maximum slope (magnitude):

$S_{(r)\cdot\frac{100}{in}} := \theta(r)$ $\qquad$ $A := max(S)$ $\qquad$ $B := min(S)$

$\theta_{max} := (A > -B) \cdot A + (A \le -B) \cdot B$ $\qquad$ $\theta_{max} = 0.031 \cdot deg$

## Moment; radial and tangential

$$M_r(r) := M_c + LT_M(r)$$

$$M_t(r) := \frac{\theta(r) \cdot D \cdot \left(1 - \nu^2\right)}{r} + \nu \cdot M_r(r)$$

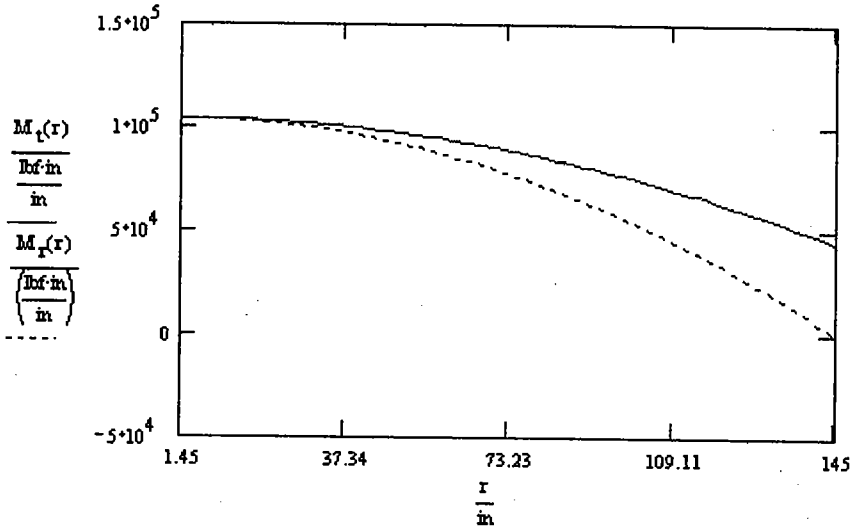


Radial and tangential moment at center and outer radius:

$M_r(0 \cdot in) = 1.043 \cdot 10^5 \cdot \frac{lbf \cdot in}{in}$ $\quad M_r(a) = 0 \cdot \frac{lbf \cdot in}{in}$

$M_t(0.01 \cdot in) = 1.043 \cdot 10^5 \cdot \frac{lbf \cdot in}{in}$ $\quad M_t(a) = 4.426 \cdot 10^4 \cdot \frac{lbf \cdot in}{in}$

Maximum radial and tangential moment (magnitude):

$Mr_{(r)\frac{100}{in}} := M_r(r)$ $\quad Ar := \max(Mr)$ $\quad B := \min(Mr)$

$Mt_{(r)\frac{100}{in}} := M_t(r)$ $\quad At := \max(Mt)$ $\quad Bt := \min(Mt)$

$Mr_{max} := (Ar > -B) \cdot Ar + (Ar \le -B) \cdot B$ $\quad Mr_{max} = 1.043 \cdot 10^5 \cdot \frac{lbf \cdot in}{in}$

$Mt_{max} := (At > -Bt) \cdot At + (At \le -Bt) \cdot Bt$ $\quad Mt_{max} = 1.043 \cdot 10^5 \cdot \frac{lbf \cdot in}{in}$

**Shear** $Q(r) := LT_Q(r)$

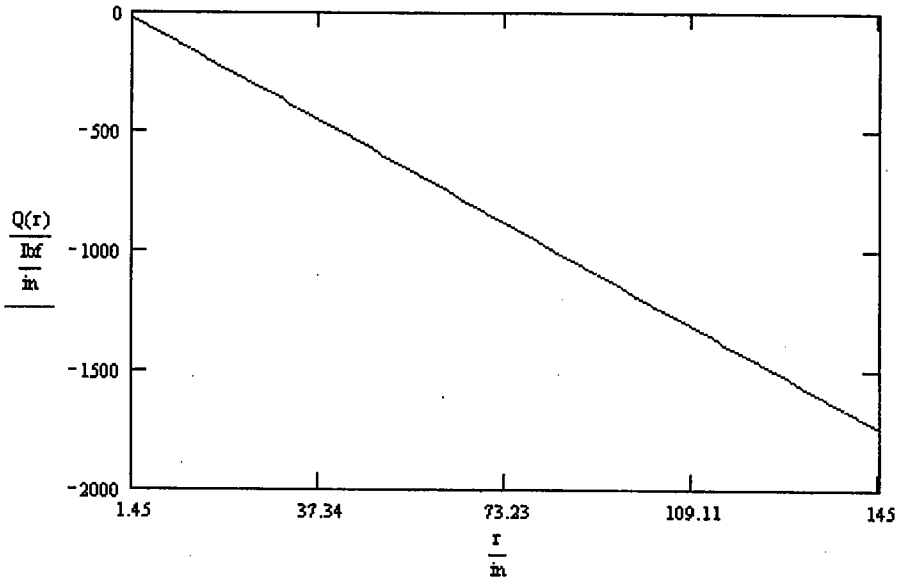


Shear at center and outer radius:

$Q(0.01 \cdot in) = -0.12 \cdot \frac{lbf}{in}$ $Q(a) = -1.744 \cdot 10^3 \cdot \frac{lbf}{in}$

Maximum shear (magnitude):

$V_{(r)\cdot\frac{100}{in}} := Q(r)$ $A := \max(V)$ $B := \min(V)$

$Q_{max} := (A > -B) \cdot A + (A \le -B) \cdot B$ $Q_{max} = -1.744 \cdot 10^3 \cdot \frac{lbf}{in}$

**Bending stresses; radial and tangential**

$$\sigma_r(r) := \frac{6 \cdot M_r(r)}{t^2}$$

$$\sigma_t(r) := \frac{6 \cdot M_t(r)}{t^2}$$

$bistress(r) := \frac{\sigma_r(r)}{\sigma_t(r)}$ Biaxiality Ratio

Calculate Effective Stress

$$\sigma_{eff}(s1, s2, s3) := \left[0.5 \cdot \left[(s1 - s2)^2 + (s2 - s3)^2 + (s3 - s1)^2\right]\right]^{0.5}$$

$$\sigma_e(r) := \sigma_{eff}\left(\sigma_r(r), \sigma_t(r), 0 \cdot psi\right)$$

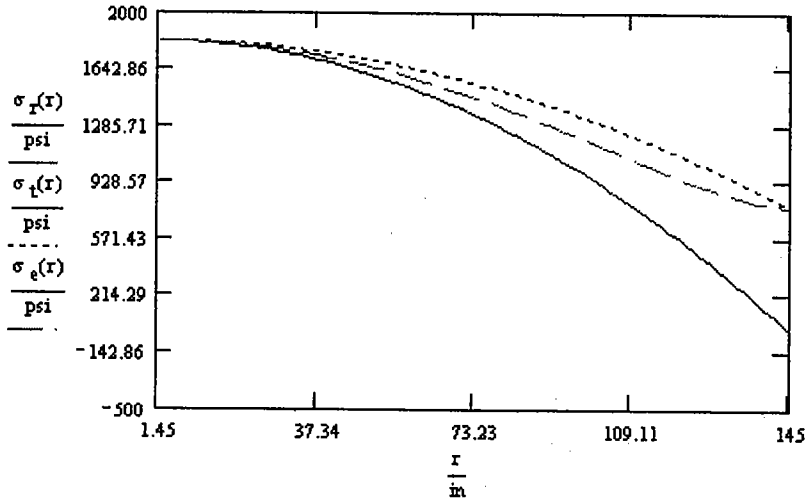


Plot of radial, tangential and effective stress

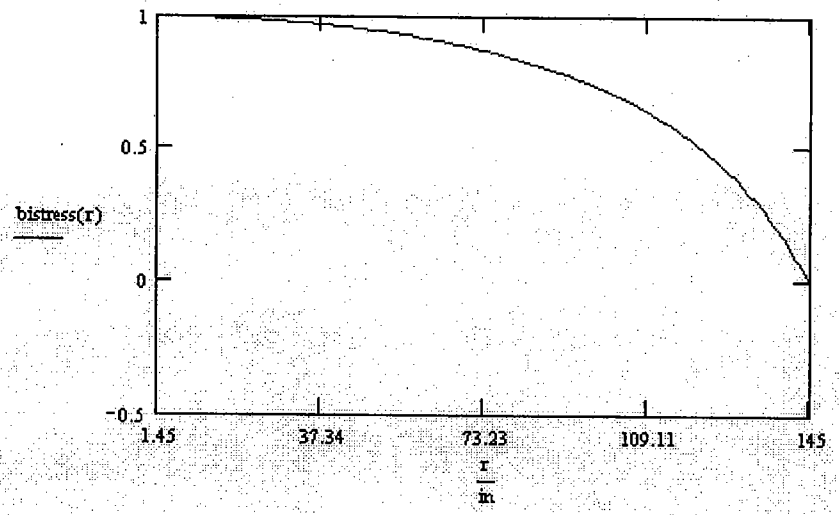


Plot biaxiality ratio

Radial and tangential stress at center and outer radius:

$\sigma_r(0.01\ in) = 1.828 \cdot 10^3\ psi$ $\qquad$ $\sigma_r(a) = 0\ psi$

$\sigma_t(0.01\ in) = 1.828 \cdot 10^3\ psi$ $\qquad$ $\sigma_t(a) = 775.612\ psi$

Maximum radial and tangential stresses:

$\sigma r_{r \cdot \frac{100}{in}} := \sigma_r(r)$ $\quad Ar := \max(\sigma r)$ $\quad Br := \min(\sigma r)$

$\sigma t_{r \cdot \frac{100}{in}} := \sigma_t(r)$ $\quad At := \max(\sigma t)$ $\quad Bt := \min(\sigma t)$

$\sigma r_{max} := (Ar > -Bt) \cdot Ar + (Ar \leq -Bt) \cdot Br$ $\quad \sigma r_{max} = 1.828 \cdot 10^3 \cdot psi$

$\sigma t_{max} := (At > -Bt) \cdot At + (At \leq -Bt) \cdot Bt$ $\quad \sigma t_{max} = 1.828 \cdot 10^3 \cdot psi$

Maximum stresses will be increased by two factors because of the perforated plate:

*First factor* is due to the holes in the plate and is calculated from the *P/h* ratio which taken from Ref. 3.4. *P* is the pitch which is the nominal distance between hole center lines. *h* is the nominal width of the ligament at the minimum cross-section. For the grid plate *h* = *P* - O.D. of nozzle. The outside diameter of the nozzle is defined in Appendix B and was designed to be a 172 mm diameter hole through the grid plate. The pitch *P* is the lattice (assembly) pitch which is 222 mm for the current core design

$P := 222 \cdot mm$ $\quad h := P - 172 \cdot mm$ $\quad h = 50 \cdot mm$

$SM_1 := \frac{P}{h}$ $\quad SM_1 = 4.44$

*Second factor* is the biaxiality ratio, which is taken from Ref. 3.4

Stress Multiplier = 1.15 on bending stress, which is the maximum value for the plate. This is located at the support edge where the biaxiality ratio = 0, thus this is a conservative increase.

$SM_2 := 1.15$

The allowable stress is taken from Ref. 3.2 for 316 SS at temperature of 900F. The allowable stress is multiplied by 1.5 because the stress is due to bending.

$\sigma_{allow} := 15600 \cdot psi \cdot 1.5$ $\quad \sigma_{allow} = 2.34 \cdot 10^4 \cdot psi$ $\quad \sigma_{allow} = 1.613 \cdot 10^8 \cdot Pa$

The maximum stress in the perforated plate due to bending will be:

$\sigma_{max} := \sigma r_{max} SM_1 SM_2$ $\quad \sigma_{max} = 9.334 \cdot 10^3 \cdot psi$ $\quad \sigma_{max} = 6.436 \cdot 10^7 \cdot Pa$

$\frac{\sigma_{allow}}{\sigma_{max}} = 2.507$ Value should be greater than 1, a margin of 2.607 should be sufficient to cover the additional level A, B and C service limits of ASME

Additionally the stresses will be increased at or near the holes in the perforated plate. The first factor is the same as above for $SM_1 = 4.44$. The second factor is to the stress increase at or near the holes. This can be found from Ref. 3.4 and also Ref. 3.1 in Table 37, Case 6b. The increase in stress at the holes is estimated to be $SM_2 = 2.3$

$SM_2 := 2.3$

The maximum local stress in the perforated plate at the holes will be:

$\sigma_{max} := \sigma r_{max} \cdot SM_1 \cdot SM_2 \quad \sigma_{max} = 1.867 \cdot 10^4 \cdot psi \quad \sigma_{max} = 1.287 \cdot 10^8 \cdot Pa$

The allowable stress is taken from Ref. 3.2 for 316 SS at temperature of 900F. The allowable stress is multiplied by 3 because of the peak stress which is due to local stress near a hole in the plate.

$\sigma_{allow} := 15600 \cdot psi \cdot 3.0 \quad \sigma_{allow} = 4.68 \cdot 10^4 \cdot psi \quad \sigma_{allow} = 3.227 \cdot 10^8 \cdot Pa$

$\frac{\sigma_{allow}}{\sigma_{max}} = 2.507$ Value should be greater than 1, a margin of 2.507 should be sufficient to cover the additional level A, B and C service limits of ASME

**Review the maximum values for deflection, slope, moment, stress and shear**

$y_{max} = -0.051 \cdot in \qquad \theta_{max} = 0.031 \cdot deg$

$Mr_{max} = 1.043 \cdot 10^5 \cdot \frac{lbf \cdot in}{in} \qquad Mt_{max} = 1.043 \cdot 10^5 \cdot \frac{lbf \cdot in}{in}$

$\sigma r_{max} = 1.828 \cdot 10^3 \cdot psi \qquad \sigma t_{max} = 1.828 \cdot 10^3 \cdot psi$

$Q_{max} = -1.744 \cdot 10^3 \cdot \frac{lbf}{in}$

Total deflection of plate (bending induced plus shear induced):

$y_{total} := (y(0\ in) + y_{sro}) \qquad y_{total} = -0.052 \cdot in$

The plate deflection will be increased because of the perforated plate. Ref. 3.4 gives the following changes to the elastic constants for an effective elastic constants. The value of the modulus of elasticity E and Poisson's ratio $\nu$ will change and is a function the ligament efficiency $h/P$. The values for $h/P$ = 50 mm / 222 mm = 0.2252 which were given above.

From Fig. A-8131-1 and the above ligament efficiency of $h/P = 0.2252$

$E_{effective} := E \cdot 0.1609$ $\quad E_{effective} = 3.701 \cdot 10^{6}\ psi$ $\quad E_{effective} = 2.552 \cdot 10^{10}\ Pa$

$\nu_{effective} := 0.4522$

Stiffness of the plate without holes is: $D := \frac{E \cdot t^3}{12\left(1 - \nu^2\right)}$ $\quad D = 1.334 \cdot 10^{10}\ psi \cdot in^3$

Stiffness of the plate with holes is: $D_{effective} := \frac{E_{effective} \cdot t^3}{12\left[1 - \left(\nu_{effective}\right)^2\right]}$

$D_{effective} = 2.456 \cdot 10^{9}\ psi \cdot in^3$

The flexibility increase is: $\frac{D}{D_{effective}} = 5.433$

The perforated plate is 5.434 times more flexible than the solid plate.

Total deflection of the perforated plate (bending induced plus shear induced):

$y_{total} := \left(y(0 \cdot in) + y_{sro}\right) \cdot \frac{D}{D_{effective}}$ $\quad y_{total} = -0.281\ in$

**Large deflection condition check**

Check to verify that the absolute value of the maximum deflection is less than one-half the plate thickness (an assumption stated in the Notation file which must hold true). If $|y_{max}|$ is greater than t/2 (large deflection), the equations in this table used for plates with small deflections are subject to large errors.

$check := if\left(\left|y_{total}\right| > \frac{t}{2}, 0, 1\right)$ $\quad check = 1$

If $|y_{max}|$ is greater than t/2 (i.e., check = 0), only max y and $\sigma$ can be found.

If $|y_{max}|$ is not greater than t/2 (i.e., check = 1), solution okay.

**The remainder of the document displays the general plate functions and constants used in the equations above.**

$$L_{11} \equiv \frac{1}{64} \cdot \left[ \begin{array}{l} 1 + 4 \cdot \left(\frac{r_o}{a}\right)^2 - 5 \cdot \left(\frac{r_o}{a}\right)^4 \ldots \\ + - \left[ 4 \cdot \left(\frac{r_o}{a}\right)^2 \cdot \left[ 2 + \left(\frac{r_o}{a}\right)^2 \right] \cdot \ln\left(\frac{a}{r_o}\right) \right] \end{array} \right]$$

$$L_{17} \equiv \frac{1}{4} \cdot \left[ 1 - \left(\frac{1-\nu}{4}\right) \cdot \left[ 1 - \left(\frac{r_o}{a}\right)^4 \right] - \left(\frac{r_o}{a}\right)^2 \cdot \left[ 1 + (1+\nu) \cdot \ln\left(\frac{a}{r_o}\right) \right] \right]$$

$$G_{11}(r) \equiv \frac{1}{64} \cdot \left[ \begin{array}{l} 1 + 4 \cdot \left(\frac{r_o}{r}\right)^2 - 5 \cdot \left(\frac{r_o}{r}\right)^4 \ldots \\ + - \left[ 4 \cdot \left(\frac{r_o}{r}\right)^2 \cdot \left[ 2 + \left(\frac{r_o}{r}\right)^2 \right] \cdot \ln\left(\frac{r}{r_o}\right) \right] \end{array} \right] \cdot \left(r > r_o\right)$$

$$G_{14}(r) \equiv \frac{1}{16} \cdot \left[ 1 - \left(\frac{r_o}{r}\right)^4 - 4 \cdot \left(\frac{r_o}{r}\right)^2 \cdot \ln\left(\frac{r}{r_o}\right) \right] \cdot \left(r > r_o\right)$$

$$G_{17}(r) \equiv \frac{1}{4} \cdot \left[ 1 - \left(\frac{1-\nu}{4}\right) \cdot \left[ 1 - \left(\frac{r_o}{r}\right)^4 \right] - \left(\frac{r_o}{r}\right)^2 \cdot \left[ 1 + (1+\nu) \cdot \ln\left(\frac{r}{r_o}\right) \right] \right] \cdot \left(r > r_o\right)$$

$$LT_y(r) \equiv \frac{-q \cdot r^4}{D} \cdot G_{11}(r) \qquad LT_M(r) \equiv -q \cdot r^2 \cdot G_{17}(r)$$

$$LT_\theta(r) \equiv \frac{-q \cdot r^3}{D} \cdot G_{14}(r) \qquad LT_Q(r) \equiv \frac{-q}{2 \cdot r} \cdot \left(r^2 - r_o^2\right) \cdot \left(r > r_o\right)$$

# Appendix B – Calculations for Lower End Nozzle Piece

The maximum support weight of the nozzle is based on the heaviest assembly which is the reflector assembly. The weights of the assemblies are given in Appendix A of the report. The total weight for each type of assembly is calculated for the current core design.

$Wt_{max} := 842.8 \cdot kg$ Based on reflector assembly weight

The resulting force on the nozzle would be:

$Force_{max} := Wt_{max} \cdot g$ $Force_{max} = 8.3 \cdot 10^{3} \cdot N$ $Force_{max} = 1.9 \cdot 10^{3} \cdot lbf$

$g = 9.8 \cdot m \cdot s^{-2}$ acceleration of gravity

At the top of the nozzle and using an assumed thickness of 1.0 cm, the cross-sectional area would be:

$Area := \pi \left[ (21.5 \cdot cm)^2 - (19.5 \cdot cm)^2 \right]$ $Area = 0 \cdot m^2$ $Area = 39.9 \cdot in^2$

The bearing stress at the interface of the nozzle and the grid plate would conservatively be:

$\sigma_{bearing} := \frac{Force_{max}}{Area}$ $\sigma_{bearing} = 3.2 \cdot 10^{5} \cdot Pa$ $\sigma_{bearing} = 46.5 \cdot psi$

The resulting stress is very low compared to the ASME allowable stress. The allowable stress is taken from Ref. 3.2 for 316 SS at temperature of 900F. The allowable stress is for primary stress, which is the resulting compressive stress in the upper nozzle section.

$\sigma_{allow} := 15600 \cdot psi$ $\sigma_{allow} = 1.6 \cdot 10^{4} \cdot psi$ $\sigma_{allow} = 1.1 \cdot 10^{8} \cdot Pa$

$\frac{\sigma_{allow}}{\sigma_{bearing}} = 335.2$ Value should be greater than 1, a margin of 335 will be sufficient to cover the additional level A, B and C service limits of ASME

Additionally by engineering judgment the upper nozzle will not experience any buckling issues because the unsupported length is only 12 cm (4.77 in.).

The part of the nozzle which extends through the grid plate is essentially stress free during normal operations. However during assembly and other events the wall thickness was kept the same as the nozzle piece above the grid plate (1.0 cm). The size of the lower nozzle was based on engineering judgment. An additional 1.15 cm is provided around the inner diameter of the upper nozzle piece before it passes through the grid plate. This additional amount of material will provide a proper seat of the nozzle into the grid plate.

$OD_{lower} := 21.5 \cdot cm - 2 (1 \cdot cm + 1.15 \cdot cm)$ $OD_{lower} = 17.2 \cdot cm$ $OD_{lower} = 6.8 \cdot in$

$ID_{lower} := OD_{lower} - 2 (1 \cdot cm)$ $ID_{lower} = 15.2 \cdot cm$ $ID_{lower} = 6 \cdot in$

# Appendix C – Calculations for Fuel Support and Bundle Restraint (Lower/Upper Plates)

The core weight calculations were based on using the average weight density, per component material multiplied by the corresponding volume for each component. This allows for an effective means to determine the static weight which needs to be supported by the fuel support plates.

The component weights and average weight densities are summarized in Section 3.3 of the report. Table 3.2 provides the densities for a regular fuel pin. All of the average densities were adjusted by subtracting the weight density of the SiC – duct material from each average density. This is reduction simply calculated by:

$3.20\ g/cc \times 6.3\% = 0.201\ g/cc = 201.6\ kg/m^3$

The volume for an assembly is calculated from the cross-sectional area times the height of the assembly. The lattice (assembly) pitch distance is used to calculate the cross-sectional area of the hexagonal geometry. The pitch distance is 215 mm (flat-to-flat of the outside duct) plus the inter-assembly gap of 7 mm. The total flat-to-flat distance for the inter-assembly including the gap is 222 mm. The cross-sectional area for a hexagonal area is found in Ref. 3.3 (pg. 1-8) for a six sided polygon:

Area $= 3.464 \times r^2$ , where $r$ = radius of inscribed circle

The values of $r = 111$ mm, which is the assembly pitch of 222 mm / 2 for the current core geometry.

The output from an EXCEL spreadsheet which calculates the weight for each component of the assembly is given below. The total weight of an assembly without the duct is 405 kg.

Assembly Weight Calculations Without SiC Hexcan Duct Weight

| Fuel Assembly | Radius = 111 (mm)<br>Area = 42679.9 ($mm^2$) | | | 0.04268 ($m^2$) | |
|---|---|---|---|---|---|
| Component | Length (m) | Volume ($m^3$) | Wt. Density ($kg/m^3$) | Weight (kg) | |
| Fuel | 1.34 | 0.05719 | 3168.4 | 181.2 | |
| Reflector (lower and upper) | 1 | 0.04268 | 1878.4 | 80.2 | |
| Plenum (lower and upper) | 1 | 0.04268 | 548.4 | 23.4 | |
| Shield (lower) | 0.8 | 0.03414 | 1878.4 | 64.1 | |
| Shield (upper) | 0.7 | 0.02988 | 1878.4 | 56.1 | |
| Total Weight per Assembly | | | | 405.0 | |
| Total Length per Assembly | 4.84 | | | | |

The total weight supported by a fuel support plate is the fuel, reflector, plenum, upper and lower shield plus the fuel support plates and tie rod assembly. The additional weights would be:

| | | |
|---|---|---|
| 1. Tie Rods (6) | | = 11.2 kg |
| 2. Lower Fuel Support plate | = 7.5 kg | |
| 3. Upper Fuel Support plate | = 3.0 kg | |
| 4. Bundle Restraint plates | (2) | = 15.0 kg |
| TOTAL | = 36.7 kg | |

The design of the fuel support plate will conservatively assume all of this additional weight is supported by the plate. The weight of the tie rods is determined from Appendix D. The weights of the fuel support plates are based on an assumed thickness of 2.54 cm (1.0 in.) for the plates with a hexagonal geometry. The density of the bundle restraint plates and the lower plates was 8000 kg/m$^3$ for 316L stainless steel and HT9 steel. The density of upper was 3200 kg/m$^3$ for SiC. The flat-to-flat distance was assumed to be 206 mm for the fuel support plates and bundle restraint plates. Thus for 2.54 cm (1.0in.) plates the volume would be:

$$\text{Volume} = 3.464 \times (103\ \text{mm})^2 \times 25.4\ \text{mm} = 9.334 \times 10^{-4}\ \text{m}^3$$

$$\text{Weight} = 8000 \times \text{Volume} = 7.5\ \text{kg per 316L or HT9 steel plate}$$

$$\text{Weight} = 3200 \times \text{Volume} = 3.0\ \text{kg per SiC plate}$$

The thicknesses of plates were estimated in advance based on engineering judgment and an efficient design. Reference 3.4 on stresses in perforated plate provided the best guidance for the fuel support plates. The outer bundle restraint plates will also have some perforations for cooling requirements. These plates were not designed at this time, but by engineering judgment using the same thickness as the fuel support plates will be adequate.

The following is the design of the lower fuel plate. A conservative support weight is assumed for the loading. The material of the lower fuel support plate was designed to be 316L stainless steel. The resulting maximum stress due to bending and the maximum deflection confirm the fuel support plate thickness of 2.54 cm (1.0 in.) is adequate.

As noted in Figure 3.1 the upper fuel support plate is made of SiC material. ASME does not have stress allowable for this material, however from previous studies the flexural strength at room temperature is 700 MPa (101.5 ksi) and the tensile strength is 100 MPa (14,500 psi). Based on the analysis below for the lower fuel plate with 316L stainless steel, and the reduced load on the upper fuel plate a thickness of 2.54 cm (1.0 in.) is adequate.

Additionally, from Figure 3.1 the bundle restraint plates at the top and bottom of the assembly are constructed from HT9 steel. ASME does not have stress allowable for this material, however other sources have listed the yield stress of around 480 MPa (70,000 psi) at 480 $^0$C (900 $^0$F). The lower bundle restraint plate would be at 480 $^0$C (900 $^0$F) during operation. The upper bundle restraint plate is at 850 $^0$C (1562 $^0$F) during operation but has very small load and does not require much strength to function. The upper bundle restraint plate would require strength during refueling operations, which occur at around 100 $^0$C (212 $^0$F). This was not assessed in the current design, but by engineering judgment the upper and lower bundle restraint plate is adequately designed.

**Table 26 Formulas for maximum deflection and maximum stress in flat plates with straight boundaries and constant thickness**

## Case 19a Regular Polygonal Plate, All Edges Simply Supported; Uniform Load Over Entire Plate

---

**Regular polygonal plate, all edges simply supported**


**Enter dimensions, properties and loading**

Plate dimensions:

length: $a := 4.06 \cdot in$ $a = 10.312 \cdot cm$

thickness: $t := 1 \cdot in$ $t = 2.54 \cdot cm$

Total weight supported by plate $W_{total} := 405 \cdot kg + 36.7 \cdot kg$ $W_{total} = 441.7 \cdot kg$

Compute uniform pressure due to support weight

$$q_{support} := \frac{W_{total} \cdot g}{3.464 \cdot a^2} \quad q_{support} = 17.054 \cdot psi \quad q_{support} = 1.176 \cdot 10^5 \cdot Pa$$

$g = 9.807 \cdot m \cdot sec^{-2}$ acceleration of gravity

Distributed load: $q := 17.1 \cdot psi$ $q = 1.179 \cdot 10^5 \cdot Pa$

Number of sides of the polygon: $n := 6$

Modulus of elasticity: $E \equiv 23.0 \cdot 10^6 \cdot psi$ $E = 1.586 \cdot 10^{11} \cdot Pa$

Poisson's ratio: $\nu \equiv 0.3$

**Calculation procedure**

For a plate material with $\nu$ approximately = 0.3, the stress (s) and deflection (y) are given below:

At center of plate:

$$\sigma := \frac{\beta \cdot q \cdot a^2}{t^2} \qquad \sigma = 297.654 \cdot \frac{lbf}{in^2}$$

$$y_{max} := -\frac{\alpha \cdot q \cdot a^4}{E \cdot t^3} \qquad y_{max} = -1.21 \cdot 10^{-4} \cdot in$$

At the center of the straight edge:

$$Max\_slope := \frac{\xi \cdot q \cdot a^3}{E \cdot t^3} \qquad Max\_slope = 4.732 \cdot 10^{-5}$$

Where a and b and x are interpolated as follows:

$$Table \equiv \begin{bmatrix} 3 & 1.302 & 0.91 & 1.535 \\ 4 & 1.152 & 0.71 & 1.176 \\ 5 & 1.086 & 0.635 & 1.028 \\ 6 & 1.056 & 0.599 & 0.951 \\ 7 & 1.044 & 0.581 & 0.91 \\ 8 & 1.038 & 0.573 & 0.888 \\ 9 & 1.038 & 0.572 & 0.877 \\ 10 & 1.044 & 0.572 & 0.871 \\ 15 & 1.074 & 0.586 & 0.883 \\ 10^{307} & 1.236 & 0.695 & 1.05 \end{bmatrix}$$

$Table^T =$

| | | | | | | | | | |
|---|---|---|---|---|---|---|---|---|---|
| 3 | 4 | 5 | 6 | 7 | 8 | 9 | 10 | 15 | $1 \cdot 10^{307}$ |
| 1.302 | 1.152 | 1.086 | 1.056 | 1.044 | 1.038 | 1.038 | 1.044 | 1.074 | 1.236 |
| 0.91 | 0.71 | 0.635 | 0.599 | 0.581 | 0.573 | 0.572 | 0.572 | 0.586 | 0.695 |
| 1.535 | 1.176 | 1.028 | 0.951 | 0.91 | 0.888 | 0.877 | 0.871 | 0.883 | 1.05 |

$\alpha \equiv \text{linterp}(\text{Table}^{\langle 0 \rangle}, \text{Table}^{\langle 2 \rangle}, n)$ $\alpha = 0.599$

$\beta \equiv \text{linterp}(\text{Table}^{\langle 0 \rangle}, \text{Table}^{\langle 1 \rangle}, n)$ $\beta = 1.056$

$\xi \equiv \text{linterp}(\text{Table}^{\langle 0 \rangle}, \text{Table}^{\langle 3 \rangle}, n)$ $\xi = 0.951$

**Large deflection condition check**

Check to verify that the absolute value of the maximum deflection is less than one-half the plate thickness (an assumption stated in the notation file which must hold true):

$\text{check} := \text{if}\left(\left| y_{max} \right| > \frac{t}{2}, 0, 1\right)$ check = 1

If $|y_{max}|$ is greater than t/2 (i.e., check = 0), a large deflection solution must be used.

If $|y_{max}|$ is not greater than t/2 (i.e., check = 1), solution okay.

---

Maximum stresses will be increased by two factors because of the perforated plate:

First factor is due to the holes in the plate and is calculated from the *P/h* ratio which taken from Ref. 3.4. *P* is the pitch which is the nominal distance between hole center lines. *h* is the nominal width of the ligament at the minimum cross-section. For the fuel support plate *h* = *P* - O.D. of pin hole. The outside diameter of the pin is 9.57 mm so the pin hole will be set to 9 mm. The pitch *P* is the fuel spacing which is 12.6 mm for the current core design

$P := 12.6 \cdot mm$ $h := P - 9 \cdot mm$ $h = 3.6 \cdot mm$

$SM_1 := \frac{P}{h}$ $SM_1 = 3.5$

*Second factor* is the biaxiality ratio, which is taken from Ref. 3.4

Stress Multiplier = 1.15 on bending stress, which is the maximum value for the plate. This is located at the support edge where the biaxiality ratio = 0, thus this is a conservative increase.

$SM_2 := 1.15$

The allowable stress is taken from Ref. 3.2 for 316 SS at temperature of 900F. The allowable stress is multiplied by 1.5 because the stress is due to bending.

$\sigma_{allow} := 15600 \cdot psi \cdot 1.5$ $\sigma_{allow} = 2.34 \cdot 10^4 \cdot psi$ $\sigma_{allow} = 1.613 \cdot 10^8 \cdot Pa$

The maximum stress in the perforated plate due to bending will be:

$\sigma_{max} := \sigma \cdot SM_1 \cdot SM_2$ $\sigma_{max} = 1198.058 \cdot psi$ $\sigma_{max} = 8.26 \cdot 10^6 \cdot Pa$

$\frac{\sigma_{allow}}{\sigma_{max}} = 19.532$ Value should be greater than 1, a margin of 19.5 will be sufficient to cover the additional level A, B and C service limits of ASME

Additionally the stresses will be increased at or near the holes in the perforated plate. The first factor is the same as above for $SM_1 = 4.44$. The second factor is to the stress increase at or near the holes. This can be found from Ref. 3.4 and also Ref. 3.1 in Table 37, Case 6b. The increase in stress at the holes is estimated to be $SM_2 = 2.3$

$SM_2 := 2.3$

The maximum local stress in the perforated plate at the holes will be:

$\sigma_{max} := \sigma \cdot SM_1 \cdot SM_2$ $\sigma_{max} = 2396.117 \cdot psi$ $\sigma_{max} = 1.652 \cdot 10^7 \cdot Pa$

The allowable stress is taken from Ref. 3.2 for 316 SS at temperature of 900F. The allowable stress is multiplied by 3 because of the peak stress which is due to local stress near a hole in the plate.

$\sigma_{allow} := 15600 \cdot psi \cdot 3.0$ $\sigma_{allow} = 4.68 \cdot 10^4 \cdot psi$ $\sigma_{allow} = 3.227 \cdot 10^8 \cdot Pa$

$\frac{\sigma_{allow}}{\sigma_{max}} = 19.532$ Value should be greater than 1, a margin of 19.5 will be sufficient to cover the additional level A, B and C service limits of ASME

**Review the maximum value for deflection**

The plate deflection will be increased because of the perforated plate. Ref. 3.4 gives the following changes to the elastic constants for an effective elastic constants. The value of the modulus of elasticity E and Poisson's ratio $\nu$ will change and is a function the ligament efficiency $h/P$. The values for $h/P$ = 3.6 mm / 12.6 mm = 0.29 which were given above.

From Fig. A-8131-1 and the above ligament efficiency of $h/P = 0.29$

$E_{effective} := E \cdot 0.245$ $\quad E_{effective} = 5.635 \cdot 10^{6}$ psi $\quad E_{effective} = 3.885 \cdot 10^{10}$ Pa

$\nu_{effective} := 0.39$

Stiffness of the plate without holes is: $D := \frac{E \cdot t^3}{12\left(1 - \nu^2\right)}$ $\quad D = 2.106 \cdot 10^{6}$ psi·in$^3$

Stiffness of the plate with holes is: $D_{effective} := \frac{E_{effective} \cdot t^3}{12\left[1 - \left(\nu_{effective}\right)^2\right]}$

$D_{effective} = 5.538 \cdot 10^{5}$ psi·in$^3$

The flexibility increase is: $\frac{D}{D_{effective}} = 3.803$

The perforated plate is 3.8 times more flexible than the solid plate.

Total deflection of the perforated plate :

$y_{max} := -\frac{\alpha \cdot q \cdot a^4}{E \cdot t^3} \frac{D}{D_{effective}}$ $\quad y_{max} = -4.602 \cdot 10^{-4}$ in

**Large deflection condition check**

Check to verify that the absolute value of the maximum deflection is less than one-half the plate thickness (an assumption stated in the notation file which must hold true):

$check := if\left(\left|y_{max}\right| > \frac{t}{2}, 0, 1\right)$ $\quad check = 1$

If $|y_{max}|$ is greater than t/2 (i.e., check = 0), a large deflection solution must be used.

If $|y_{max}|$ is not greater than t/2 (i.e., check = 1), solution okay.

## Appendix D – Calculations for Tie Rods / Wrapper

The tie rods will be 4.84 m in length, which is the span from the lower to upper bundle restraint plates. Six tie rods will be used at each hexagonal corner of the two fuel plates and two bundle restraint plated. The rods will pass through the fuel support plates and be attached to the lower and upper bundle restraint plates.

The design of the tie rods is given below. A cursory check of the hexcan duct (wrapper) is also given for an assessment of the internal pressure loading.

Determine the mass of the 6 tie-rods by assuming a 8 mm OD

$D := 8 \cdot mm$ $L := 4.84 \cdot m$

$Vol_{rod} := \frac{\pi \cdot D^2 \cdot L}{4}$ $Vol_{rod} = 0 \cdot m^3$

$Mass_{rod} := Vol_{rod} \cdot 7760 \cdot \frac{kg}{m^3}$ $Mass_{rod} = 1.888 \cdot kg$

$Mass_{total} := 6 \cdot Mass_{rod}$ $Mass_{total} = 11.327 \cdot kg$

The total mass including the rods and all of the other material is given in Appendix C

$W_{total} := 441.7 \cdot kg$ $W_{total} = 973.782 \cdot lb$

$Force_{total} := W_{total} \cdot g$ $Force_{total} = 4331.597 \cdot N$ $Force_{total} = 973.782 \cdot lbf$

Due to potential dynamic forces from refueling the force will be doubled

$Force_{dynamic} := 2 \cdot Force_{total}$ $Force_{dynamic} = 1947.564 \cdot lbf$

The axial stress in the per rod is:

$Area_{rod} := \frac{\pi \cdot D^2}{4}$ $Area_{rod} = 0 \cdot m^2$

$\sigma_{rod} := \frac{Force_{dynamic}}{6 \cdot Area_{rod}}$

$\sigma_{rod} = 4166.18 \cdot psi$

This stress acts only during refueling operation at 100 $^0$C

The yield stress of HT9 steel at this temperature is:

$\sigma_{yield} := 89800 \cdot psi$ $\sigma_{yield} = 6.191 \cdot 10^8 \cdot Pa$

The equivalent ASME allowable would be 2/3 of yield.

$\sigma_{allowable} := \frac{2}{3} \cdot \sigma_{yield}$ $\sigma_{allowable} = 59866.667 \cdot psi$

$\frac{\sigma_{allowable}}{\sigma_{rod}} = 14.37$ Which is of sufficient margin

A smaller diameter bar of 5 mm diameter is evaluated next

$D := 5 \cdot mm$

The axial stress in the per rod is:

$\sigma_{rod} := \frac{Force_{dynamic}}{6 \cdot Area_{rod}}$ $Area_{rod} := \frac{\pi \cdot D^2}{4}$ $Area_{rod} = 0 \cdot m^2$

$\sigma_{rod} = 10665.42 \cdot psi$

$\frac{\sigma_{allowable}}{\sigma_{rod}} = 5.613$ Which is still a sufficient margin

Thus a 5 mm diameter bar is of adequate design for the tie rods

---

Check Wrapper Design for a internal pressure of 0.5 bar (7.25 psi)

The hexcan duct (wrapper) was designed to be 3.7 mm thick

The stress in the duct wall is (based on a tube geometry which is approximate):

$\sigma_{hoop} := 7.25 \cdot psi \cdot \frac{(215 \cdot mm)}{2 \cdot 3.7 \cdot mm}$ $\sigma_{hoop} = 210.642 \cdot psi$

$\sigma_{yield} := 100 \cdot 10^6 \cdot Pa$ $\sigma_{yield} = 14503.774 \cdot psi$

$\sigma_{allowable} := \frac{2}{3} \cdot \sigma_{yield}$ Based on an ASME equivalent allowable for SiC

$\frac{\sigma_{allowable}}{\sigma_{hoop}} = 45.903$ Which is adequate, but this needs to evaluated for an upper temperature of 850 C to confirm the result


Nuclear Engineering Division
Argonne National Laboratory
9700 South Cass Avenue, Bldg. 208
Argonne, IL 60439-4842

www.anl.gov


A U.S. Department of Energy laboratory
managed by The University of Chicago